공학박사 학위논문

# Synthesis of porous carbon with high electrical conductivity via Carbide-Derived Carbon (CDC) process

탄화물 유도 탄소합성법을 이용한 높은 전기 전도성을 갖는 다공성 탄소 합성

2017 년 08 월

서울대학교 대학원

재료공학부

한 지 선

Imagination is more important than knowledge

Albert Einstein

Dedicated to Aurora

# Abstract

Porous carbon materials have attracted great attention in academic and industrial areas, such as gas sorption, electrode materials, and catalyst materials because it has high specific surface area, porosity, and high electrical conductivity. Carbide derived carbons (CDCs), which are synthesized by selectively removing metal phase in carbides using chlorine gas, is characterized by micropore (i.e. pores less than 2 nm), and interestingly its pore size is finely tuned within sub-angstrom range by changing the carbide precursor or synthesis temperature. The tunable porosity in sub-angstrom range have made extensive interests in various application and will bring advantages in especially electrode materials. Among the porous carbons synthesized by various methods, mesoporous CDCs have been intensively researched in electrode materials because it has micropore originated from chlorination of carbide and mesopore resulted from the porosity in the carbides, and this hierarchic porous structure could result in excellent adsorption properties and enhanced kinetic in adsorption processes. However, the current methods accompanied the multiple synthesis process including templating and severe washing to produce micro/mesoporous CDCs and are limited to silicon carbide systems due to facile adhesion of polycarbosilane on mesopore $SiO_2$. Main part in the dissertation is focused on the simple and effective ways to synthesize hierarchic CDC with mesopore from the titanium carbonitride and porous titanium carbide. Through the chlorination of titanium carbonitride, we found a new experimental result that the graphite layer is nucleated at a low temperature of 300 degrees at the step edge and grows along the particle's ledge surface. Lastly, the novel method based on KOH activation is introduced to develop two dimensional graphene from graphite layers grown on the surface of the carbon synthesized by chlorination of titanium carbonitride, and thus leads to

hybrid graphene/porous carbon material.

First, titanium carbonitride, $Ti(C_xN_{1-x})$ are obtained by carbothermal reduction of $TiO_2$ with graphite under $N_2$ atmosphere. The composition of nitrogen in $Ti(C_xN_{1-x})$ can be tuned by molar ratio of $TiO_2$ and graphite, and synthesis temperature and nitrogen pressure. Through the chlorination, the porosity can be changed depending on the composition of C and N in $Ti(C_xN_{1-x})$ and chlorination temperature. Since chlorine react with $Ti(C_xN_{1-x})$ layer by layer, as formed $TiCl_4$ is vaporized carbon remained as the forms of C-C and C-N bonds. However, because C-N bonds are unstable at high temperature, decomposition occurs as a form of $CN_x$ and $N_2$, which resulted in additional pore generation from meso- to macropore depending on the nitrogen contents in $Ti(C_xN_{1-x})$. As nitrogen content increases remaining carbon is gasified with increasing temperature due to severe decomposition of C-N bonds which results in collapse of microporous structure, and hence meso- and macropore were developed without micropore. Therefore, in this dissertation, $Ti(C_{0.7}N_{0.3})$ was chosen for synthesizing the porous carbon with uniform pore structure. Chlorination at 700℃ (denoted as CN700) leads to porous carbon with micropore of 0.7 nm and mesopore in the range of 1~3 nm. With increasing chlorination temperature, pores are broaden into the large mesopores. Interestingly, by decomposition of $CN_x$, active nitrogen, such as pyrrolic and pyridonic-N, were doped uniformly into carbon lattice. This materials was applied to adsorbent for arsenic removal in water. The detailed mechanism of arsenic adsorption is discussed.

Second, mesoporous titanium carbide are synthesized by carbothermal reduction of $ZnTiO_3$ with graphite under argon atmosphere. Since Zn-based bonds are firstly broken by carbon and gradually reduced into Zn, Ti component is readily reduced and transformed to titanium

carbide. The reason why $ZnTiO_3$ was chosen is because Zn reacts with carbon and does not form carbide but is easily reduced at 907 ° C to be vaporized and removed, so that porous carbide can be formed. This process can result in mesoporous titanium carbide, because metallic Zn is vaporized with a fast rate at high temperature making the holes of 2~80 nm in the TiC particles. Chlorination of porous titanium carbide with mesopores induces porous carbon with a hierarchical pore structure because the holes are connected to micropores to serve as pore channels. Since this method can be applied to various porous carbides (TiC, MoC, ZrC, SiC, etc.), it has an advantage of not only controlling the pore size of micropores but also having a hierarchical pore structure. This hierarchic CDC was applied to the capacitive deionization and showed high speed characteristics.

Lastly, Novel method to develop graphene from graphite layers is introduced. The graphite layers were grown on the carbon surface synthesized by chlorination of $Ti(C_{0.7}N_{0.3})$. The graphite layer can be intercalated by metal potassium (K) to form graphite-intercalation compounds and can be peeled off into several layers by mechanical stimulation. The metal K formed by KOH activation is intercalated into the graphite layers of CN700, and the disordered carbon inside is activated through the oxidation reaction to activate the pore structure. In addition, this peeled graphite layers were developed into a two-dimensional graphene composed of one to three layers through simultaneous activation reaction with a molten salt (KCl). Due to the activation process and development into two-dimensional graphene, the hybrid graphene/porous carbon material has a very high electrical conductivity of 2200 S/m, high specific surface area of 3779 $m^2/g$, and high pore volume of 2.70 $cm^3/g$. Synthesis mechanism and its characteristics are explained in detail. Its material was applied to capacitive deionization and showed good sorption amounts and rates.

**Keywords: Porous carbon, Carbide-derived carbon, Micropore, Pore size distribution, Hierarchical pore structure, Nitrogen doping, Porous carbide, graphene, electrical conductivity, Arsenic removal, Capacitive deionization, Chemical activation.**

**Student number: 2011-20676**

# Contents

# List of Figures

# List of Tables

# 1. Introduction

## 1.1. General introduction

Most of the material that makes up man is carbon. Carbon is not only an indispensable being of living nature, but also an important element in inorganic chemistry and materials science. Surprisingly, carbon has various properties depending on the type of arrangement. In diamond crystals, carbon is the hardest material on earth, graphite is one of the best conductive materials, and carbon dioxide is part of the carbon cycle and affects the climate. Fullerene and graphene, one of the materials of greatest interest recently, are now one of the most attractive materials in science.

Porous carbon materials, which can be classified into three types according to the International Union of Pure and Applied Chemistry (IUPAC) classification[1]; Micropores < 2 nm, 2 nm < mesopores < 50 nm, and macropores > 50 nm, have received a lot of attention because of their high specific surface area, well-developed pore structure, and moderate electric conductivity [2,3]. Along with these properties, it has been applied to gas storage [4], water purification [5], catalyst supports [6], and electrodes for supercapacitor [7] and battery [8]. Even though a variety of ways to produce the porous carbon materials are reported, synthesis methods that uniformly control the micropores of subatomic size are challenging [9]. Among them, zeolite-templated carbon (ZTC) [10] and carbide-derived carbon (CDC) [11] can only uniformly control the pore size on an atomic scale.

This thesis focuses on the chlorination method of synthesizing CDC. The micropore, a feature and a great advantage of CDC [11], plays an important role in the sorption properties of the gas and the supercapacitor's electrolyte. Narrowly tunable pore size in micropore helps separate the gases with different sizes and increase the gas sorption amounts. In the case of physical sorption, since the gas is adsorbed by carbon walls of the CDC, as the pore size is small the interaction between carbon and gas increases [12]. Therefore, through the optimizing the pore size it is capable of adsorbing a large amount of gas with higher adsorption energy than the other carbon materials. In addition, it was reported that CDC supercapacitor showed anomalous increase in capacitance when pores fits well the size of ions of organic electrolytes [7]. This result is different from traditional view that, as pore size decrease to less than twice the solvated ion size, normalized capacitance decreased because compact ion layers from adjacent pore walls impinged and the surface area usable for double-layer formation was reduced. This traditional trend is reversed when pore size decreases to less than the solvated ion size. As a result, the control of pore size and its application to various electrochemical adsorption will not only provide new directional studies but also bring more enhanced properties than existing ones.

Despite the good property of micropore, there is a need for additional mesopore in the CDC that can facilitate adsorption capacity as well as the kinetic of the adsorption process. Up to now, there has been an attempt to produce hierarchic CDC with mesopore by synthesizing the porous SiC using polymer [13, 14] and template methods [15]. In particular, the porous SiC-derived carbon synthesized by the template method maintains high capacitance at high current density in Li-S battery [16] and supercapacitor [17] through a hierarchical pore structure having mesopore and micropore at the same time. However, these methods are

complicated due to the use of templates, and they are costly. Furthermore, since they are limited to SiC synthesis, a new and easy method for synthesizing various porous carbides is required.

Electrical conductivity of carbon and also CDC depends normally on the crystallinity of carbon layer, which is influenced by the synthesis temperature. However increasing the synthesis temperature increases the electrical conductivity, but it accompany the decrease in the surface area of carbon. So, the methods to design the carbon materials that increase the electrical conductivity with increasing surface area are quite important when they are apply to electrochemical application.

Overall, specific surface area, hierarchical pore structure, and conductivity are the most important factors in carbon materials [18]. If we can develop a hierarchic CDC that can control the size of micropore while enhancing the electrical conductivity, potential applications will be realized in the electrochemistry.

## 1.2. Carbide-Derived Carbon (CDC)

In 1918, the production of silicon chloride by reaction of chlorine gas with silicon carbide, according to equation 1, was patented by Otis Hutchins [19].

$$SiC\ (s) + 2Cl_2\ (g) \rightarrow SiCl_4\ (g) + C\ (s) \quad - \quad \text{eq.1}$$

The solid carbon, initially known as waste byproduct, has been spotlighted in 1959 by Walter Mohun since its characterization and its potential application. Since then, the synthesis

method and properties of CDC (Carbide derived carbon) have been optimized by Gogotsi [20] and the application of CDC has shown remarkable potential. Recently, CDC materials are synthesized from a wide range of binary and ternary carbides, such as TiC, VC, WC, SiC, ZrC, $Ti_3SiC_2$, $Ti_3AlC_2$, etc. [21-27].

CDC is porous carbon materials synthesized by selective removal of metal or metalloid atoms, using hot chlorine gas, from a crystalline metal carbide precursor. It is characteristic for CDC process that, as chlorine react with metal, the carbon layer is formed by inward growth and typically retains the original shape and volume of the precursor [28]. Because of this conformal reaction, CDCs is characterized by micropores (i.e. pores less than 2 nm), and interestingly its pore size is finely tuned within sub-angstrom range depending on the types of carbide precursor or the synthesis temperature. According to figure 1 [29], at low synthesis temperature, the carbon layer exists as amorphous structure, with making narrow pores less than 2 nm. As the synthesis temperature increases, the carbon layer is well organized with the graphite structure and has a broader pore size distribution with a sacrifice of micropore. In addition to synthesis temperature, the structure of CDCs varies from amorphous to highly ordered graphitic nature depending on the stoichiometry and the crystal structure of carbide, which also effect pore size distribution as shown in figure 2 [30]. For example, TiC- and SiC-derived carbon retain relatively amorphous structure at moderate chlorination temperature, however, the carbon layers derived from $Cr_2C_3$, $Al_3C_4$, and $Fe_3C$ are highly organized into graphite structure at relatively low temperature [31-33]. In case of $Fe_3C$-derived carbon [33] crystallinity of graphite is more enhanced by the aid of catalytic effect of iron. In order for the crystalline graphite to be grown, graphene should be nucleated. After etching of metal phase nucleation for graphene can be made by stepped edges with many broken bonds. This

principle apply to graphene/SiC film studies [34-36]. The graphene is grown by applying a step edge to the (0001) SiC film by various methods. However, because this step edge promotes nucleation, too many step edges will grow the multi-layer graphene. In order to grow a few-layered graphene laterally for wafer scale, one should decrease the step density and increase the terrace surface. Therefore, the step edges in the TiC and SiC powders will nucleate the graphene after chlorination. Through this process, graphene/porous carbon hybrid can be synthesized because graphene growth is terminated at the defects such as grain boundary, and beneath the graphene, amorphous carbon are grown inward the carbide.

Microporous CDC can be promising materials for electrochemical applications, such as electrode materials for supercapacitor and battery if hierarchical mesopore are incorporated. For this reason, among the various porous carbon materials, hierarchic CDCs with mesopore have been intensively researched in electrode materials because it has micropores originated from chlorination of carbides and mesopores resulted from the porosity in the carbides, which could result in excellent adsorption properties and enhanced kinetic in adsorption processes [37-39]. However, the current methods accompanied the multiple synthesis process including templates to produce micro/mesoporous CDCs and are limited to silicon carbide systems due to facile adhesion of polycarbosilane on mesopore $SiO_2$

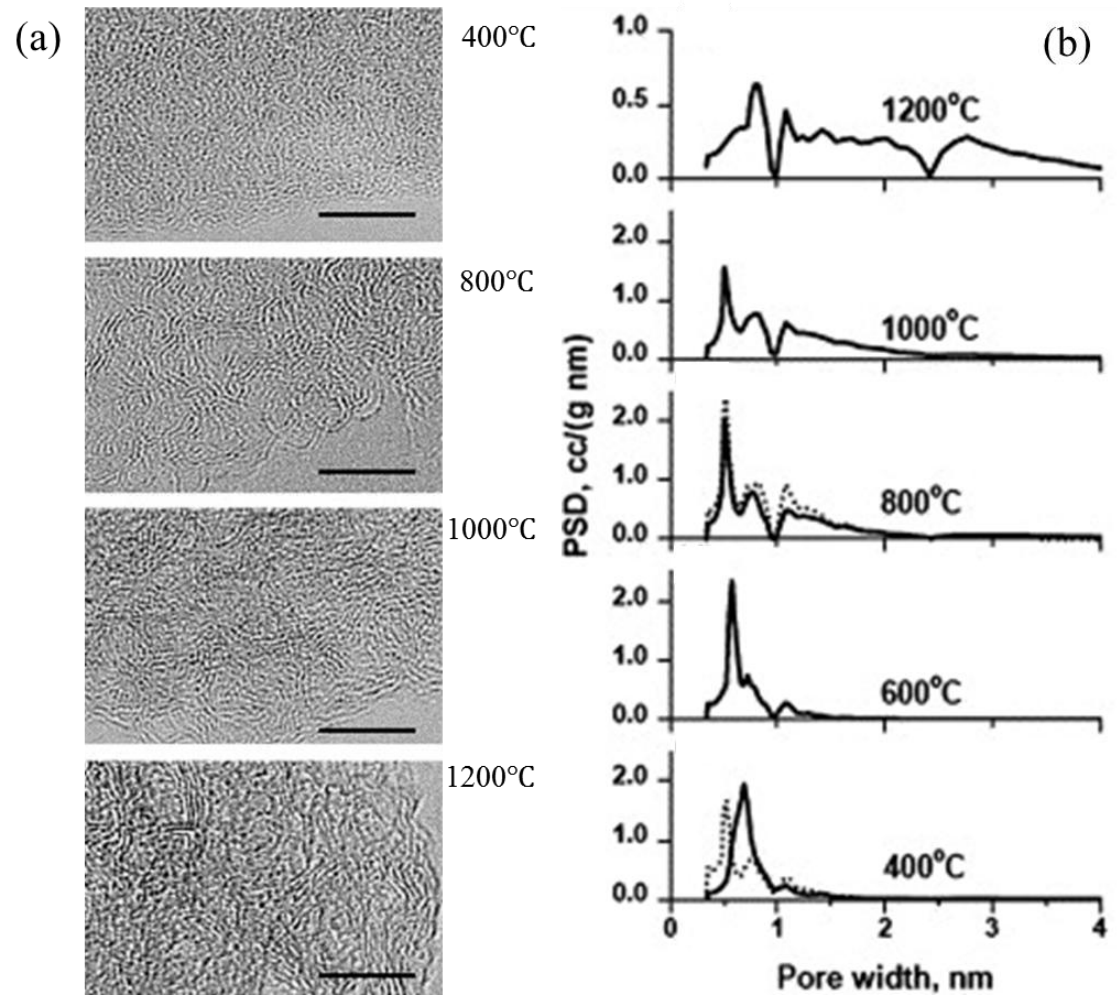


Figure 1. TEM images (a) of TiC–CDC synthesized at 400 ℃, 800 ℃, 1000 ℃, and 1200 ℃; scale bar 5 nm. The carbon produced at 400 ℃ is mostly amorphous. Thin non-planar graphitic fringes are seen from the sample at 800 ℃ and above. PSDs (b) of TiC–CDC synthesized at 400 ℃, 600 ℃, 800 ℃, 1000 ℃, and 1200 ℃. As synthesis temperature increases, the PSDs become broad with a sacrifice of micropore. (Data from reference [29])

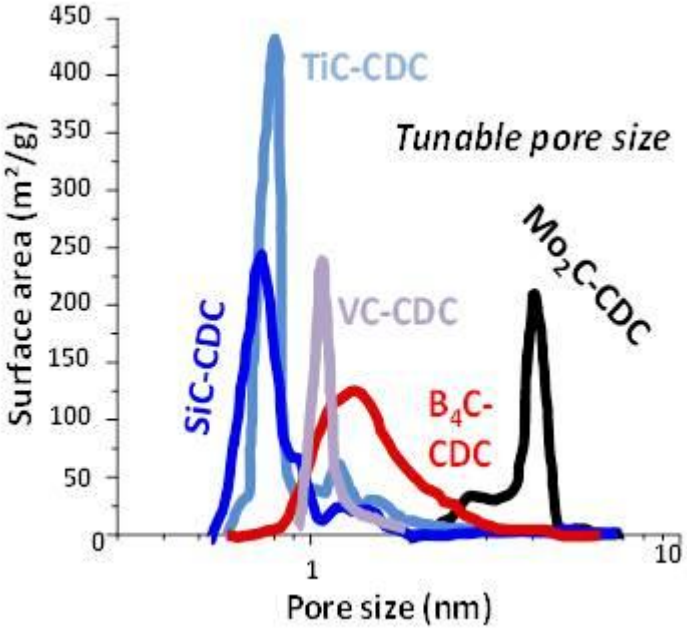


Figure 2. Pore size distributions for different carbide precursors. (Data from reference [30])

## 1.3. Arsenic removal

On account of the high concentration of arsenic in groundwater and its carcinogenic health effects, a global concern for arsenic has emerged and is growing [40]. The National Academy of Science (NAS) and the National Research Council (NRC) have reported that even a concentration of 3 μg/L of arsenic can cause the risk of bladder and lung cancer, leading to between 4 and 7 deaths per 10,000 people, and by the extended long-term exposure of 10 μg/L arsenic, this risk can increase up to 23 deaths per 10,000 people [41]. In most countries, the maximum contaminant level (MCL) in drinking water has been set to 50 μg/L [42]; however, the MCL has been enforced to a lower value, as the World Health Organization (WHO) had recommended an MCL of 10 μg/L in 1993 [43]. Furthermore, the US Environmental Protection Agency (EPA) has recommended a lower standard of 5 μg/L, which has been currently adopted by the Department of Environmental Protection of New Jersey, USA.

On the other hand, among the sorption materials for arsenic, iron oxides or hydroxides have demonstrated excellent sorption characteristics and have been applied to various carbon nanomaterials [44,45]. Typically, improvement in the adsorption capacities of adsorbents has been performed by either decreasing the particle sizes of iron oxides or hydroxides or changing supporting agents such as carbon-based materials [46], As these modification procedures can be easily optimized, intensive efforts have been focused on the development of eco-friendly iron-based materials for the removal of arsenic; meanwhile, the progress of chemically and thermally stable carbon for the adsorption of arsenic is insignificant as compared to its broad and successful utilization as sorbents and energy-related materials

[47,48]. Furthermore, as the removal of arsenic is conducted in water, adsorbents should not contain impurities, which can contaminate the water; in addition, they should exhibit chemical stability during the removal of arsenic so as not to react with arsenic and form byproducts [49]. Hence, changing the intrinsic properties of carbon, such as by the modification of the pore structure and doping by heteroatoms, such as N, S, and B, is highly desired.

Carbide-derived carbon (CDC), prepared by the selective removal of metal from carbide, exhibits narrow pore size distributions with a high specific surface area, typically originating from the micro-pore region [50]. These characteristics of CDC facilitate its use as gas adsorbents and electrode materials for supercapacitors. Recently, modified CDC, having dual micro- and meso-porous regions, has been synthesized by the template method followed by chlorination [51]. On account of its well-developed micro-pores, which exhibit strong interaction between the adsorbent and adsorbate, and uniform meso-pores, which facilitate the diffusion of electrolytes, it demonstrates high performance for use in lithium sulfur batteries [51].

On the other hand, as doping pure carbon with nitrogen makes it highly reactive, nitrogen-doped carbon can be applied for $CO_2$ capture and electrocatalytic activity [52,53]. In fact, nitrogen-doped carbon has been applied as an adsorbent for arsenic [54,55]. However, because of insufficient sorption properties, the role of nitrogen has not been investigated well in the field of arsenic capture.

In this study, we synthesized nitrogen-doped carbon by the chlorination of titanium carbonitride, $Ti(C_xN_{1-x})$, which exhibits well developed micro- and small meso-pores with uniform pore structures. Furthermore, the adsorption capacities for arsenic were extensively investigated. We found that these nitrogen-doped CDC with unique CDC-like porosities can

be promising method new for arsenic adsorption, even comparable to metal oxide-carbon hybrid reported previously.

## 1.4. Capacitive deionization

The supply of clean water at a reasonable price is one of the core technology, social and economic challenges of the 21st century. Clean water, which should of course be provided to mankind, is still not available to one in seven people in the world. The more serious the problem is that as we increase the groundwater extraction around the world, the more progressive saline infiltration occurs in the wells and aquifers. As a result, much attention has been focused on developing economically attractive desalination technologies. Over the years, several of the most popular technologies, such as distillation, reverse osmosis, and electrodialysis, have been developed [56]. The pursuit of current research is to increase energy efficient and cost efficiency for desalination. With the energy-efficient technology, brackish water, which is large enough on the planet, will be used adequately for human consumption, agriculture and industry.

Capacitive deionization (CDI) is an emerging technology for desalination of water with a low or moderate salt content [57]. Due to its robust, energy efficient, and cost effectiveness, CDI have been attracted great attentions over the existing technologies, and as it can be conducted at ambient conditions and low voltages (< 2V) it is eco-friendly technology without secondary waste and does not require high-pressure pumps, distillations columns, or thermal heaters. Practical application is expected with development of flow-electrode CDI

[58]. As shown of scheme of CDI in figure 3 [59], it works by using a pair of oppositely arranged porous carbon electrodes that store ions when applying an electrical voltage difference. These electrodes can be assembled into a stack of multiple pairs. In the brackish water flowing through the "spacer channel" between the two electrodes, $Na^+$ of the cation and $Cl^-$ of the anion are fixed while forming an electric double layer in the pores inside the carbon material. In order to regenerate the carbon electrode, when all accessible pore volumes are saturated with electro-adsorbed ions, the cell voltage is reduced or reversed. In this way, the electrodes again regain their initial ionic absorption capacity. Ideally, there is no chemical reaction, the lifetime of the CDI device is long and easy to maintain.

Since CDI is based on electrosorption of ions with interfacial process, high surface area carbon electrodes should be used in order to have the maximum contact area between electrode and water [60]. For optimization of electrosorption amounts and sorption rates, physical properties of porous carbon such as porosity and electrical conductivity are considered for the important factors. Various carbon materials have been studied for desalination by CDI, with the development of novel carbon materials such as carbide derived carbon (CDC) [61], ordered carbon [62], carbon nanotube and graphene [63]. Microporous carbons (< 2 nm) such as activated carbon and CDC have shown good electrosorption amounts superior to mesoporous carbon, similar phenomenon to capacitance of electric-double layer capacitor electrodes [64]. However, the micropores themselves have serious limitations on ion transport in CDI flow cells. For facile ion transport inside of carbon electrodes, hierarchical mesopore are needed. Recently, using templated CDC [60], which consist of a large micropore volume with hierarchical mesopores (2~50 nm), the CDI performances in terms of electrosorption amounts and sorption rates, have been significantly

improved. Meanwhile, electrical conductivity is also important parameter to have optimum performance of CDI. A combination of conductive carbon, such as graphene and carbon nanotube (CNT), and porous carbon with high surface area have been realized by many researchers [65,66], in order to have high ion sorption amount and rate with low voltage ( about 1.2 V). However, because poor connectivity of these material, caused by experimental limitation, and trade-off between electrical conductivity and specific surface area, most CDI performance of hybrid materials did not outperform the commercial AC-MSP20 that showed 14.3 mg/g sorption amount at a cell voltage of 1.2 V. Therefore, careful design of these material should be conducted to have one structure for synergistic effect which comes from the high surface area and good electrical conductivity.

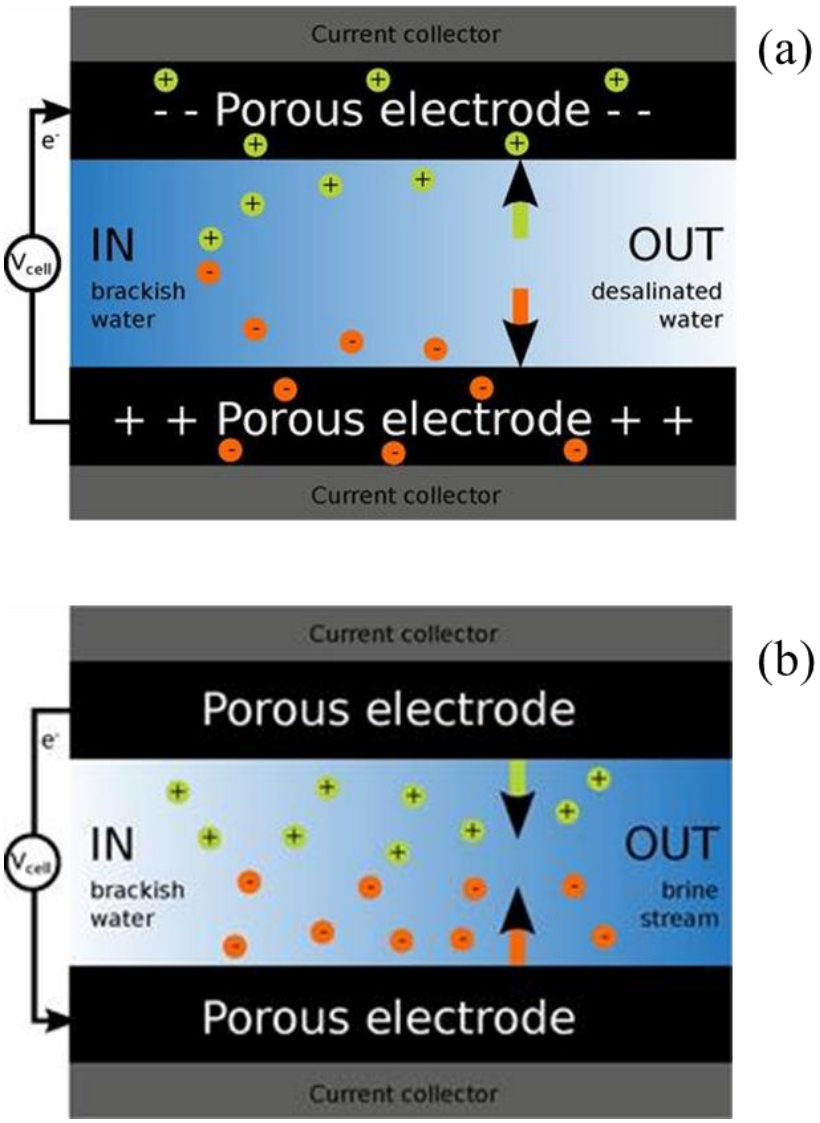


Figure 3. Schematic design of a cell for Capacitive Deionization (CDI). When a voltage difference is applied between two porous carbon electrodes, ions are attracted to the electrode, positive ions to the negative electrode (cathode, top) and negative ions to the positive electrode (anode, bottom). As a result,

desalinated water is produced (a). In order to regenerate the electrodes, desorption of ions from electrode should occur by reducing or reversing the cell voltage (b). (Data from reference [59])

## 1.5. Hybrid graphene/porous carbon

Hybrid carbon materials, a combination of two complementary materials, have attracted great attention, because it could give synergistic effects in various applications [67-69]. For example, hybrid carbon in which fullerenes are covalently attached to the single-walled carbon nanotubes (SWNTs) is formed on the iron-catalyst particles during CO disproportionation [70]. Because the fullerene is combined to the surface of a conductive SWNT in one structure, a number of highly curved fullerene surfaces serving as emission sites have improved properties in cold electron field emission. Recently, a hybrid material in which graphene is connected to a porous carbon is attracting attention in the field of electrochemistry due to its high conductivity and high specific surface area [67-69]. Well-developed pore-structured carbon and conductive crystalline graphene enable easy transport of electrolytes, ions and electrons. Therefore, the synergistic effect can be obtained if two substances are connected by one structure.

With high theoretical surface area, good mechanical flexibility, excellent electrical and thermal conductivity, graphene, an atomic thick two dimensional layer of carbon, has been

extensively applied to various fields, especially electrochemical application [71-73]. However, graphene, despite having theoretical high BET SSA, has suffered from the limited specific surface area available due to Van der Waals forces and π–π stacking [74]. In order to solve this problem, various effective methods of making porous graphene have been intensively reported [71-74]. However, graphene having two dimensional structure and high BET SSA (i.e. more than 2000 $m^2/g$) is still limited. To endow graphene high surface area (i.e. more than 2000 $m^2/g$) there have been intensive researches, such as activation of graphene itself [75] and hybridization of graphene with porous carbon [76]. Activation of graphene increased the surface area to over 3000 $m^2/g$ due to the severe etching of in-plane carbon, but the electrical conductivity was limited to 500 S/m. The hybrid synthesis methods for producing graphene/porous carbon are divided into two main methods. The first method is made by the hydrothermal method of graphene oxide and amorphous carbon, and the second one by chemical vapor deposition (CVD) method. These two methods ultimately involve KOH activation. In the former case [77], both the graphene oxide and the amorphous carbon are activated and the BET SSA is well developed (3523 $m^2/g$), but the conductivity is limited (303 S/m). In the latter method [69], the graphene developed by the CVD is well-crystallized, so that the amorphous carbon developed by CVD is dominantly activated resulting in high electrical conductivity (5460 S/m), but there is a limit to the BET SSA (513 $m^2/g$). As a result, both methods show tradeoffs that the electrical conductivity increases as the BET SSA decreases, and vice versa (figure 4). A new strategy is needed to create a hybrid material in which crystalline graphene and porous carbon are combined into one structure, thus possessing high electrical conductivity and BET SSA.

Herein, we design the simple and effective route to synthesis of hybrid material of nano-

architectured graphene/porous carbon as shown in figure 5. This hybrid carbon showed a well-developed pore structure with a very high electrical conductivity of 22,000 S/m, a high BET SSA of 3779 $m^2$/g and a pore volume of 2.70 $cm^3$/g. The key to hybrid carbon synthesis is the use of KOH and KCl to activate the carbon in which the irregular carbon inside of particle and the graphite layers on the particle surface have a single structure. Since graphite is layered structure it can be intercalated by alkali metals. Beguin et al. [78] suggested through the XRD results of the intercalation compound phase that the metal K produced during KOH activation could be inserted into regular ordered graphite layers but not into disordered graphite layers. According to Kaner's study (figure 6 [79]), graphite intercalated compound could be readily exfoliated by reacting it with aqueous solutions and reconstructed by mechanical stimulation. In this study, we found that during the KOH activation of carbon, the graphite layer was intercalated by metallic K and reconstituted by the washing step into few layers of graphite while the disordered carbon was predominantly activated. Surprisingly, by activating CN with KOH and KCl, a few layers of graphite developed into two-dimensional (2D) graphene, where KCl acts as a template for lateral growth. As a result, the developed graphene has a structure that is gently connected to porous carbon. The mechanism of development of 2D graphene is discussed in detail in this work. This promising hybrid material was used as electrode materials for capacitive deionization (CDI) which is attracting great attention as a novel desalination technology. Due to well-developed pore structure and conductive graphene interface, high Na+ and Cl- ions sorption rate and capacity were achieved.

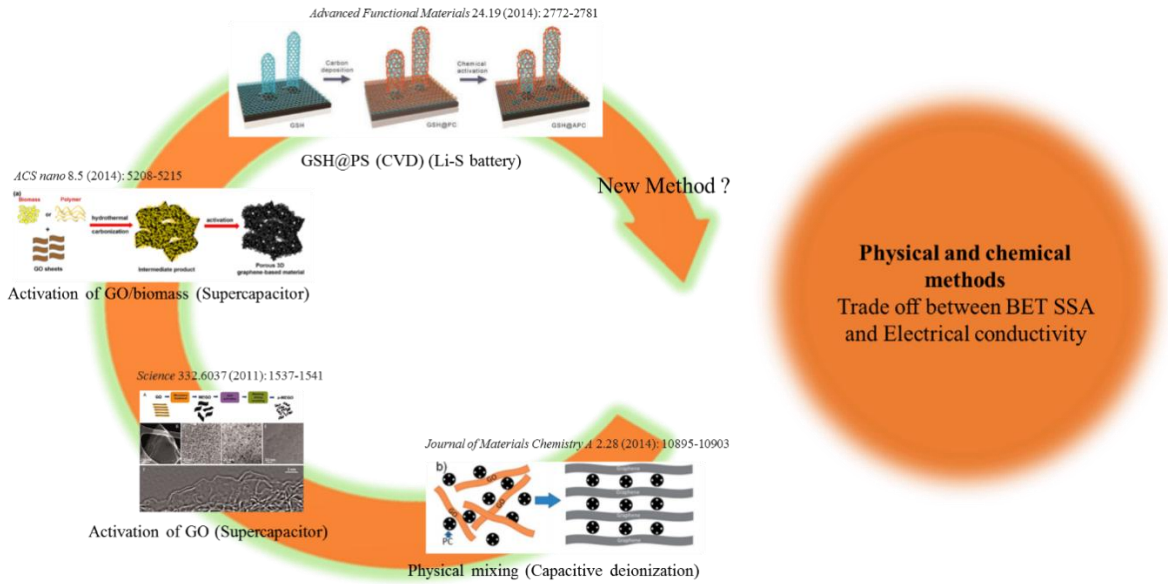


Figure 4. The methods to make hybrid carbon materials are demonstrated. But, new method is needed in order to have hybrid material that have high BET SSA and electrical conductivity.

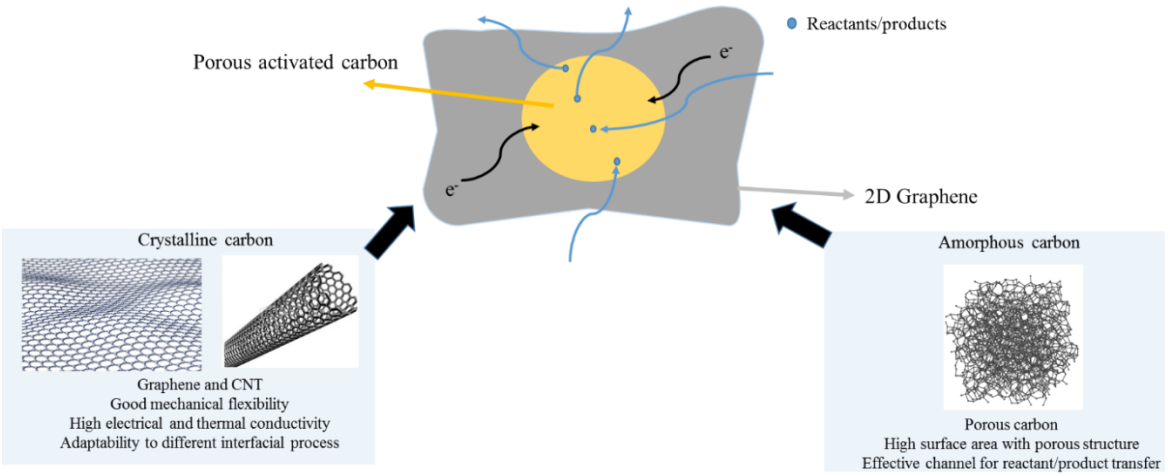


Figure 5. Scheme of hybrid graphene/porous carbon. Seamlessly connected structure enable facile transfer of reactants/products and electrons (SSA↑ and conductivity↑).

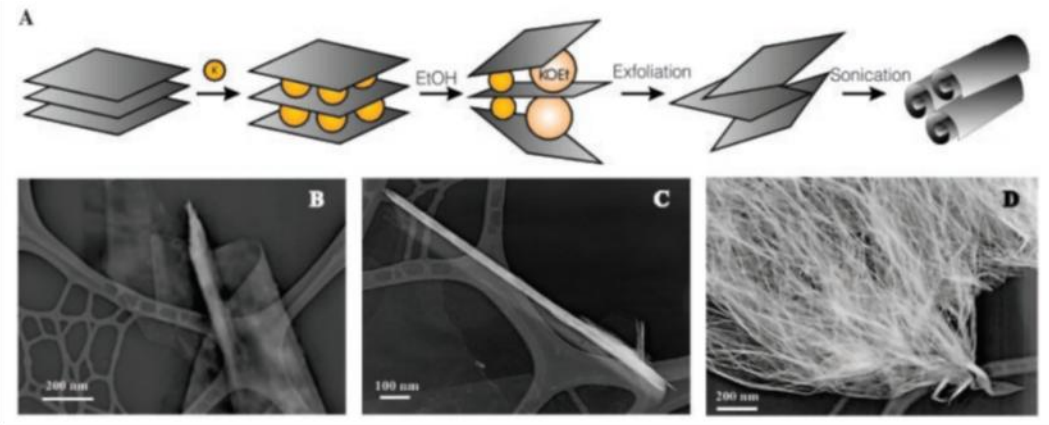


$KC_8 + CH_3CH_2OH \rightarrow 8C + KOCH_2CH_3 + ½\ H_2$, Exothermic reaction

Figure 6. Synthesis of carbon nanoscroll by exfoliating the graphite intercalation compounds. [Data from reference [79])

# 2. Experimental Procedures

## 2.1. Synthesis methods

### 2.1.1. Synthesis of porous titanium carbide (TiC)

Porous titanium carbide (TiC) was prepared by carbothermal reduction of zinc titanate ($ZnTiO_3$) using graphite. $ZnTiO_3$ was first prepared by the specific mixture of $TiO_2$ (99%, Aldrich) and ZnO (99%, Aldrich) followed by a thermal treatment at 800 ℃ for 24 hour in air [99]. Using high energy ball milling with a condition of 250 rpm for 5 hour, $ZnTiO_3$ and graphite were mixed with the ratio as the equation below.

$$ZnTiO_3\ (s) + 4C\ (s) \rightarrow Zn\ (v)\ \uparrow\ + TiC\ (s) + 3CO\ (g)\ \uparrow$$

In order to analyze the porosity and structure of the carbide with the heat treatment time, the above mixture was heat treated at 1250 ° C for 3 h, 6 h, 12 h and 24 h in argon atmosphere. The by-product produced in the outer part of the heat treatment zone was analyzed as Zn and ZnO through XRD. As a comparison, crystalline TiC was prepared by carbothermal reduction of $TiO_2$ (99%, Aldrich) using graphite. The mixture obtained under the same milling conditions as above was subjected to heat treatment for 1 hour at 1600 ° C under vacuum ($10^{-3}$ torr). XRD, $N_2$ sorption analysis, FESEM, and TEM were used to analyze the pore structure and microstructure of porous TiC and crystalline TiC. The porous TiC derived from $ZnTiO_3$ is

denoted by Zn-TiC-Xh, where X is heat treatment time and the crystalline TiC derived from $TiO_2$ is denoted by TiC.

### 2.1.2. Synthesis of porous titanium carbide-derived carbon with hierarchical pore structure

Porous TiC-derived carbon was prepared by normal chlorination experiment [9]. The starting powder (1 g) was placed in the graphite boat and injected into the quartz tube of the furnace. The furnace was heated to 800 ℃ with at a rate of 10 ℃/m under argon atmosphere. Next, at 800 ℃, $Cl_2$ gas was passed through the quartz tube for 1 h. Then, after chlorination, the samples were subjected to heat-treatment under $H_2$ gas at 600 ℃ for 2 h for removing residual $Cl_2$ gas and trapped chlorides. Finally, the samples were subjected to Ar, when increased or decreased in temperature. As a comparison, crystalline TiC-derived carbon was prepared by same way with the method to produce the porous TiC-derived carbon. The porous TiC-derived carbon is denoted by Zn-TiC-Xh-CDC, where X is heat treatment time for carbide synthesis and the crystalline TiC-derived carbon is denoted by TiC-CDC.

### 2.1.3. Synthesis of micro- and mesoporous N-doped carbon (CN) derived from titanium carbonitride

Titanium carbonitride, $Ti(C_{0.7}N_{0.3})$, was purchased from Treibacher Industry AG. First, 3g of $Ti(C_{0.7}N_{0.3})$ was placed in a quartz tube furnace and heated to different temperatures (700–1000 ℃) under Ar atmosphere. Next, at the desired temperature, $Cl_2$ gas was passed through the quartz tube for 3 h. Then, after chlorination, the samples were subjected to heat-treatment under $H_2$ gas at 600 ℃ for 2 h for removing residual $Cl_2$ gas and trapped chlorides. Finally, the samples were subjected to Ar, when increased or decreased in temperature. The powders, formed by the chlorination of $Ti(C_{0.7}N_{0.3})$, showed hierarchical pore structure with micro- and mesopore. Micropore, developed as $TiCl_4$ gas was selectively desorbed, are hierarchically interconnected to the mesopore, which was developed by desorption of thermally unstable $CN_x$ and $N_2$ gases. CNX are denoted on the basis of doped nitrogen on carbon which is determined by balancing between retaining and reconstructing the bonds after Ti is etched out as a form of $TiCl_4$, and X means different heating temperature; for example, CN700, CN800, CN900, and CN1000. For comparison, TiC—CDC was synthesized via same chlorination process at 800 ℃.

## 2.1.4. Synthesis of graphene/porous carbon hybrids

CNs, which was presented in 2.1.2., is used for synthesizing the graphene/pours carbon hybrid. Since chlorination is conformal reaction, its morphology and size in particles are not changed. Particles of $Ti(C_{0.7}N_{0.3})$ was characterized by flat and step edge surface. After

chlorination, particles of CN was also characterized by flat and step edge surface. Close observation of CN surfaces by TEM shows crystalline graphitic layers. aCN-KOH was synthesized by KOH activation of CN in a 1:4 mass ratio at 800 °C for 1 h under $N_2$ flow with a heating rate of 3 °C $min^{-1}$. aCN-KOH/KCl was synthesized by KOH and KCl in situ activation of CN at 800 °C for 1 h under $N_2$ flow with a heating rate of 3 °C $min^{-1}$ with a 1:4:12 mass ratio. For control experiment, CN-KCl was synthesized by KCl activation of CN with 1:12 mass ratio and aCN-KOH-KCl was obtained by KCl activation of aCN-KOH with 1:3 mass ratio at 800 °C for 1 h under $N_2$ flow with a heating rate of 3 °C $min^{-1}$. Commercial AC, amorphous carbon, was activated by same method above and was denoted by aAC-KOH in case of KOH activation of AC in a 1:4 mass ratio and aAC-KOH/KCl in case of KOH and KCl in situ activation of AC in a 1:4:12 mass ratio. all conduced at 800 ℃ for 1 h under $N_2$ flow with a heating rate of 3 ℃ $min^{-1}$.

## 2.2. Experiment methods

### 2.2.1. Arsenic removal experiments

Arsenic-contaminated water using various CNs was subjected to equilibrium batch tests. Arsenic adsorption tests were conducted in 50 mL conical tubes under batch conditions at ambient temperature. First, 50 mL of an arsenic solution (pH 4.02–5.30) with initial concentrations of 5, 10, 25, 50, and 100 mg/L was added into 50 mL conical tubes each containing 0.006 g of CNs. The equilibrium adsorption test was also performed using TiC-CDC for comparing the adsorption of arsenic using CNs with that using typical CDC. Second, samples were mixed using a rotary shaker at 100 rpm. Next, after the reaction was completed, the liquid phase was separated from the solution using a 0.45 μm PTFE syringe filter (Millipore). Finally, the arsenic concentration was measured by inductively coupled plasma optical emission spectroscopy (ICP-OES) on a Perkin-Elmer (Optima 2000 DV) spectrometer at a pump rate of 1.5 mL/min.

For quantifying the adsorption property of the CNs, the equilibrium adsorption of arsenic was analyzed by the Freundlich and Langmuir adsorption isotherm models, which are shown in Eqs. (1) and (2), respectively:

$$q = KC^{\frac{1}{n}}$$ equation (1)

here, $q$ is the adsorbed concentration (mg/g), $C$ is the equilibrium aqueous concentration (mg/L), and $K$ and $n$ are empirical constants.

$$q = \frac{q_m K_a C}{1 + K_a C} \qquad \text{equation (2)}$$

here, $q_m$ is the maximum mass adsorbed under saturation conditions per mass unit of adsorbent (mg/g). $K_a$ is the empirical constant with units of inverse of concentration $C$ (1/mg).

### 2.2.1.1. Zeta potential measurements

Zeta potentials of CNs and TiC-CDC were measured using a zeta potential analyzer (Zetasizer nano ZS, Malvern Instruments Ltd., UK). Aqueous suspensions of CNs and TiC-CDC were prepared in glass vial. The pH values of the suspensions were adjusted to 2–12 using dilute HCl or NaOH. The vials were shaken at 20 rpm for 4 h prior to zeta potential analysis, and the equilibrium pH was also measured.

### 2.2.1.2. Simulation details

First-principles calculations were calculated on the basis of density functional theory (DFT) using Vienna Ab initio Simulation Package for structure optimization. The general gradient

approximation (GGA) method was adapted to describe exchange correlation functional, and the pseudopotential was parameterized under the projector augmented wave (PAW) method by Perdew–Burke–Ernzerhof (PBE). The van der Waals interaction was included with the vdw-DF2 method for describing ionic bonding character. The energy cut-off for the plane wave basis set was 400 eV, and the optimization tolerance was 0.01 eV/Å. The unit-cell size was set to $25 \times 25 \times 15$ Å$^3$ for avoiding inter-cell interactions. The free energies for the optimized structure were also calculated for including the contributions from entropy and zero-point energy. The GAUSSIAN09 program was used for calculating free energy by adopting the 6-31 g (d,p) basis set and the M06-2X exchange correlation functional. The adsorbent was based on circumcoronene (CC), which is composed of 54C and 18H atoms. All configurations in the figures were drawn using VESTA.

## 2.2.2. Capacitive deionization experiments

### 2.2.2.1. Electrode fabrication

CN, aCN-KOH, and aCN-KOH/KCl electrodes were prepared by a slurry mixture of each powder (80 wt%), carbon black (Super P, Timkan graphite and carbon 10 wt%) and polytetrafluoroethylene (PTFE, Sigma-Aldrich, 10 wt%) with a mortar and pestle. The mixtures were handled by a roll press machine to fabricate the sheet-type electrodes, then the electrodes were dried in vacuum oven at 60 ℃ for 12 h. The thickness of the electrodes was approximately 300 μm.

### 2.2.2.2. Electrochemical characterization

Galvanostatic charge/discharge was carried out with two electrodes system in which the fabricated electrodes were employed as a working and counter electrode using a battery cycler (WBCS3000, WonA Tech Co) in 1M of NaCl aqueous solution. Cyclic voltammetry (CV) and Electrochemical Impedance Spectroscopy (EIS) were conducted with a potentiostat (PARSTAT 2273, Princeton Applied Research) using a three electrode system that consisted of the fabricated electrodes (CN, aCN-KOH, and aCN-KOH/KCl electrodes) as not only a working electrode but counter electrode, and Ag/AgCl KCl saturated electrode as a reference electrode.

### 2.2.2.3. Deionization test

The deionization performance, following the procedure of the previous studies, was carried out in a continuous flow system (one pass experiment). A pair of electrodes was employed with the contact area of 3 $cm^2$, and the nylon separator with a thickness of 200 μm offered the flow stream between two electrodes. 1.2 V and 0 V were applied to the cell for 10 min in charging step and discharging step, respectively. The rate of flow stream was approximately 2 mL/min, and the concentration of influent was 10 mM of NaCl aqueous solution. The conductivity of effluent was monitored by a conductivity meter (3573-10C, HORIBA, Ltd)

and the measured conductivity was converted to the concentration of NaCl. In this study, the deionization performance was expressed by the salt adsorption capacity (SAC) which indicates how much ions were deionized by the mass of employed electrodes.

# 3. Results and discussion

## 3.1. Porous Titanium carbide-derived carbon with hierarchical pore structure

### 3.1.1. Motivation

It is characteristic for CDC process that, as chlorine react with metal, the carbon layer is formed by inward growth and typically retains the original shape and volume of the precursor [28]. Because of this conformal reaction, CDCs is characterized by micropores (i.e. pores less than 2 nm), and interestingly its pore size is finely tuned within sub-angstrom range depending on the types of carbide precursor or the synthesis temperature [80]. However, in the conventional technology, the synthesis method of obtaining a hierarchical pore by simultaneously developing micropore and mesopore in carbide-derived carbon is challenging. Up to now, there has been an attempt to produce hierarchic CDC with mesopore by synthesizing the porous SiC using polymer and template methods. In particular, the porous SiC-derived carbon synthesized by the template method maintains high capacitance at high current density in Li-S battery [16] and supercapacitor [17] through a hierarchical pore structure having mesopore and micropore at the same time. However, these methods are complicated due to the use of templates, and they are costly. Furthermore, since they are limited to SiC synthesis, a new and easy method for synthesizing various porous carbides is required.

### 3.1.2. Results of porous Titanium carbide-CDC with hierarchical pore structure

In the conformal transformation of the chlorine reaction, the pore structure of the carbide can be connected to the micropore after the chlorination reaction to provide a hierarchical pore. Therefore, we have developed an easy and cost effective method to develop porosity in various carbides. $ZnTiO_3$ was selected for the synthesis of porous TiC because it is possible to carbonize $ZnTiO_3$ at thermodynamically lower temperatures of 1142 ℃ than to reduce $TiO_2$, as shown in the figure 7. For synthesis of $ZnTiO_3$, carbon ratio was calculated and added so that 1 mole of TiC and Zn were produced. The powder produced in the outer part of the heating zone was identified as Zn and ZnO through XRD in the figure 7. It is believed that ZnO is formed as Zn is oxidized. The reason for this is that if the ZnO is formed, the ZnO phase should be present together with the TiC formed in the heating zone since the melting temperature is as high as 1975 ℃ and vaporization is hardly occurred at the heat treatment temperature of 1250 ℃. However, since ZnO was not detected with the TiC phase, it is presumed that Zn was oxidized by $CO/CO_2$ gas produced during carbothermal reduction.

The scheme (figure 8) shows that porous TiC is synthesized via $ZnTiO_3$ and produces a hierarchical porous carbon through chlorination. When $ZnTiO_3$ is transformed into TiC, the released Zn and $CO/CO_2$ gases create holes of various sizes in TiC to produce meso/macro pores. The conformal transformation of chlorination links the pores of the carbide with the micropore in a hierarchical manner.

As shown in figure 9, XRD was analyzed to confirm the phase and structure of TiC obtained in the heating zone. In the case of the powder heat treated at 1250 ℃ for 3 hours, a large

amount of $Ti_3O_5$ and $Ti_2O_3$ as intermediate phases of reduction were detected along with cubic $Ti(C_xO_y)$ phase. As intermediate phases during the reduction of $TiO_2$, Kwon et al. [81] showed the sequence of the reduction of $TiO_2$ as follows: $TiO_2 \rightarrow Ti_nO_{2n-1}$ ($n > 10$) $\rightarrow Ti_nO_{2n-1}$ ($4 < n < 10$) $\rightarrow Ti_3O_5 \rightarrow Ti_2O_3 \rightarrow Ti(C_xO_Y)$. The solid solution of $Ti(C_xO_Y)$ phase is further reduced and transformed to TiC phase. It became evident that 3 hours is not enough to transform all the oxides to carbide. Most of the oxides were transformed to cubic TiC phase after heat treatment for 6 hours, but $TiO_2$ phase was detected. Since $Ti_2O_3$ and $Ti_3O_5$ are covered with carbon, additional oxidation of these materials is not likely to occur during the heat treatment. It is considered that $TiO_2$ is formed in defects such as dislocation, grain boundary, and surface edge of TiC with large surface area. Zn-TiC-24h heat-treated for 24 h had little $TiO_2$ phase because defects is significantly reduced as heat treatment time increases. The WC phase present in the XRD is due to contamination of WC balls through milling. The XRD patterns of the TiC (111) plane of each Zn-TiC-X were presented in the figure 10, where X indicates 3h, 6h, 12h, and 24h. The peak of the (111) plane of Zn-TiC-3h was broad and shifted to higher angle of two theta. This means that it has nano-sized $Ti(C_xO_y)$ phase. On the other hand, the samples annealed for more than 6 hours correspond to the reference TiC peak, which means that the TiC phase is successfully synthesized.

The microstructure and porosity of the synthesized Zn-TiC-X was analyzed by TEM and presented in the figure 11-14. As shown in the arrows in Figure 11a, the particles has holes regardless of particle size. Particles are sized ranging from 20 to 200 nm. Particles of $ZnTiO_3$ with an average size of 300 nm are first cracked due to the release of the reduced Zn, and the particles are pulverized to a size of 20 to 100 nm. The nanoparticles were bound together because they are unstable during the heat treatment. The circles in figure 11a and 11b show

the intermediate step of the merging of several particles into one particle. In figure 11c, the red arrow shows particles with little holes, and the black arrows show that there is one large hole in a 200 nm large particle. Overall, nano-sized Ti($C_xO_y$) and oxides were surrounded by carbon fringes, which are identified in figure 11d. As the annealing time increases, the carbon fringe gradually decreased, and the average particles progressively grew to about 200 nm, which had a large hole in the center. In the case of Zn-TiC-12h, large and small particles coexist, and large pores are clearly identified in large particles (figure 13). For the sample heat treated for 24 hours, uniform particles of 200 nm are observed throughout the particle, flat holes are seen in the particles and slightly truncated holes are also observed. In addition, there is a large amount of ledge surface inside the particle. The stable plane of cubic TiC is a (100) plane, so flat ledges grow inside the particles as steps (figure 14).

Zn-TiC-12h was chlorinated at 800 ℃ for 1 hour, and named Zn-TiC-12h-CDC. The TEM micrographs of the obtained CDC powder is shown in the figure 15. Through conformational transformation, the morphology of the carbides remained on the carbon obtained. As shown in the TEM (figure 15), the holes of the carbide remain after the carbon is formed. However, the (100) plane which was flat in the carbide becomes slightly rough after carbon formation, which is attributed to the amorphous characteristic of carbon after the chlorination. The EDS of TEM (figure 16) was analyzed to determine the atomic proportions of carbon, nitrogen, and oxygen in the synthesized Zn-TiC-12h-CDC. As a result carbon was analyzed as 96.4%, oxygen as 3.6%, and nitrogen as 0%.

XRD and Raman spectra were measured to analyze the structure and the defect of the sample made through the chlorination reaction of Zn-TiC-X (figure 17). TiC-CDC was also measured for comparison. In the XRD, TiC-CDC, which is characterized by micropore,

showed high intensity at low angle of two theta. This was evident in the carbon obtained after the chlorination reaction of the sample heat treated for 12 h and 24 h. However, in the case of carbon obtained after chlorination of Zn-TiC-3h with Ti($C_xO_y$) phase, the intensity of the low angle decreases and the (002) and (10) peaks developed, indicating the turbostratic structure. After Ti is removed in the form of $TiCl_4$, the carbon that retained the micropore reacts with the surrounding oxygen and is etched in the form of $CO/CO_2$, so that the carbon is reconstructed and the degree of crystalline develops. The WC produced by milling remained after the chlorination reaction, but the oxide was mostly removed after the chlorination reaction. In Raman spectra (figure 18), all the samples showed broad D band, which was ranged from 1332 to 1341 $cm^{-1}$, and G band, which was ranged from 1587 to 1596 $cm^{-1}$, indicating the carbon obtained by chlorination showed disordered carbon. For disordered porous carbon, the D and G band widths are commonly used as a measure of disorder in the carbon-carbon bonding network. Compared to TiC-CDC, Zn-TiC-X-CDC showed much-decreased D band full-width at half-maximum intensity (FWHM), indicating that the carbon-carbon bonding becomes more uniform and less defective. A decrease in D band is much pronounced in Zn-TiC-3h-CDC, because of reconstruction of carbon-carbon bonding network. This result is in good agreement of XRD (figure 17).

The $N_2$ sorption isotherms (figure 19) were conducted to analyze the pore characteristics of the carbides and their CDCs. In the case of carbide (shown in the figure 19a), TiC has almost no pore structure, whereas Zn-TiC-X have micro-, meso-, and macropore. Especially, Zn-TiC-3h among the Zn-TiC-Xs has well-developed pore structure. The pore structure of the carbon obtained after the chlorination reaction is shown in figure 19b. TiC-CDC is characterized by well-developed micropore. On the other hand, Zn-TiC-X-CDC has not only

micropore but also mesopore and macropore. This is similar to the characteristics of meso- and macropore of the existing carbide. This verified that the pore structure of the carbide was hierarchically linked to the micropore of the carbon synthesized after the chlorination reaction. The pore characteristics of all the samples were summarized in table 1. Zn-TiC-3h has BET specific surface area (SSA) of 464 $m^2/g$ and as annealing time increased BET surface area is decreased. The high BET surface areas obtained from Zn-TiC-Xs are due to the holes produced in the carbide particles compared to the low BET surface area values of 2 and 3 $m^2/g$ of TiC and $ZnTiO_3$, respectively. The TiC-CDC has a BET SSA of 1439 $m^2/g$ and micropore volume of 0.58 $cm^3/g$ with almost no mesopore. Zn-TiC-3h-CDC showed decreased BET SSA of 1402 $cm^3/g$ because of reconstruction of carbon-carbon bonding, but had high mesopore volumes of 1.66 $m^3/g$. In case of Zn-TiC-24h-CDC had high BET SSA of 2025 $m^2/g$ with high micro- and mesopore volumes of 0.76 $cm^3/m$ and 1.01 $cm^3/g$, respectively.

### 3.1.3. Conclusions

Mesoporous titanium carbide were successfully synthesized by carbothermal reduction of $ZnTiO_3$ with graphite under argon atmosphere. Since Zn-based bonds were firstly broken by carbon and gradually reduced into Zn, Ti component was readily reduced and transformed to titanium carbide. This process resulted in mesoporous titanium carbide, because metallic Zn was vaporized with a fast rate at high temperature making the holes of 2~80 nm in the TiC particles. Chlorination of porous titanium carbide with mesopores produced porous carbon with a hierarchical pore structure because the holes are connected to micropores to serve as pore channels, which was evidenced by TEM analysis. Since this method could be applied to various porous carbides (TiC, MoC, ZrC, SiC, etc.), it had an advantage of not only controlling the pore size of micropores but also having a hierarchical pore structure. This hierarchic CDC was applied to the capacitive deionization and showed higher speed characteristics compared to commercial titanium carbide-derived carbon.

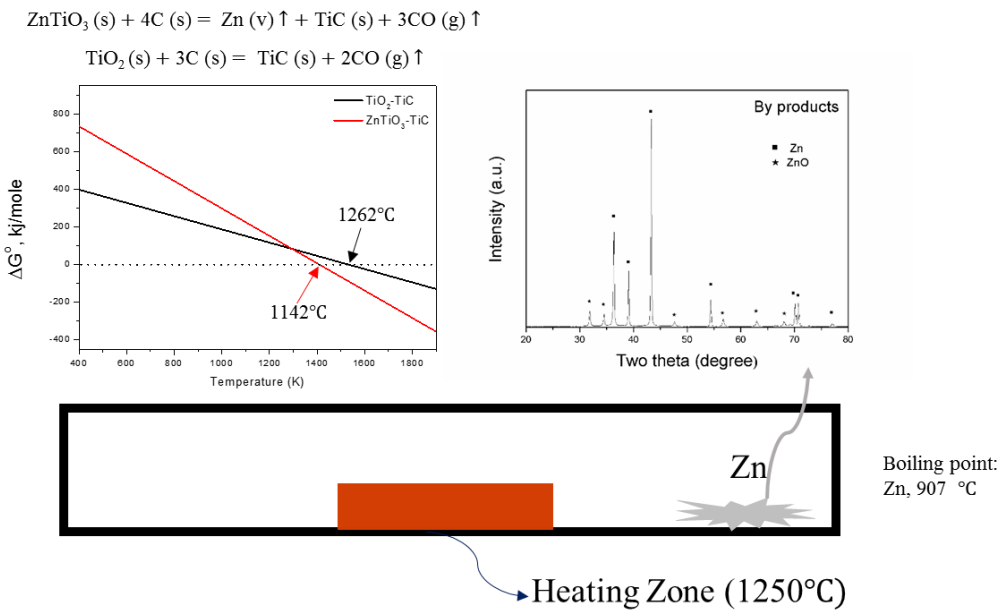


Figure 7. Thermodynamic calculation for carbothermal reduction of oxides. The XRD result of Zn/ZnO as a by-product.

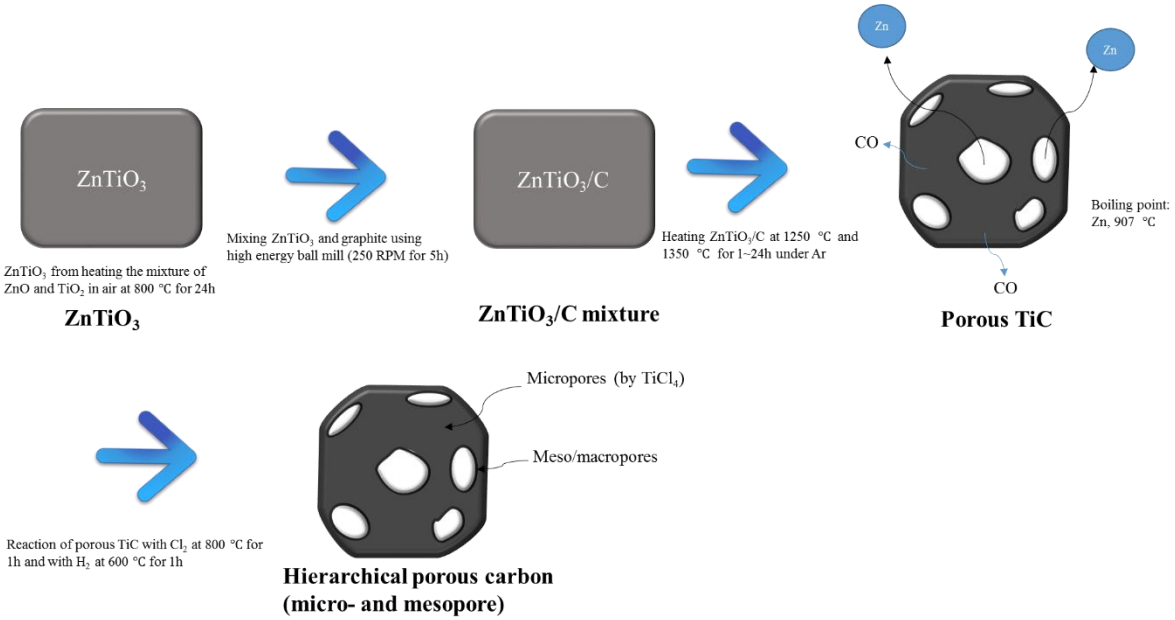


Figure 8. Scheme of synthesizing the hierarchical porous carbon (Zn-TiC-X-CDC).

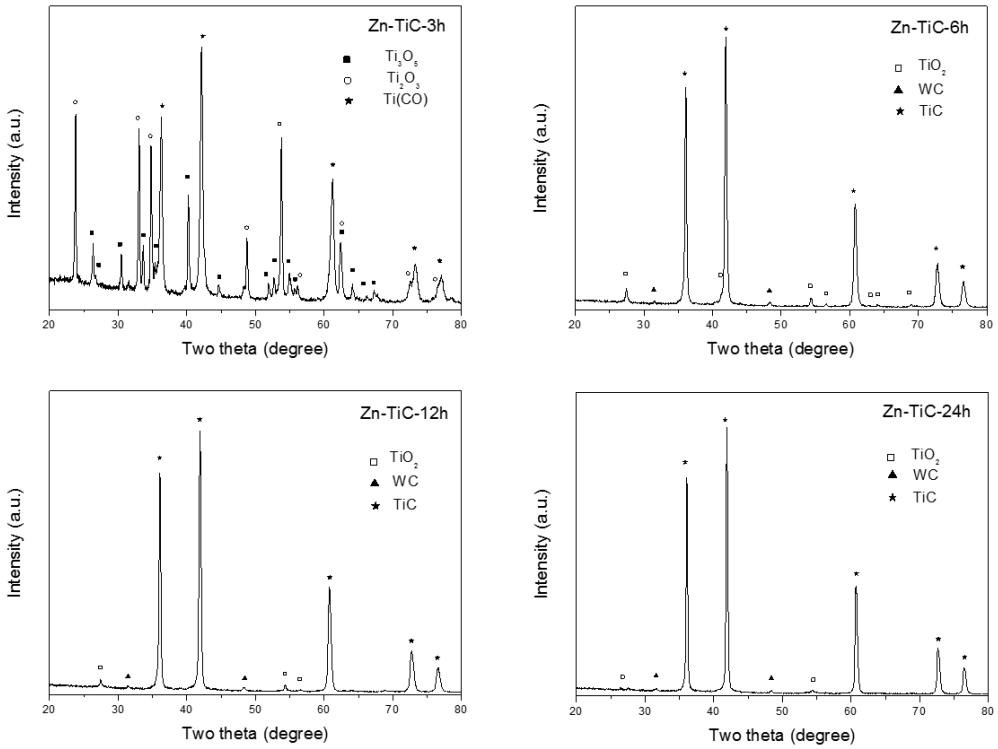


Figure 9. XRD results of Zn-TiC-X (X: 3h, 6h, 12h, and 24h).

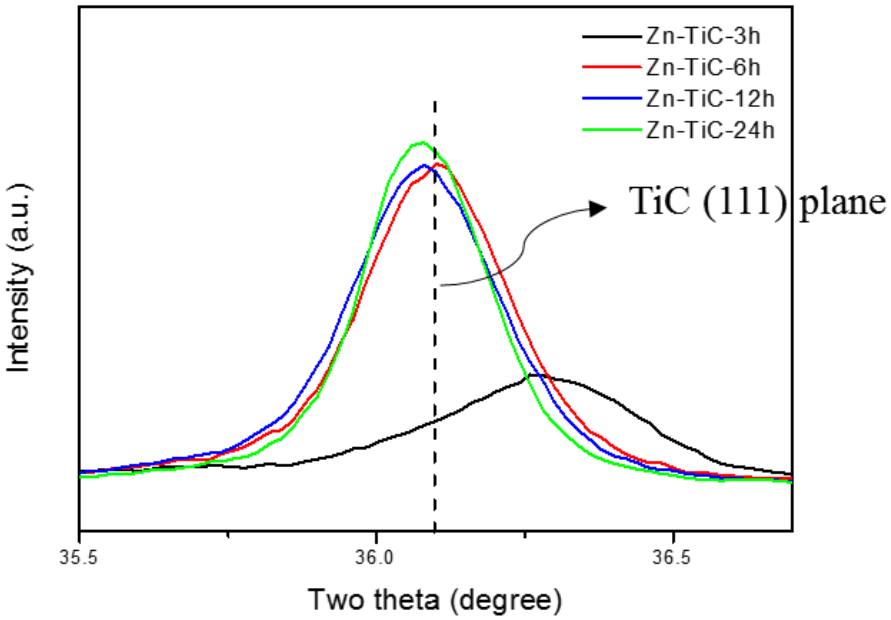


Figure 10. XRD results of Zn-TiC-X (X: 3h, 6h, 12h, 24h at 1250℃) showing peak shifts of (111) plane.

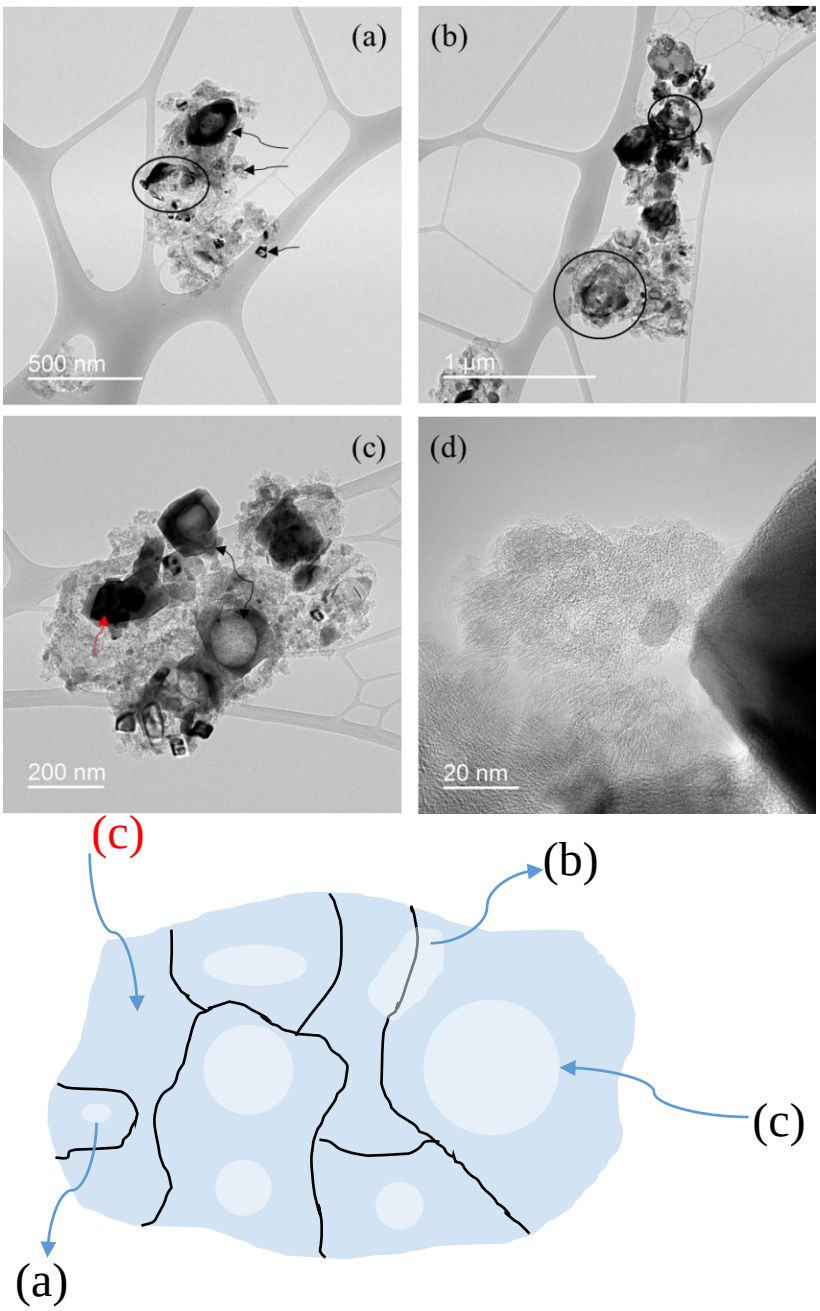


Figure 11. TEM micrographs and scheme of Zn-TiC-3h.

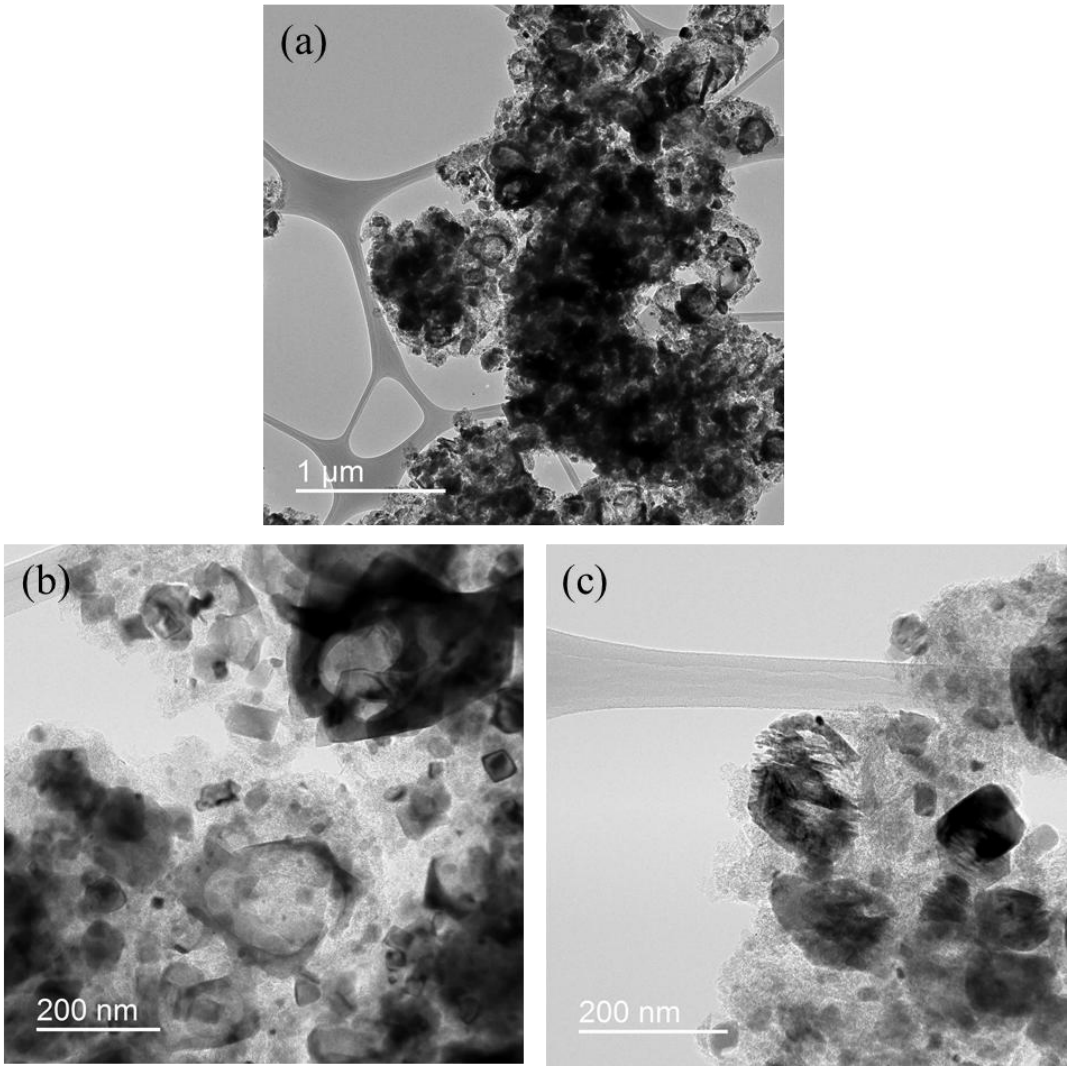


Figure 12. TEM micrographs of Zn-TiC-6h.

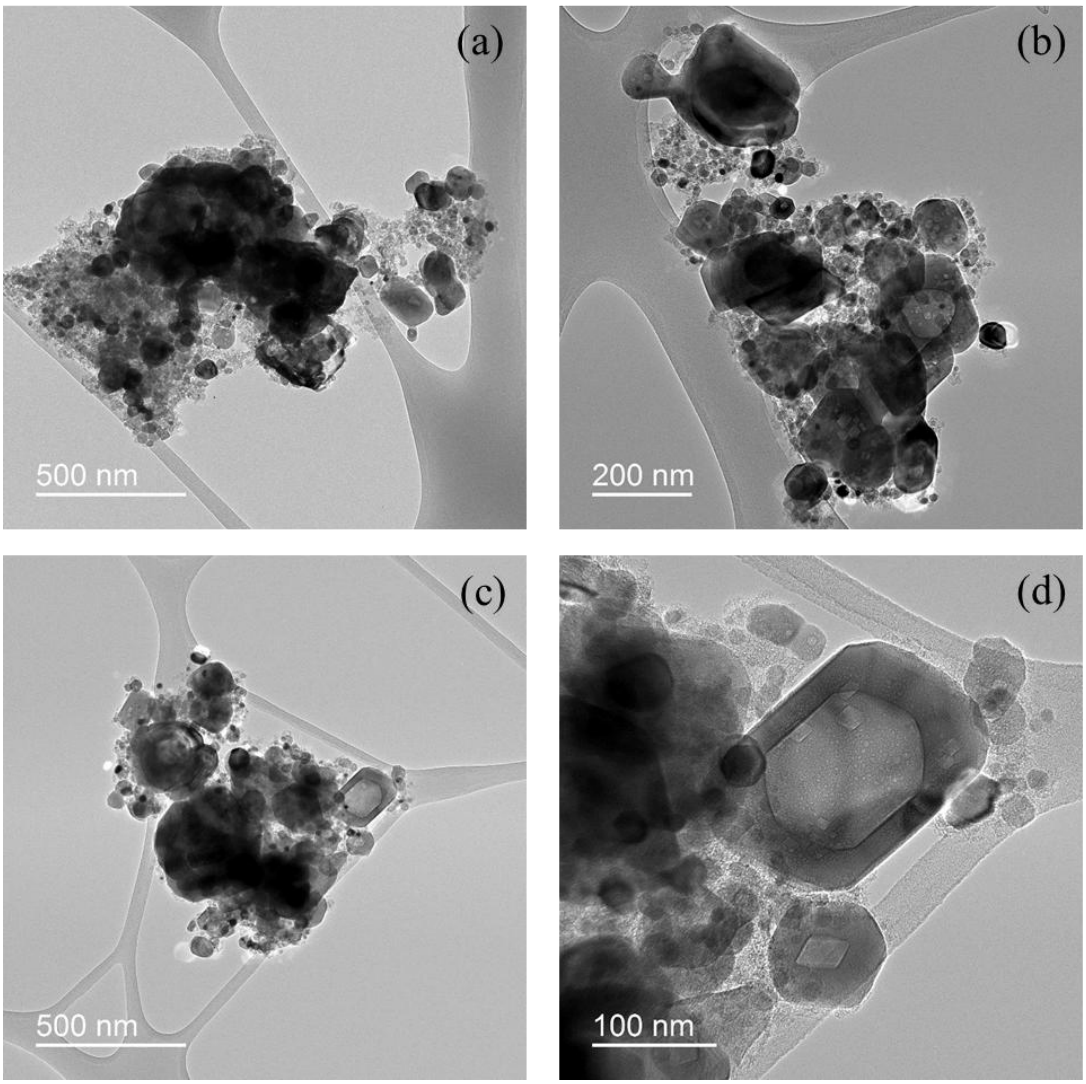


Figure 13. TEM micrographs of Zn-TiC-12h.

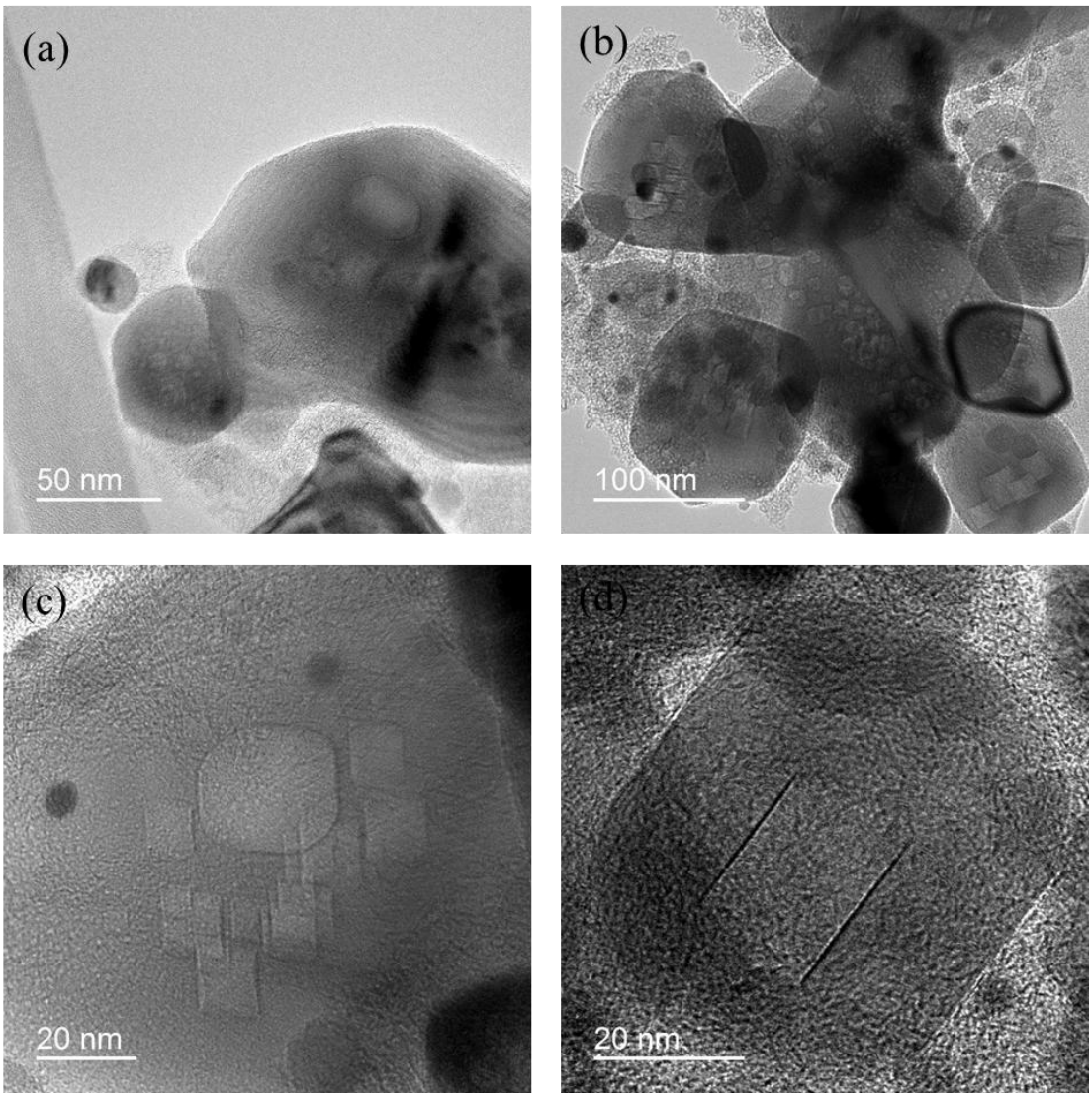


Figure 14. TEM micrographs of Zn-TiC-24h.

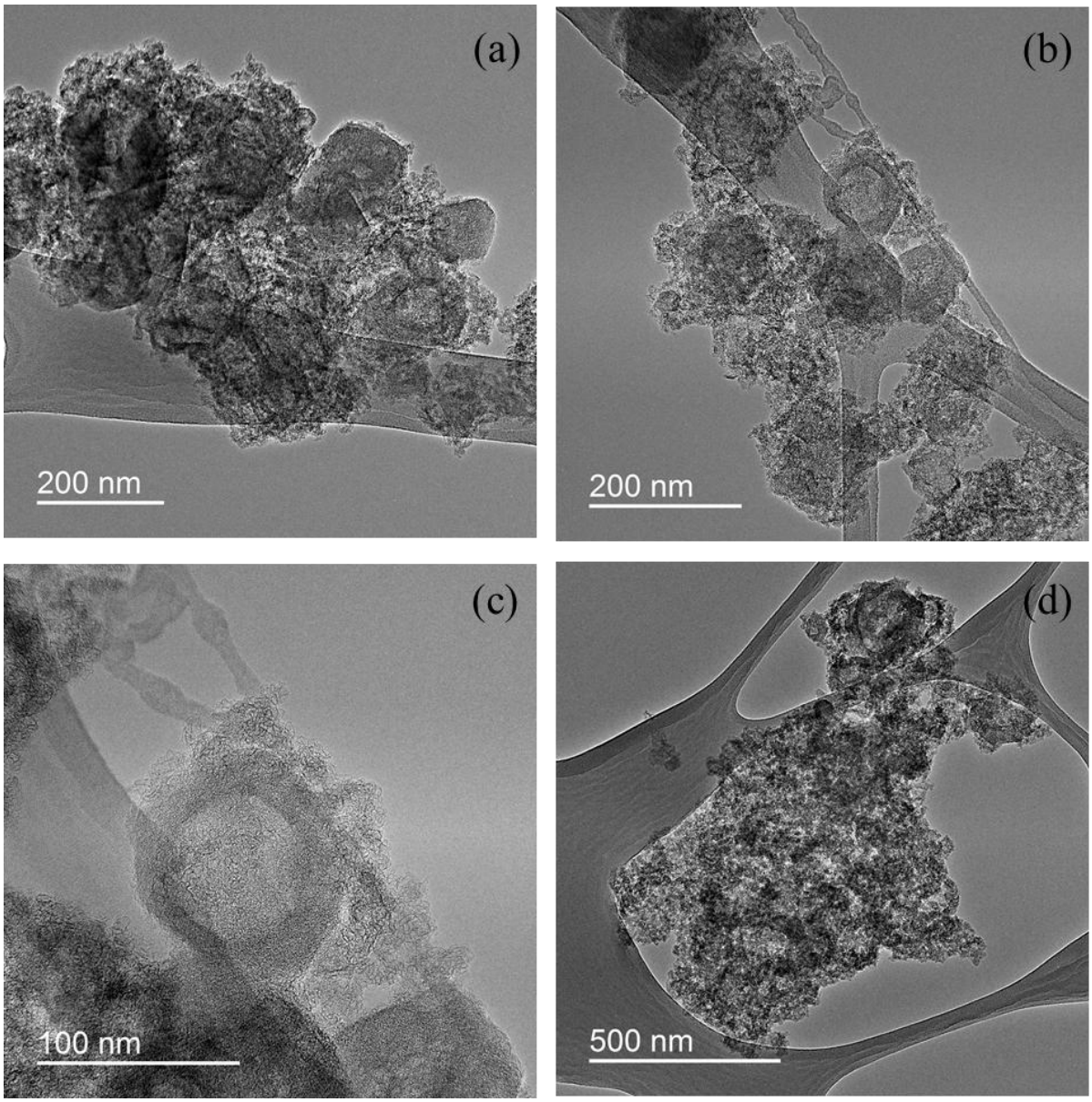


Figure 15. TEM micrographs of Zn-TiC-12h-CDC. CDC was obtained at 800℃.

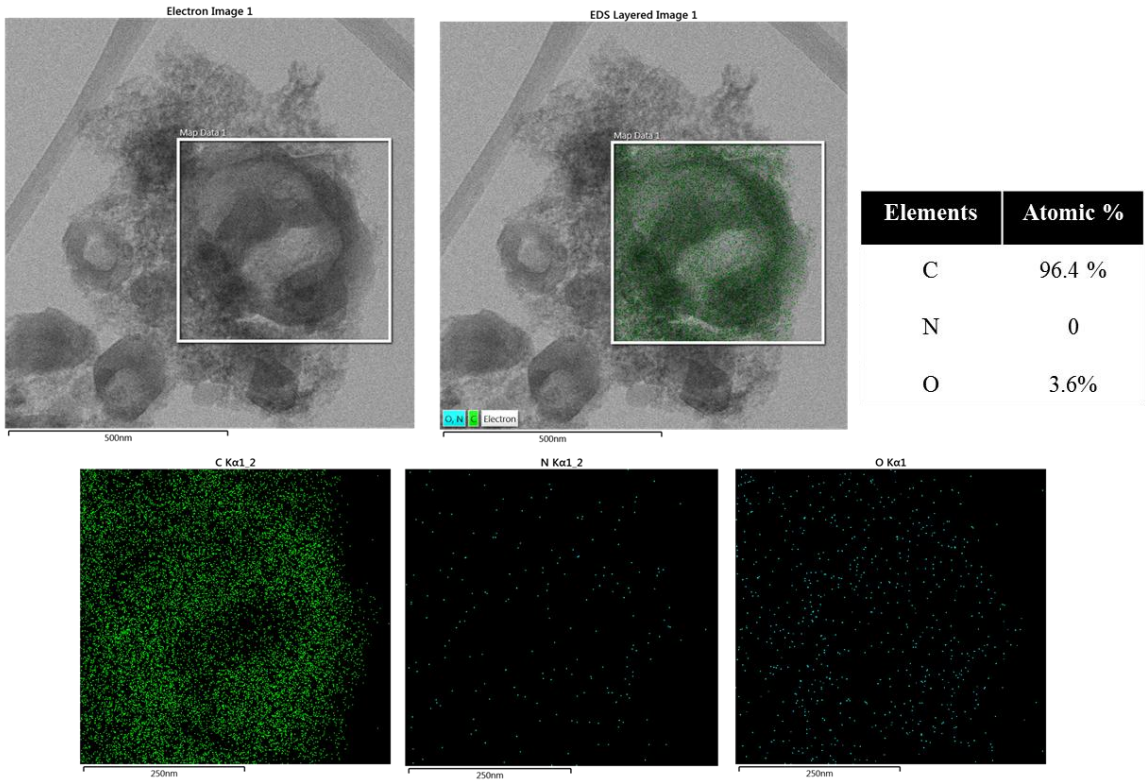


| Elements | Atomic % |
|---|---|
| C | 96.4 % |
| N | 0 |
| O | 3.6% |

Figure 16. TEM image and EDS mapping of Zn-TiC-12h-CDC. Elemental composition is obtained by EDS result; C: 96.4%, O: 3.6%, and N: 0 % (atomic percent)

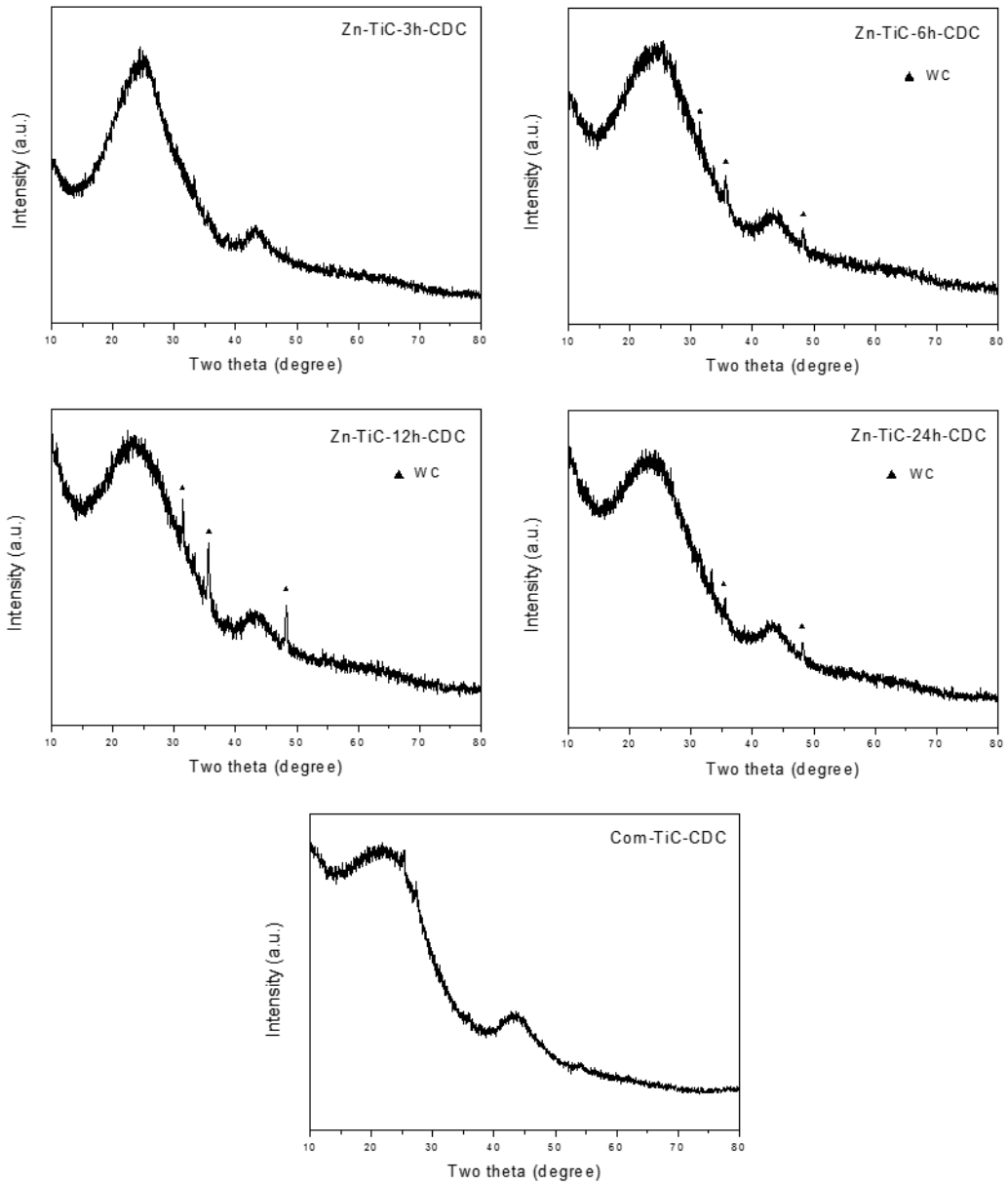


Figure 17. XRD results of Zn-TiC-X-CDC (X: 3h, 6h, 12h, 24h) and TiC-CDC. All CDC were obtained at 800℃.

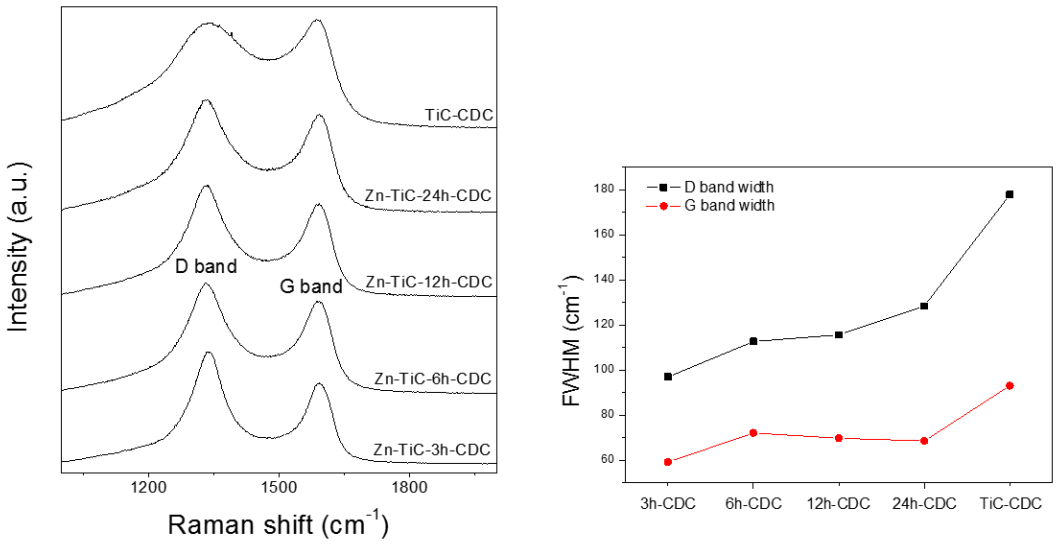


| | D band ($cm^{-1}$) | Band width($cm^{-1}$) | G band ($cm^{-1}$) | Band width($cm^{-1}$) |
|---|---|---|---|---|
| TiC-CDC | 1341 | 177.8 | 1587 | 93.0 |
| Zn-TiC-3h-CDC | 1339 | 96.9 | 1595 | 59.1 |
| Zn-TiC-6h-CDC | 1332 | 112.7 | 1591 | 72.1 |
| Zn-TiC-12h-CDC | 1332 | 115.6 | 1592 | 69.7 |
| Zn-TiC-24h-CDC | 1334 | 128.4 | 1596 | 68.5 |

Figure 18. Raman spectra of D and G band of ZnTiC-X-CDC and TiC-CDC and their FWHM. D and G band position and FWHM are summarized in the table.

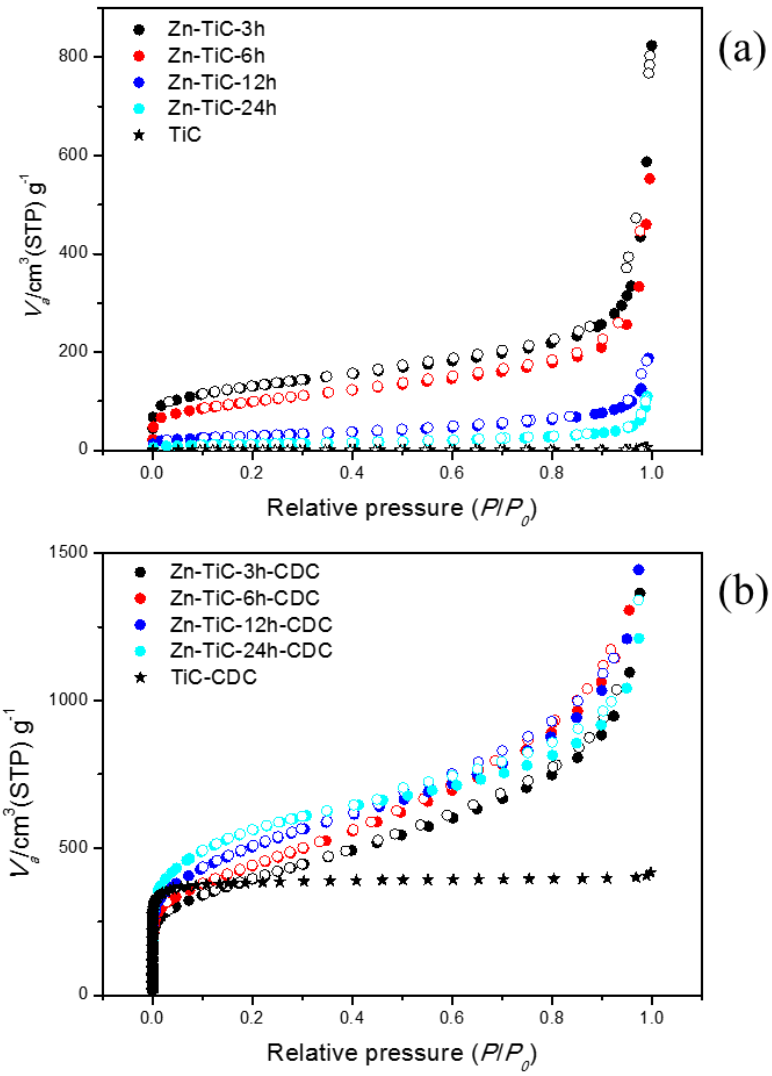


Figure 19. $N_2$ sorption isotherms of Zn-TiC-Xs and TiC (a), Zn-TiC-X-CDC and TiC-CDC (b). X means synthesis temperatures for carbide.

| Samples | SSA ($m^2/g$) | Total pore volume ($cm^3/g$) | Micro pore volume ($cm^3/g$) | Meso pore volume ($cm^3/g$) |
|---|---|---|---|---|
| TiC | 2 | - | - | - |
| $ZnTiO_3$ | 3 | - | - | - |
| Zn-TiC-3h | 464 | 0.95 | 0.18 | 0.46 |
| Zn-TiC-6h | 353 | 0.75 | 0.13 | 0.35 |
| Zn-TiC-12h | 104 | 0.27 | - | 0.13 |
| Zn-TiC-24h | 44 | 0.17 | - | - |
| TiC-CDC | 1439 | 0.63 | 0.58 | 0.04 |
| Zn-TiC-3h -CDC | 1402 | 3.32 | 0.53 | 1.66 |
| Zn-TiC-6h -CDC | 1561 | 3.63 | 0.58 | 1.65 |
| Zn-TiC-12h -CDC | 1803 | 3.10 | 0.67 | 1.23 |
| Zn-TiC-24h -CDC | 2025 | 2.63 | 0.76 | 1.01 |

Table 1. Pore characteristics of synthesized TiC, $ZnTiO_3$, Zn-TiC-X, Zn-TiC-X-CDC.

Specific surface area (SSA) was derived by BET equation. The total pore volume was measured up to $P/P_0$ =0.99. Micro and mesopore volumes were measured up $P/P_0$ =0.1 and 0.1< $P/P_0$ <0.95.

## 3.2. Titanium carbonitride-derived Micro- and mesoporous N-doped carbon

### 3.2.1. Motivation

Since chlorine react with $Ti(C_xN_{1-x})$ layer by layer, as formed $TiCl_4$ is vaporized carbon remained as the forms of C-C and C-N bonds. However, because C-N bonds are unstable at high temperature, decomposition occurs as a form of $CN_x$ and $N_2$, which resulted in additional pore generation from meso- to macropore depending on the nitrogen contents in $Ti(C_xN_{1-x})$. As nitrogen content increases remaining carbon is gasified with increasing temperature due to severe decomposition of C-N bonds which results in collapse of microporous structure, and hence meso- and macropore were developed without micropore. Therefore, in this dissertation, $Ti(C_{0.7}N_{0.3})$ was chosen for synthesizing the porous carbon with hierarchical pore structure.

### 3.2.2. Synthesis of Micro- and mesoporous N-doped carbon

Through the Chlorination of $Ti(C_{0.7}N_{0.3})$, theoretically carbon should remain with nitrogen as retaining its disordered structure by desorption of $TiCl_4$. But thermally unstable bonds between carbon and nitrogen lead decomposition as forms of $CN_x$ and $N_2$ gases, which

produce hierarchic mesopore, interconnecting a large volume of micropore of the carbon as shown in figure 20. As the content of nitrogen in the carbide increases, the yield, BET SSA, and micropore volume decrease because the amount of carbon decomposed after chlorination increases. For $Ti(C_{0.3}N_{0.7})$, it yielded less than 1% and low BET SSA of less than 100 $m^2/g$. For this reason, the composition of $Ti(C_{0.7}N_{0.3})$ was chosen for synthesizing carbon material. We call this carbon a CN in this dissertation. Samples are denoted as CNX, where X represents the chlorination temperature.

Field emission-scanning electron microscopy (FESEM) and transmission electron microscopy (TEM) were analyzed to study the structure evolution as the chlorination temperature increases. Figure 21 shows the FESEM images of the $Ti(C_{0.7}N_{0.3})$ precursor and their corresponding CN700 produced by chlorination at 700 ℃. Since $Ti(C_{0.7}N_{0.3})$ has a cubic structure, an angular and flat (100) surface is developed and a large amount of step bunching is found on the surface. As CN700 retained $Ti(C_{0.7}N_{0.3})$'s original angular shape and size, in particular, step edge surface of precursor. This result implies that conformal-like transformation occurs, similar to that in the formation of CDC [82]. According to FESEM of figure 22, there was no significant difference in the shape of particles even when the synthesis temperature was increased. However, CN800 synthesized at 800 ℃ has holes in the range of 10~50 nm, which appears to be caused by decomposition of $CN_x$ [83]. It is interesting to note that the surface of the $Ti(C_{0.7}N_{0.3})$ on which the (100) surface changed to (111) surface on the ledge after the chlorination reaction [84]. At higher temperature, as carbon ordering occurs a large hole in range of 200 nm is observed in some part (figure 22b and 22c). TEM shows that the surface of $Ti(C_{0.7}N_{0.3})$ has a step edge morphology as indicated by arrow in figure 23a and is terminated by carbide lattices without graphite layers (figure 23b). Surprisingly in CN300, synthesized at 300 ℃, step edge surfaces were clearly observed

where the graphite layers were grown, which has thickness of approximately 2 nm. But inside the particle, formed carbon were relatively disordered. (fig. 23c). It is interesting that the graphite layer formed at a low temperature of 300 ℃ is different from amorphous carbon synthesized from other materials at similar temperatures. Particularly in typical CDC, at such low temperatures, carbon is predominantly disordered and graphite begins to form at temperatures above 1200 ° C. It is believed that high crystallinity is observed despite the low temperature because there are many broken bonds and defects at the step edge surface which can nucleate the graphene. Figure 24 shows the development of graphene on the surface of SiC at 1400~2000 ℃ under high vacuum condition. In the scheme image, silicon atoms at the step position are easily sublimed and the carbon forms curved graphene. The graphene nucleated around the step grows along the terrace region as silicon atoms sublime further. Similar mechanism also applies to CN systems except that nitrogen further promote graphite nucleation. Surface of CN300 consists of fragmented and curved graphite layers, and disordered carbon inside and graphite are interconnected each other (fig. 23d). Figure 25 shows the structure evolution of CNX as the chlorination temperature increases. In CN700 graphite layers were more curved and thicker to 3.5~5 nm and more increased to 5~5.5 nm in CN800. From CN900 these graphite layers are interconnected along with particle surface. This layers were thicker into 8~20 nm showing as a hollow type (fig. 25c,d). As chlorination temperature increases, fragmented graphite layers interconnect as one structure and inside the particle relatively disordered carbon also ordered making uniformity.

Figure 26 shows the X-ray diffraction (XRD) spectra of the synthesized CNs. Sharp (002) and broad (10) peaks were observed, which are characteristic of turbostratic structure [32]. A sharp shoulder peak from CN700, observed around 26–27°, represents well crystallized graphite layers developed on the surface of CN. As synthesis temperature increases, broad

(002) plane become uniform. This result is in good agreement with TEM results that showed long graphite layers, which were interconnected by fragmented graphite layers. This long graphite layers was also verified by crystallized (10) plane. Average distance of graphite layers of CNX was plotted in the figure 27. CN 300 showed about 2 nm thickness of layers and it increased to 5.5 nm as graphite layers nucleated at the step edge. This thickness decreased from CN900 and CN1000 as fragmented graphite layers become long graphite layers. Raman spectroscopy shown in figure 28 showed that decrease in FWHM is observed as synthesis temperature increases. In the case of the CN300, there was a crystalline graphite layer clearly visible in the TEM, but the Raman result showed broad D and G bands representing disordered carbon. This is because the carbon inside the particles is almost amorphous. From the samples synthesized at 700 ℃, 2D band is arose, which is caused by the interactions between layers of graphite. As the temperature increases, the FWHMs of D and G bands narrow and the 2D band becomes well developed, which corresponds to the TEM and XRD results above. TiC-CDC typically requires the temperature of greater than 1200 ℃ to be well graphitized, whereas titanium carbonitride-derived carbon show well developed graphite layers even from 300 ℃ due to step edge and $CN_x$ decompositions, which seem to nucleate and promote the graphitization. Zeta potential measurements were performed on CNs and TiC-CDC. Zeta potential of all the powders were strongly related to pH values. At low pH, the particles were positively charged by protonation, which is beneficial for attracting the anionic metal complexes. In contrast, the particles were negatively charged at high pH. The isoelectric points ($pH_{PZC}$), where the zeta potential is zero, of TiC-CDC, CN700, CN800, CN900, and CN1000 were pH 5.9, 6.3, 6.4, 7.6, and 10.1, respectively. In CNs, as synthesized temperature increased, these values increased. This

comes from the basicity of carbon, which could be attributed to the π-electrons on the graphitic basal planes, and/or basic oxygen functional groups [85].

X-ray photoelectron spectroscopy (XPS) spectra (Fig. 29a) were conducted for the comparison of the chemical composition and bonding properties of CNs produced by chlorination at different temperatures, and Table 2 summarizes the XPS data. CN700, CN800, CN900, and CN1000 exhibited nitrogen contents of 3.14 wt%, 3.72 wt%, 2.67 wt%, and 2.17 wt%, respectively. The N 1s peak was deconvoluted into two types of configuration: pyrrolic-N (400.37 ± 0.2 eV) and oxidized-N (402–404 eV), which mainly consists of N-oxides of pyridinic-N (402.06 ± 0.3 eV) [86]. Given that these functional groups were invariably located at the edges sites, the CNs synthesized seems to consist of a large amount of edges caused by the development of pores [87]. As indicated by elemental analysis (EA), which provides the bulk composition, nitrogen contents were higher than those observed from XPS results. As the surface can be easily contaminated by oxygen, the relative nitrogen content at the surface decreased. On the other hand, a previous study has demonstrated that pores in CDC are developed not only at the surface but also throughout the bulk. Moreover, edges along the pore growth of the bulk seem to be desired sites for an edged-nitrogen doping. Micro-pores are formed in pure carbide systems, while micro- and meso-pores are formed in carbonitride systems. Pores grow over by the decomposition of unstable C–N bonds, such as pyrrolic-N (5-membered ring), while stable nitrogen bonds, such as pyridinic- or graphitic-N (6-membered ring), are retained, or unstable bonds are converted to stable bonds on the pores [40]. In CN700, pyrrolic-N was well developed, but it dramatically decreased with temperature. Moreover, in all CNs, pyridinic-N transformed into N-oxides of pyridinic-N on the surface [86], as can be observed in the XPS C1s spectra, oxidized carbon bonds were dominant, featuring one-sided double peaks. The intensity of all C-C bonds (284.5 eV) was

weaker than those of C-O bonds (～286 eV), because the existing dangling bonds or highly positive charged carbon induced by the unstable nitrogen functional group on the surface pores is subjected to contamination by oxygen at low temperature [11]. The C1s spectra were de-convoluted as follows: 286.16 ± 0.1 eV (C-N-O), 286.60 ± 0.3 eV (C-O), 287.51 ± 0.3 eV (C=O), and ～289 eV (O-C=O) [89]. All CNs exhibited high amount of oxidized carbon bonds on the surface; on the other hand, CN1000 exhibited a noticeable C-N peak (285.6 eV) [90], with an increase in the number of C=C bonds, caused by the involvement of graphitic nitrogen (402.1 eV) originating from the evolution of pyrrolic- or pyridinic-N. The XPS results for nitrogen were in good agreement with the results obtained from Fourier transform infrared spectroscopy (FTIR) analyses (Fig. 29b). Bands were observed at 3430 $cm^{-1}$ and 1600 $cm^{-1}$, attributed to N-H symmetric stretching vibration and N-H in-plane deformation vibrations or C=C stretching vibration, respectively. Furthermore, a peak was observed at 1260 $cm^{-1}$, attributed to C-N stretching vibration.

Figure 30 shows the $N_2$ sorption isotherms, which indicate the pore characteristics of CNs. CN700 exhibited a type-I isotherm with a mild slope $P/P_0$ of 0.1–0.5, which corresponds to the development of not only micro-pores also small meso-pores, which is comparable to pure CDC synthesized at much higher temperature [11]. Unlike typical products derived from CDC, CN700 exhibited a small meso-porous region by the further desorption of gases other than $TiCl_4$. CN800 and CN900 exhibited high amounts of adsorbed $N_2$, particularly for the well-developed meso-porous region, whereas the $N_2$ adsorption of CN1000 decreased because of the partial collapse of the pore network with the growth of graphitic layers into longer ones. Moreover, from synthesis temperature 900 ℃ (CN900 and CN1000), sorption isotherms changed into Type H3 and H4 hysteresis loops, which are indicative of slit-shaped

pores [91]. CNs, which have a pore-forming agent similar to that of CDC, exhibited randomly developed pore structure, with a high surface area (>1000 $m^2/g$), as calculated by the Brunauer–Emmett–Teller (BET) model. With respect to the pore characteristics, CN800 exhibited the highest total pore volume with highest micro-pore volume. On the other hand, the surface area of CN1000 significantly dwindled with the decrease of its micro- and meso-pore volumes, caused by irregular pore structure. All of the textural properties are summarized in Table 3.

As shown in Figure 31, the pore size distribution (PSD) of CNs, which is calculated by the non-local density functional theory (NLDFT), are varied upon chlorination temperature. The pore size of CN700 were centered at 0.7 nm, which is a characteristics of TiC-derived carbon [92]. Meanwhile, those of 1.5 nm and 3.0 nm, are believed to be affected by $CN_x$ desorption. CN700 exhibited a uniform tri-modal distribution. With the increase of synthesis temperature, the pores, centered at 0.7 nm and 1.5 nm, collapsed because of the high stress increased by the curved graphitic layer, thereby leading to irregularity. For CN1000, large pores with a diameter of 20–100 nm were well developed, while the total pore volumes decreased.

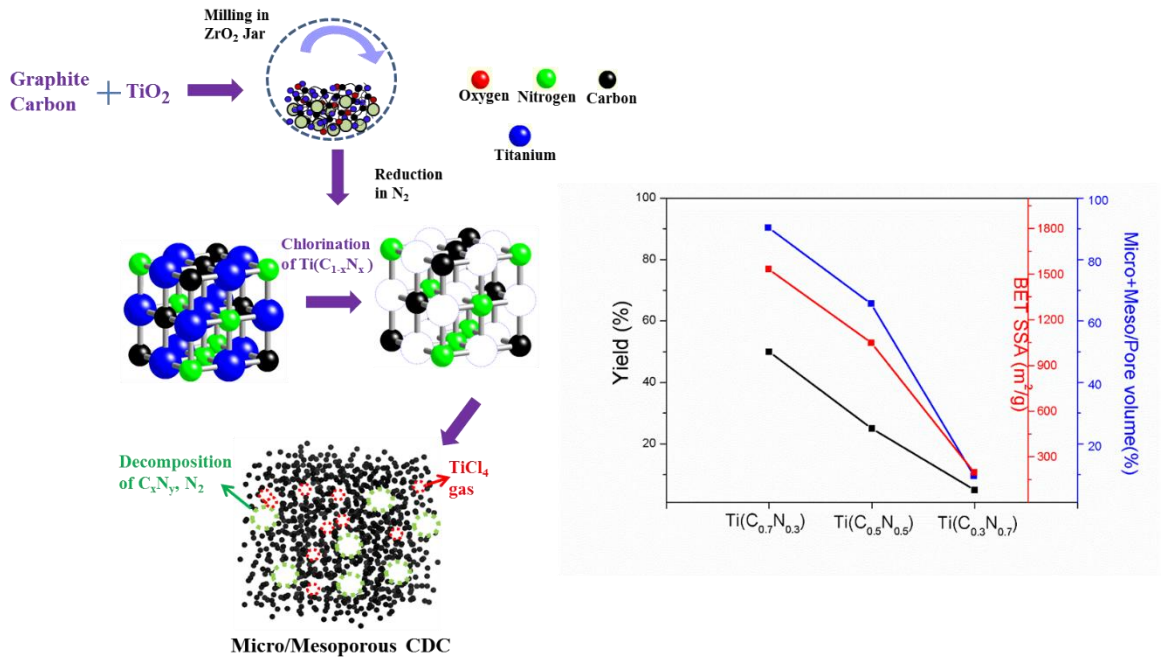


Figure 20. Scheme of micro- and mesoporous N-doped carbon. As nitrogen content in $Ti(C_xN_{1-x})$ increased, yield, BET SSA, and micro pore volume decrease after chlorination.

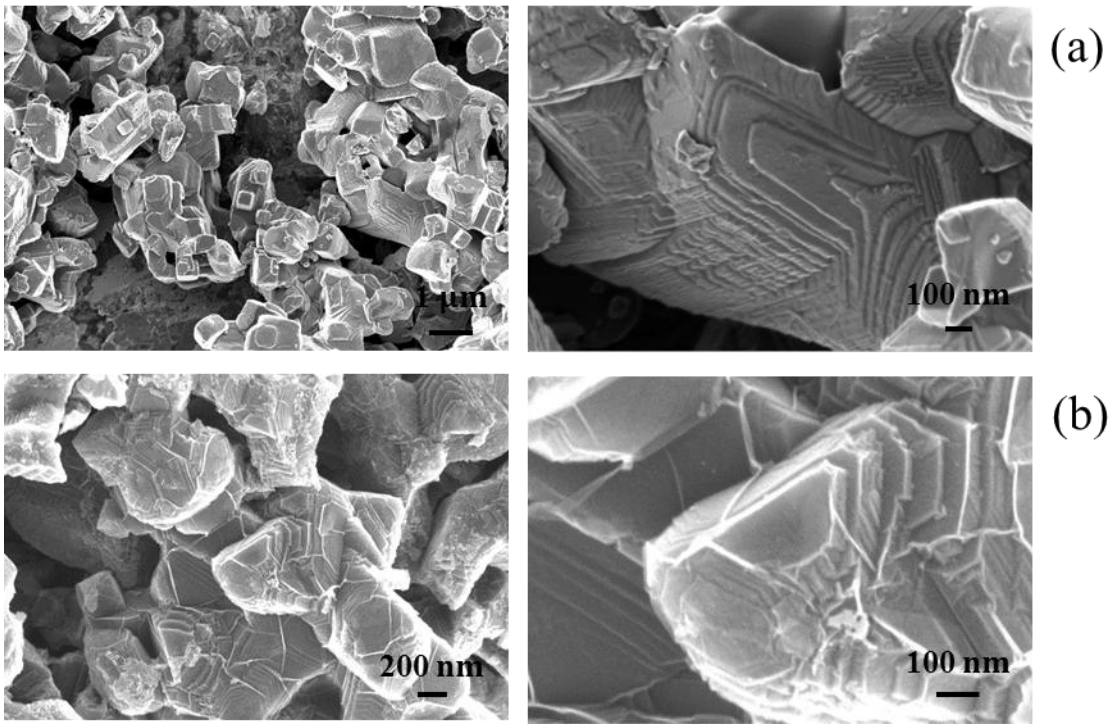


Figure 21. Field Emission Scanning Electron Microscopy (FESEM) images of $Ti(C_{0.7}N_{0.3})$ (a) and CN700 (b).

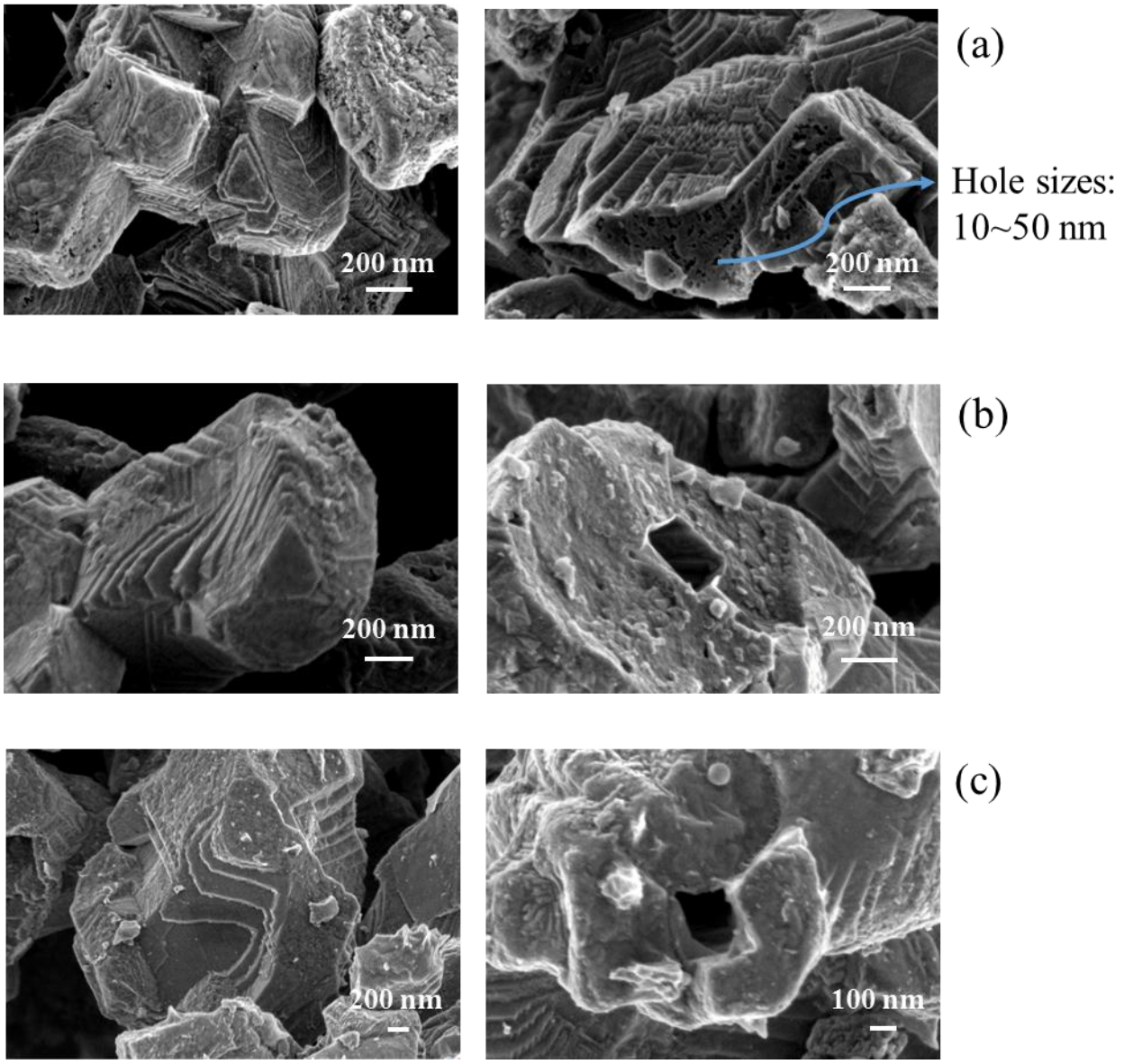


Figure 22. Field Emission Scanning Electron Microscopy (FESEM) images of CN800 (a), CN900 (b), and CN1000 (c).

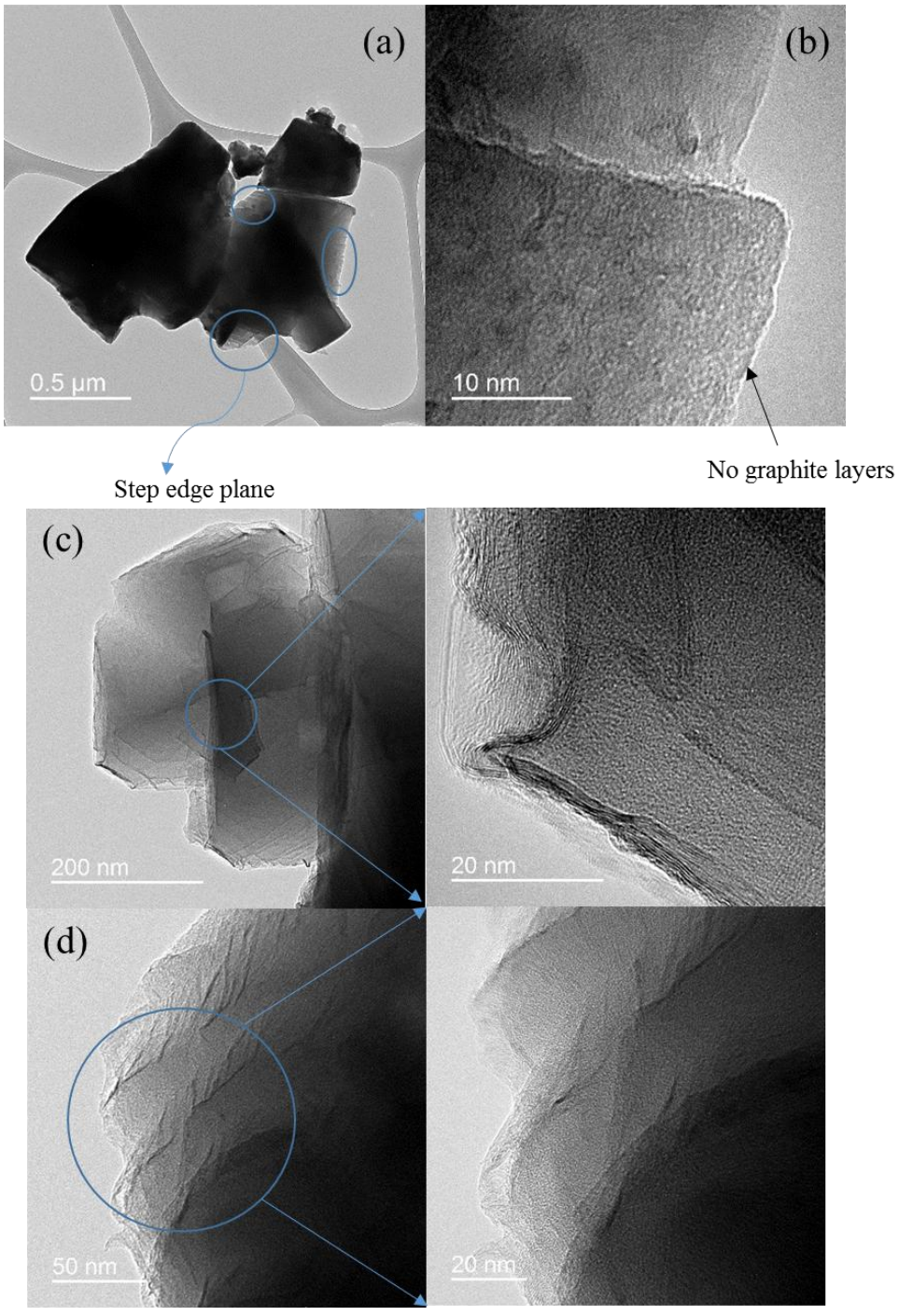


Figure 23. Transmission Electron Microscopy (TEM) images of Ti($C_{0.7}N_{0.3}$) (a, b) and CN300 (c, d).

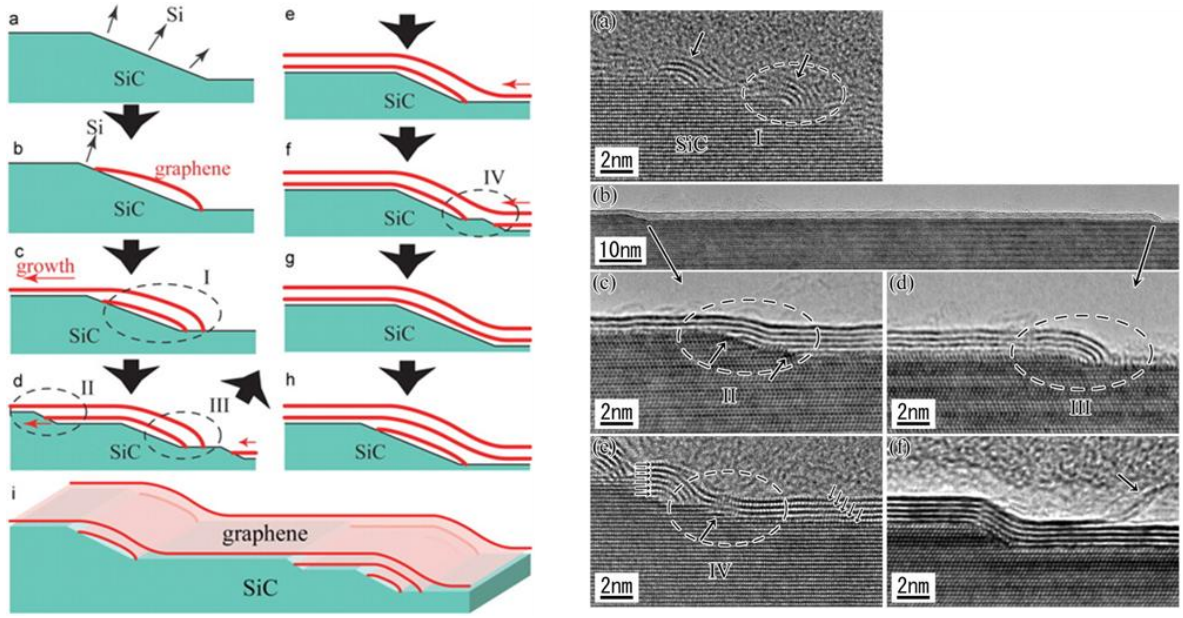


Figure 24. Scheme and Transmission Electron microscopy (TEM) images of SiC-derived graphene (Data from reference [100])

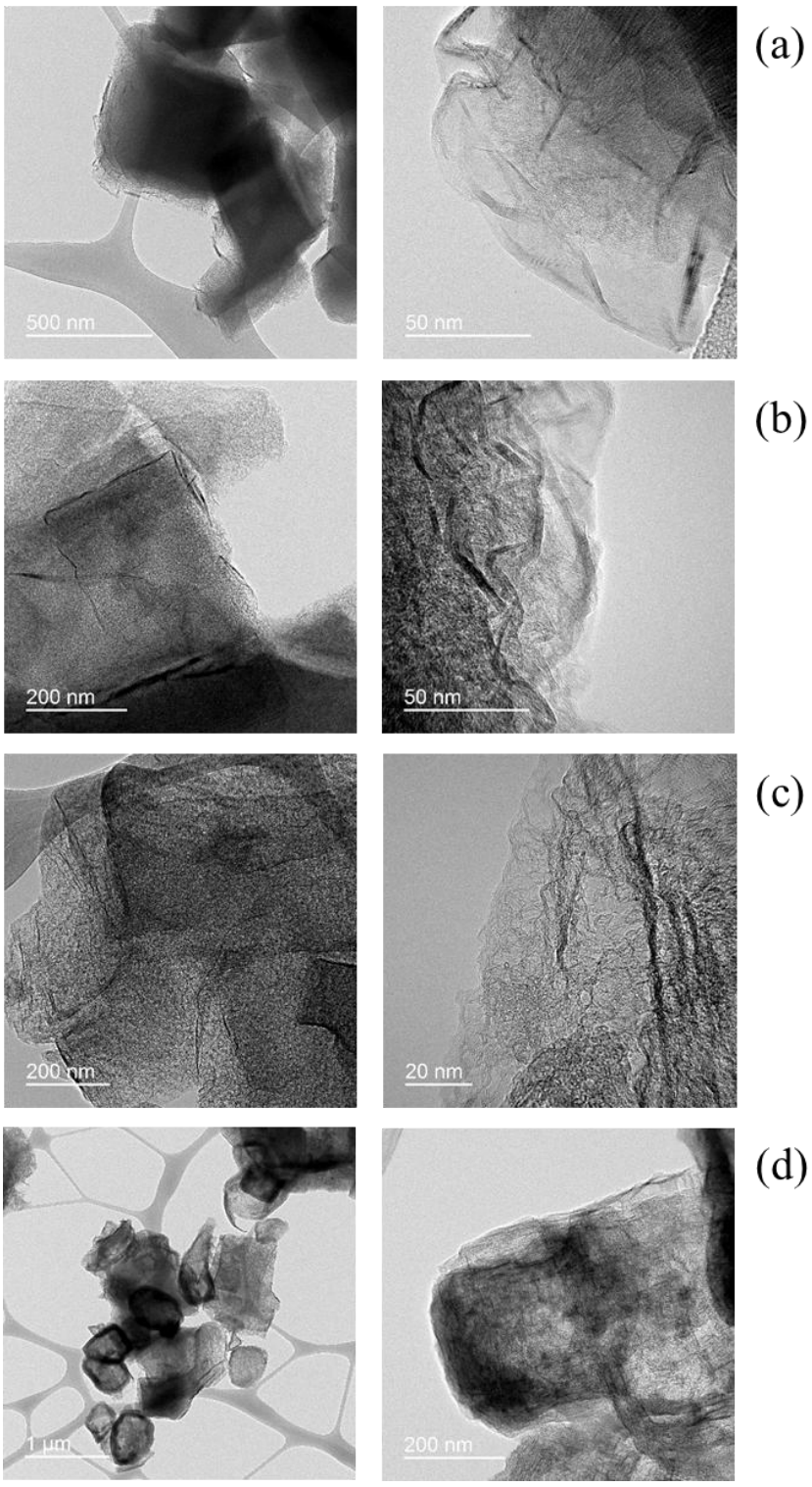


Figure 25. Transmission Electron Microscopy (TEM) images of CN700 (a), CN800 (b), CN900 (c), and CN1000 (d).

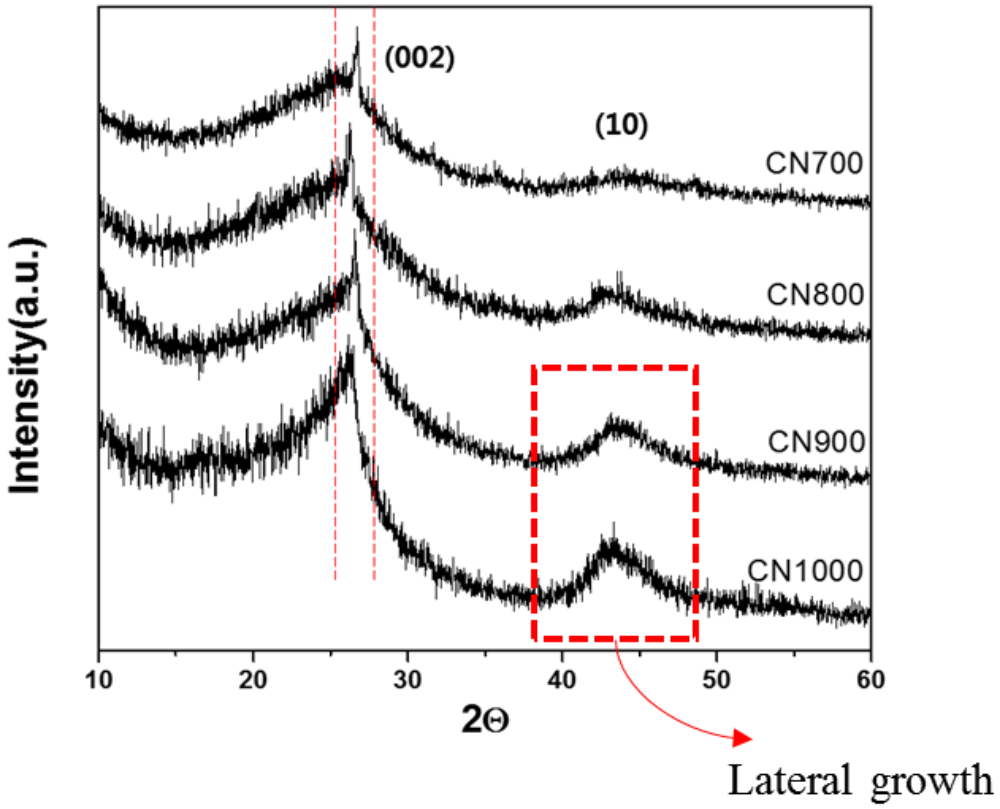


Figure 26. X-ray diffraction results of CN700, CN800, CN900, and CN1000.

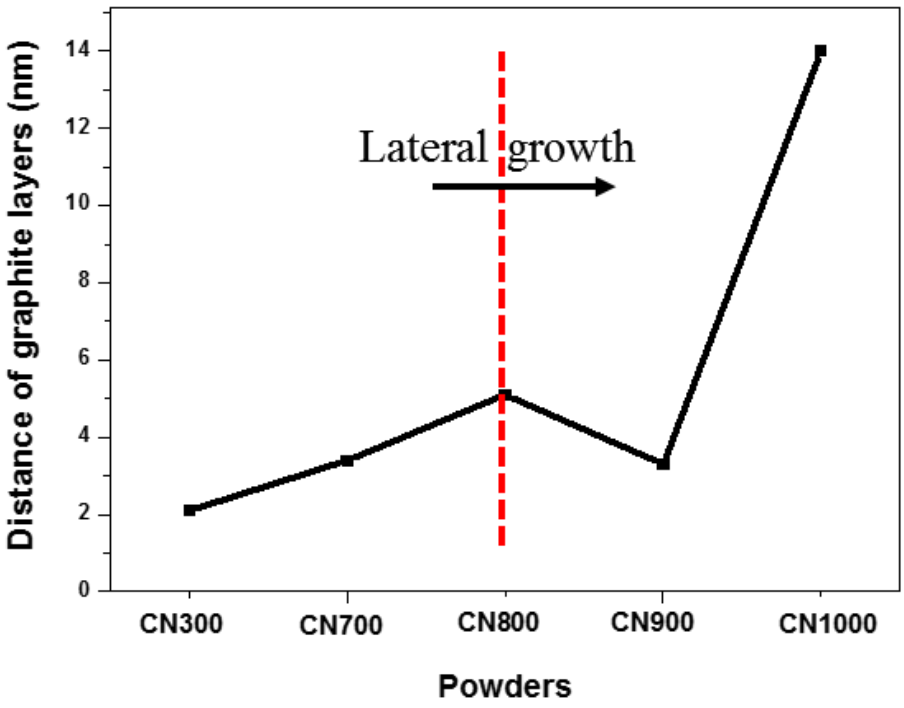


Figure 27. Average distance of graphite layers of CN300, CN700, CN800, CN900, and CN1000.

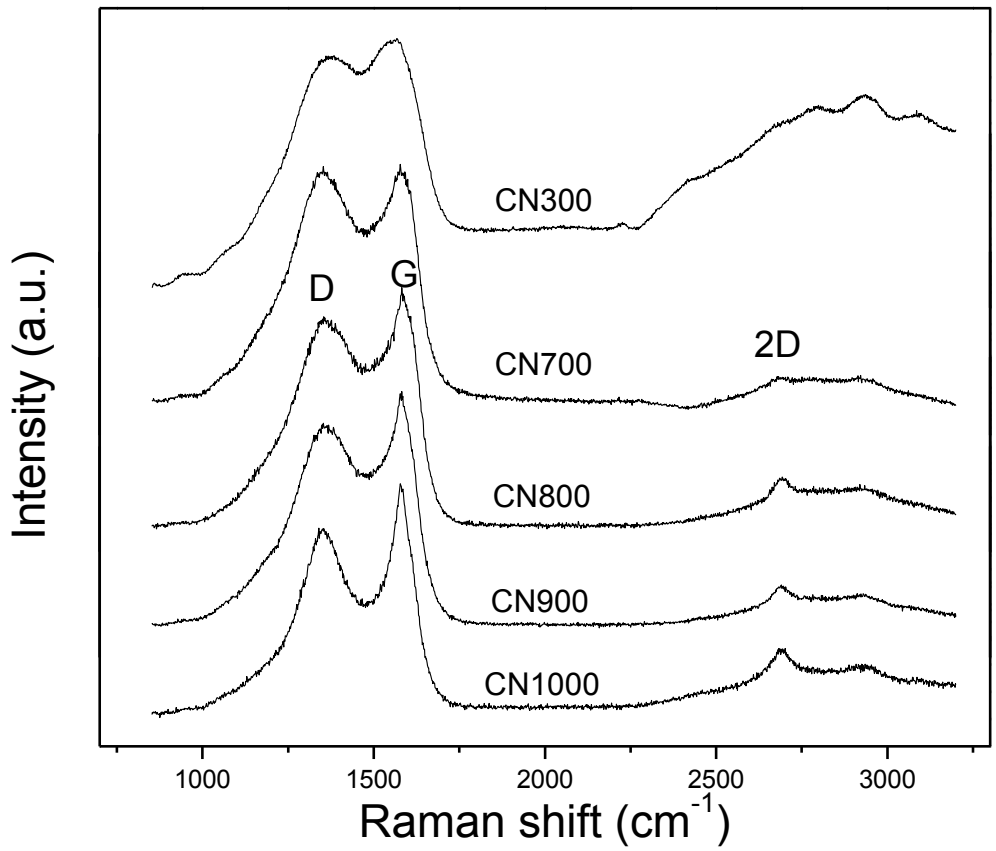


Figure 28. Raman spectra of CN300, CN700, CN800, CN900, and CN1000.

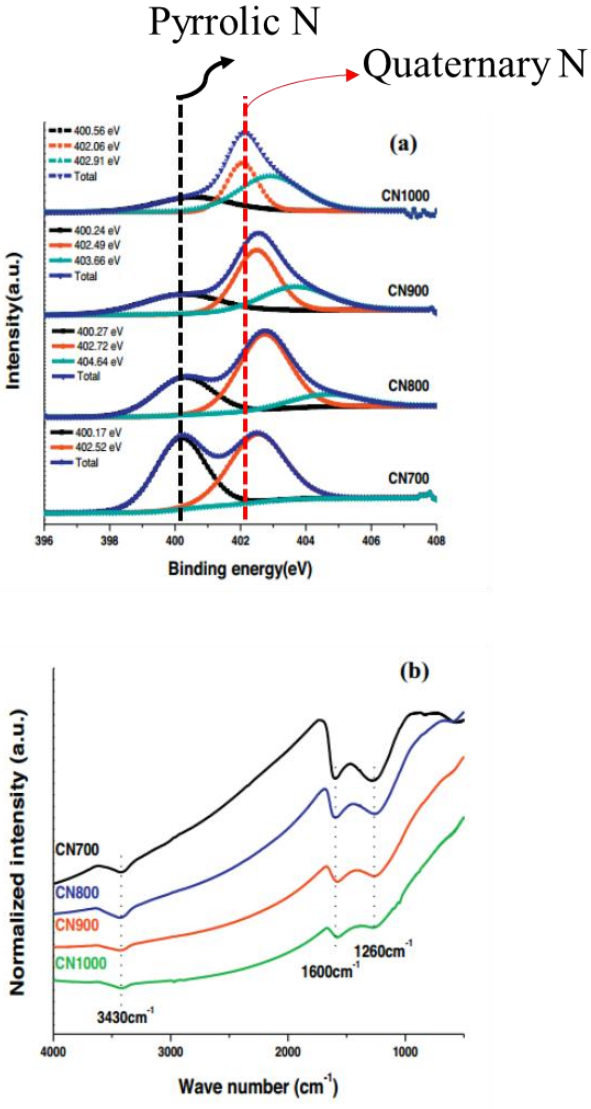


Figure 29. X-ray photoelectron spectroscopy (XPS) spectra (a) and Fourier transform infrared spectroscopy (FTIR) (b) of CN700, CN800, CN900, and CN1000

| Samples | C (wt. %) | N (wt. %) | O (wt. %) | H (wt. %) |
|---|---|---|---|---|
| CN700 | 80.77 (70.23) | 3.14 (13.43) | 14.71 (6.14) | (1.64) |
| CN800 | 84.24 (77.16) | 3.72 (9.44) | 10.71 (4.17) | (1.26) |
| CN900 | 84.08 (83.82) | 2.67 (6.70) | 12.78 (2.89) | (0.73) |
| CN1000 | 84.67 (86.84) | 2.17 (4.55) | 16.65 (1.27) | (0.36) |

Table 2. Chemical composition of CN700, CN800, CN900, and CN1000 (EA-parenthesis, XPS)

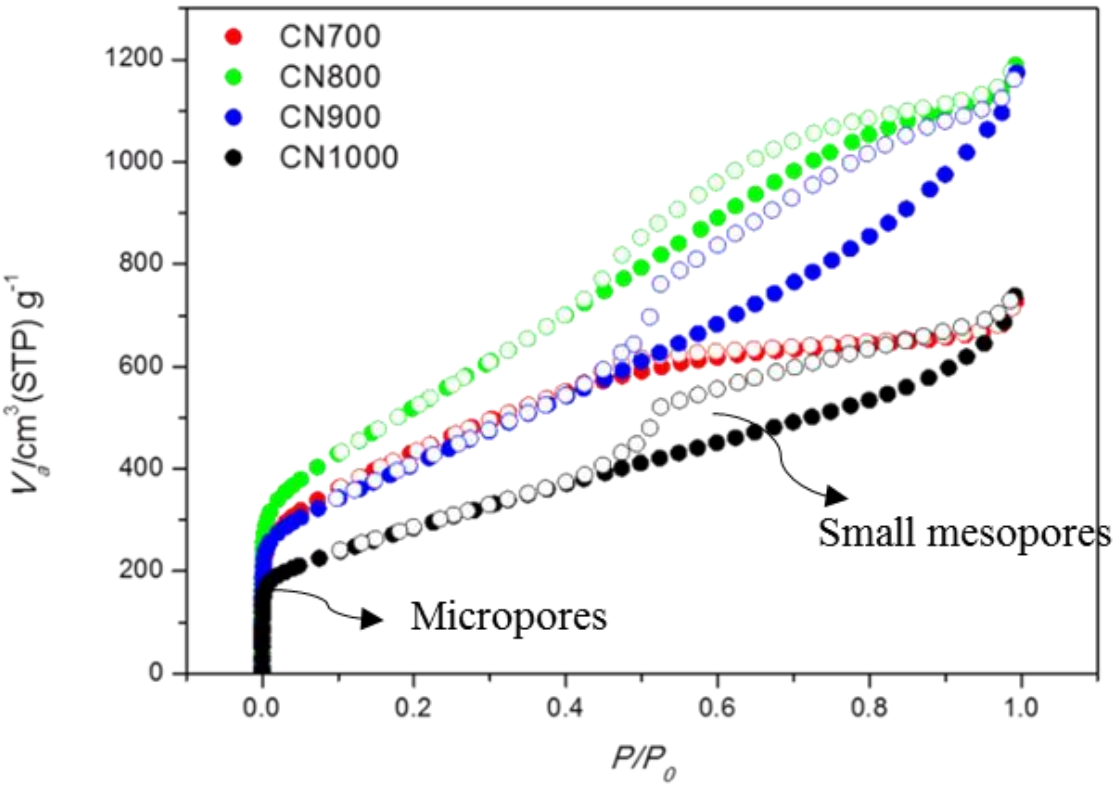


Figure 30. $N_2$ sorption isotherms of CN700, CN800, CN900, and CN1000 (solid–adsorption, open–desorption).

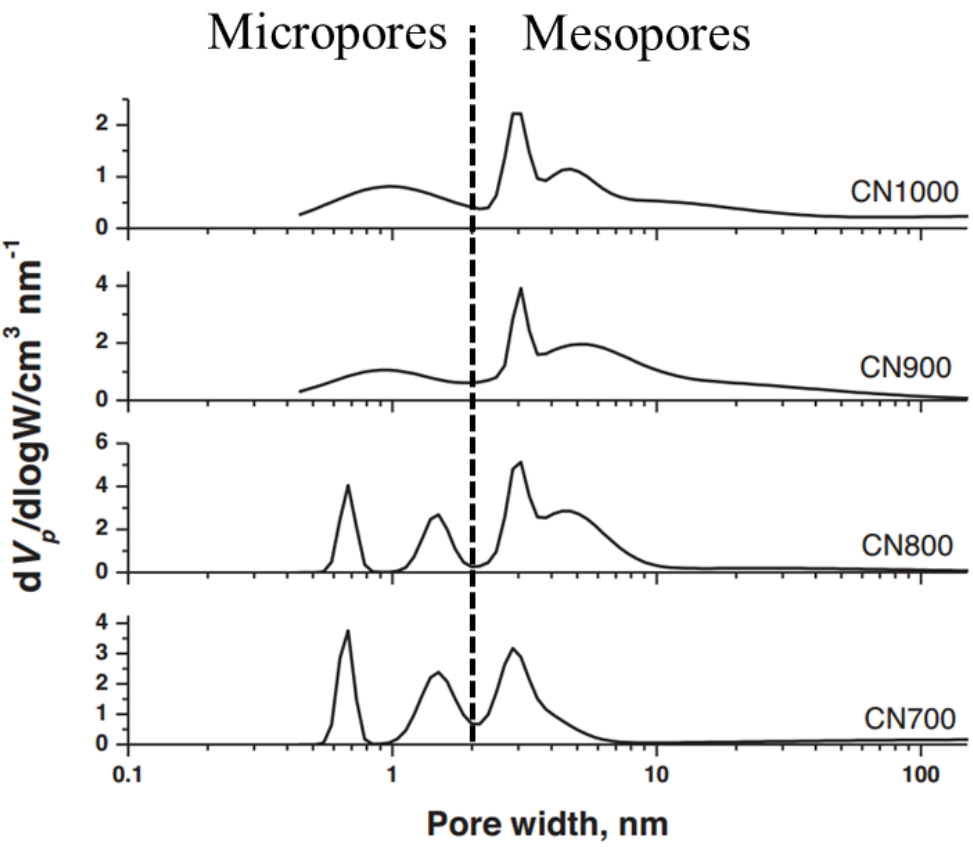


Figure 31. Pore size distribution (PSD) of CN700, CN800, CN900, and CN1000. It is calculated by Non-Local Density Functional Theory (NLDFT) (cylinder pore model).

| Samples | SSA ($m^2/g$) | Total pore Volume ($cm^3/g$) | Micro pore Volume ($cm^3/g$) | Meso pore Volume ($cm^3/g$) | Mean pore diameter (nm) |
|---|---|---|---|---|---|
| CN700 | 1572.3 | 1.1137 | 0.5594 | 0.4739 | 2.8332 |
| CN800 | 1922.8 | 1.8309 | 0.6642 | 1.0734 | 3.8088 |
| CN900 | 1496.2 | 1.7923 | 0.5284 | 1.1032 | 4.7916 |
| CN1000 | 1037.3 | 1.1349 | 0.3677 | 0.6284 | 4.3762 |

Table 3. Texture properties of CN700, CN800, CN900, and CN1000 measured by Nitrogen sorption isotherms at 77 K

### 3.2.3. Applicability of CNs for the treatment of arsenic-contaminated water

#### 3.2.3.1. Arsenic adsorption isotherm

The applicability of CNs for the treatment of arsenic-contaminated water was investigated by performing equilibrium batch adsorption tests. The arsenic adsorption isotherms of CNs are shown in Figure 32. CN700 exhibited a non-linear adsorption isotherm for the removal of arsenic. In addition, CN800 also exhibited a non-linear adsorption isotherm; however, the concentration of arsenic adsorbed on CN800 was lower than that adsorbed on CN700. Moreover, CN900 did not adsorb arsenic, but little in the low arsenic concentrations. On the other hand, CN1000 did not adsorb arsenic. This difference in the removal of arsenic among the CNs is probably related to their pore structure and surface functional groups. In light of reasonable adsorption isotherms of CN700 and CN800, it seems that micro-pores of 0.7 nm and high content of N are the reasons for higher As adsorption compared with CN900 and CN1000. To compare the arsenic adsorption properties of CNs with that of a typical CDC, an equilibrium adsorption test was also performed using TiC-CDC. The adsorption of arsenic on TiC-CDC was not significant, probably related to the negligible meso-pores and/or the absence of nitrogen functional groups. In addition, CNs shows much better As adsorption than that of activated carbon modified by polyaniline [93].

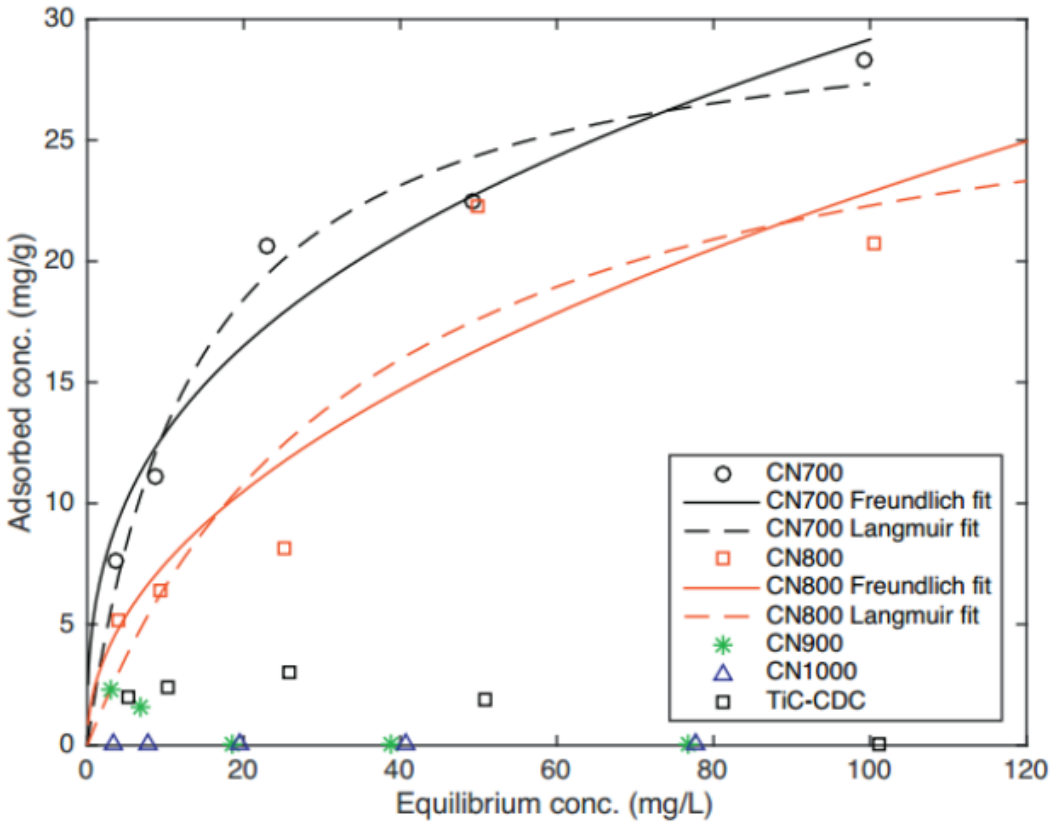


Figure 32. Comparison of adsorption isotherms of As on CNs (700, 800, 900, and 1000 ◦C) and TiC-CDC.

### 3.2.3.2. Quantification of adsorption property

To quantify the adsorption property of the CNs, the non-linear adsorption curves of CN700 and CN800 were fitted with the Freundlich and Langmuir adsorption isotherm models. Table 4 lists the estimated adsorption parameters. The fitting isotherms with the Freundlich model exhibited different values of n for CNs, suggesting different mechanisms of arsenic adsorption on CNs, although CNs are synthesized from the same starting material. This difference originates from the alteration of reactive sites by the synthesis temperature. The fitting isotherm of CN700 with the Langmuir model exhibited a maximum adsorption capacity of 31.08 mg/g, which is slightly higher than that of CN800, and it can be attributed to dominant content of pyrrolic-N in CN700 despite better surface properties of CN800, as shown in Figure 29a and Table 3. The maximum adsorption capacity decreased with increasing synthesis temperature from 700 to 1000 ℃ even though the surfaces of all the CNs were positively charged at pH 5 in the laboratory measurement condition. In general, arsenic removal is strongly dependent on the surface charge at low content of 1 ppm [85], but, according to adsorption isotherm of CN1000 which shows negligible As adsorption (Fig. 32) even though its surface charge shows the highest positive charge in the whole pH area, at high content of arsenic in aqueous solution surface charge does not seem to have great impact on arsenic removal. Instead, it does seem to be attributed to broadening pore size distribution and alteration of nitrogen functional groups of CNs. A similar effect of synthesis temperature on the surface property has been reported in previous studies conducted using activated carbon. Lua and Yang [94] have reported that a very high activation temperature results in the widening of the micro-pores to meso- and macro-pores, burn-off of the carbon structure.

Furthermore, Joupheop [95] has also reported the adsorption of arsenic on alumina and demonstrated a dramatic increase in adsorption with uniform meso-porosity via a templating method.

Adsorption parameters estimated by fitting Freundlich and Langmuir adsorption isotherms.

| | Freundlich | | | Langmuir | | |
|---|---|---|---|---|---|---|
| | $K$ | $n$ | $R^2$ | $q_m$ | $K_a$ | $R^2$ |
| CN700 | 5.724 | 2.828 | 0.9459 | 31.08 | 0.07283 | 0.9731 |
| CN800 | 2.474 | 2.072 | 0.8023 | 30.34 | 0.02771 | 0.8250 |
| CN900 | – | – | – | – | – | – |
| CN1000 | – | – | – | – | – | – |

Table 4. Adsorption parameters estimated by fitting Freundlich and Langmuir adsorption isotherms of CN700, CN800, CN900, and CN1000.

### 3.2.3.3. Adsorption mechanism of arsenic ion on CNs

We investigated the adsorption mechanisms of arsenic ion on carbon-based adsorbents. Arsenic ion assumes various complex structures in water; we assume the arsenic complex (AC) to be $H_2AsO_4^{-1}$, as the laboratory measurement conditions have a pH of approximately 5. As the reaction occurs in an aqueous environment, we included four water molecules surrounding AC in the calculations. The inclusion of these water molecules modifies the free energy of system; hence, it plays an important role in adsorption [96]. The adsorbate consists of AC and water molecules. In case of the adsorbent, we adopted two N-doping adsorbents—pyridine N-Oxide (NO) and pyrrolic N (PN)—based on the XPS spectrum and N-free adsorbent (NF) for elucidating the effect of nitrogen doping, as shown in Figure 33. Adsorption was evaluated by the difference of free energies, $\Delta G = G_{\text{adsorbent + adsorbate}} - (G_{\text{adsorbate}} + G_{\text{adsorbent}})$. The free energy is defined as $G = H - T \times S + \text{ZPE}$, where $H$, $T \times S$, and ZPE denote the enthalpy, product of temperature and entropy, and zero-point energy, respectively. All configurations were optimized by full relaxation with DFT calculations, and free energies were obtained for pre-optimized configurations using GAUSSIAN 09. Table 5 summarizes the differences of free energies for each adsorption process; $\Delta G$ of PN is negative, which represents an exothermic reaction; however, $\Delta G$ of NF and NO are positive, indicative of endothermic reactions. Figure 34a shows the optimized structure of AC on PN; AC was bound to the adsorbent by ionic bonds. Hence, electrostatic interactions are the main contributors to the adsorption of AC. Next, we analyzed the amount of charges on each atom using the Mulliken population method [97]. By comparing the amount of charges on all atoms in NF and PN, the effect of

the N atom was clearly revealed. In Figure 34a, two C atoms and H atom, which are connected to the pyrrolic N atom, were positively charged with 0.31e, 0.33e, and 0.35e, while pyrrolic N was negatively charged with −0.71e. The electrostatic interactions between these three positively charged atoms and negatively charged O atoms, the values of which were −0.78e, −0.79e, and −0.70e, respectively, in AC are the reason for the binding of AC to the adsorbent. In Figure 34b, O atoms in AC were negatively charged with −0.79e, −0.79e, and −0.70e, values similar to those in the previous case. However, the C atoms in the adsorbent are less positively charged than those of the atoms around the pyrrolic N atom, and electrostatic interaction between AC and C atoms in NF CC was not sufficiently strong so as to cause the binding of AC to the adsorbent. These theoretical results are consistent with experimental results shown in Figure 32, which indicate that the sample without the N atom (TiC-CDC) does not adsorb AC. Therefore, the N atom in the carbon-based adsorbent makes neighboring atoms positively charged, thereby reinforcing electrostatic interactions between AC and the adsorbent.

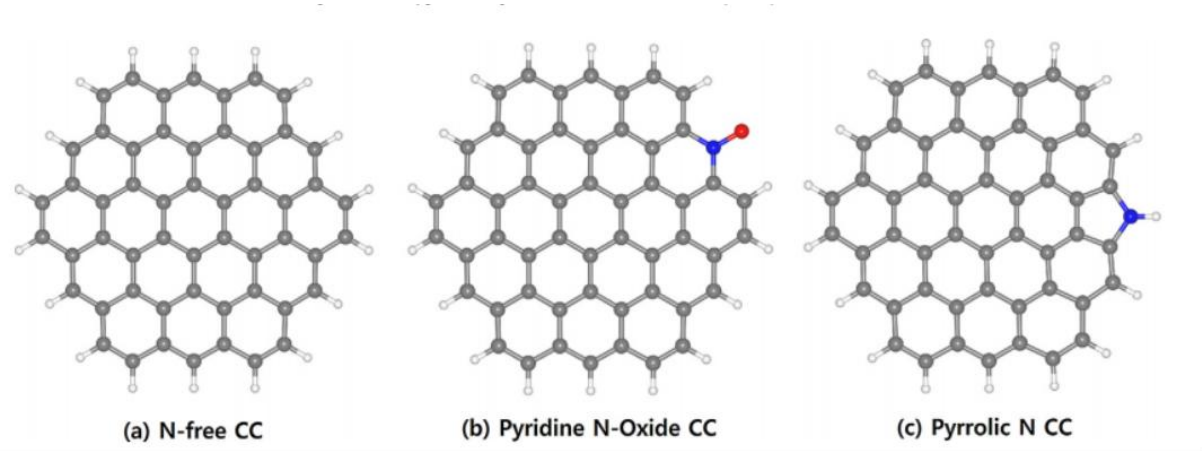


Figure 33. Three adsorbents are prepared from circumcoronene (CC), which is composed of 54 carbons and 18 hydrogen atoms with N-free (NF) (a), pyridine N-oxide (NO) (b), and pyrrolic N (PN) (c). Two N-doped adsorbents, NO and PN, are chosen based on the XPS spectra, 402.06 ± 0.3 eV and 400.37 ± 0.2 eV, respectively. Carbon, hydrogen, nitrogen, and oxygen atom are represented by gray, white, blue, and red balls, respectively.

| Adsorbent | $\Delta G$ (eV) | |
|---|---|---|
| Nitrogen-free CC | 0.36 | |
| Pyridine *N*-Oxide CC | 0.37 | |
| Pyrrolic N CC | −0.59 | Spontaneous reaction |

Table 5. Difference of free energy, $\Delta G$, for the adsorption on each adsorbent: N-free CC, pyridine *N*-oxide (NO) CC, and pyrrolic N (PN) CC.

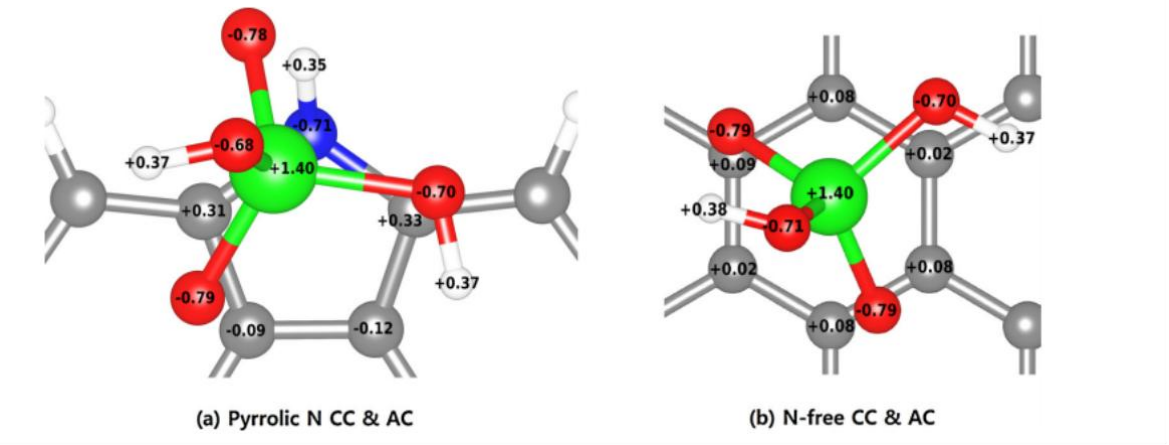


Figure 34. Two optimized structures of AC on Pyrrolic N CC (a) and N-free CC (b) (water molecules are not shown here). Carbon, hydrogen, nitrogen, oxygen and arsenic atom are represented by gray, white, blue, red and green balls, respectively.

## 3.2.4. Conclusions

Chlorination at 700℃ (denoted as CN700) leads to porous carbon with micropore of 0.7 nm and mesopore in the range of 1~3 nm. With increasing chlorination temperature, pores are broaden into the large mesopores. Interestingly, by decomposition of $CN_x$, active nitrogen, such as pyrrolic and pyridonic-N, were doped uniformly into carbon lattice. CN700 shows the highest maximum adsorption capacity of 31.08 mg/g. This remarkable removal capacity is mainly attributed to pyrrolic-N, which imparts positive charges to adjacent carbon atoms and hydrogen atom, binding arsenic complex, $H_2AsO_4^{-1}$, through electrostatic interaction. In addition, well developed micro-pores and small meso-pores were acted as an active site for arsenic adsorption and a booster respectively for rapid diffusion of arsenic complex in water, due to the unique conformal reaction of chlorination. Important finding is as follows; step edge of particles were acted as nucleation sites for graphite layers and this layers grew along the ledge surface. At a low temperature of 300 degree, this graphite nucleation was presumably attributed by step edge and nitrogen decomposition.

## 3.3. Hybrid graphene/porous carbon

### 3.3.1. General note

- CN — Reaction of $Ti(C_{0.7}N_{0.3})$ with $Cl_2$ gas at 800°C And with $H_2$ at 600 °C for 2h
- aCN-KOH — Reaction of CN with KOH (1/4 weight ratio) at 800°C for 1h under $N_2$
- aCN-KOH/KCl — Reaction of CN with KOH and KCl (1/4/3 weight ratio) at 800°C for 1h under $N_2$
- CN-KOH-KCl — Reaction of aCN with KCl (1/3 weight ratio) at 800°C for 1h under $N_2$
- CN-KCl — Reaction of CN with KCl (1/3 weight ratio) at 800°C for 1h under $N_2$
- AC-KOH/KCl — Reaction of AC with KOH/KCl (1/4/3 weight ratio) at 800°C for 1h under $N_2$

### 3.3.2. Motivation

Because graphite has a layered structure, alkali metals readily penetrate and interact with the layers to form compounds. Based on this fact, a carbon nanoscroll can be synthesized. Graphite-intercalation compounds are exfoliated by reacting with aqueous solution and this exfoliated graphite is readily scrolled by mechanical stimuli, thus making carbon nanoscroll.

Potassium metal is generated as an intermediate phase above 562 ℃ during KOH activation. Most of the papers explained that potassium metal penetrated into the carbon lattice and developed additional pores. However, some reports have reported that graphite could be peeled off by forming graphite-intercalation compounds during KOH activation. On the other hand, some explained that the metal K produced during KOH activation could only penetrate crystalline graphite not disordered carbon and make graphite-intercalation compounds.

These facts motivated us to develop the hybrid graphene/porous carbon. In order to peel off the graphite layers and activate pore structure of carbon, we activated CN materials, introduced in chapter 3.2., that had graphite layers developed on the disordered carbon. From KOH activation of CN few graphene layers were developed while disordered carbon were highly activated. Further, using molten salt, which were expected to be acted as a template for two-dimensional materials, exfoliated graphite were developed laterally making hybrid graphene/porous carbon material.

### 3.3.3. Results of hybrid graphene/porous carbon

The reaction of titanium carbonitride with $Cl_2$ gas at high temperature resulted in the formation of nitrogen doped carbon (CN) materials. Since chlorination of carbide accompany the conformal transformation when titanium is removed as a $TiCl_4$, hierarchical porous carbon with micro- and mesopore could be obtained by further decomposition of C-N bonds. The reaction with $Cl_2$ gas is discussed in the experimental section. Field Emission Scanning Electron Microscopy (FESEM) image of CN (figure 35a) showed that the particle surfaces were flat and stepped, and this was attributed from graphite edge planes. In warner's study [98] it was demonstrated that graphene edge planes were observed as a terraced graphene domain, which was verified by atomic force microscopy (AFM). In order to observe microstructure of CN, TEM analysis was conducted (figure 36a). It demonstrated that the inner part of particles consist of disordered carbon and the surface part had stacked layers of graphite with thickness in the range of 2.5 ~ 3.5 nm, which consisted of 7~10 layers of graphite, based on interlayer spacing of 3.34 Å. X-ray diffraction (XRD) results (figure 37a) show broad (002) and (10) peaks representing typical disordered carbon materials and diffraction peaks at 26.7° of 2 theta corresponding to graphite layers with interlayer spacing of 3.34 Å. The SEM, TEM, and XRD results indicate that layers of graphite and disordered carbon are integrated into one structure.

After KOH activation of CN, stacked layers of graphite were exfoliated, and disordered carbon inside of particle was activated. We denote the activated CN as aCN-KOH. From the SEM image (figure 35b), it showed that few-layered graphite were developed on the surface of the particle while the morphology of the particles in aCN-KOH was not changed by

activation. The flat, stepped surface of the CN consisting of stacked layers of graphite was transformed into a porous structure of graphite with few-layer, such as unwound yarn. Such a structure observed from the SEM image were analogous to that of nano-architectured graphene/CNT@porous carbon in which a disordered carbon was coated with SWNT and graphene. The hybrid material was used as electrodes for Lithium-sulfur batteries and showed excellent performance because of its seamlessly interconnected structure of crystalline graphene and CNT with a disordered were interlinked with and spread over the disordered carbon. TEM analysis (figure 36b) of aCN-KOH were conducted to further analyze its microstructure after KOH activation. When KOH reacts with disordered carbon, defects and edges of the graphite layer, disordered carbon inside of CN is dominantly activated by oxidation as a form of $K_2CO_3$, which is evidenced by the loose microstructure as shown in figure 36b. Through the TEM, few-layered graphite was observed and it existed as a wavy and crumpled shape, with folding occurred at the edge of layer. This folding is usually observed in single/several layers of graphene. As shown in figure 36b, a dark area where few-layered graphite was severely overlapped was observed as wrinkles. We think that this wrinkle can be caused by damage to the defective part of the graphite layer by KOH attack. During the KOH activation of CN, etching of disordered carbon occurred leading to activated porous structure, and simultaneously stacked graphite layers were exfoliated by potassium metal produced during KOH activation and reconstructed spreading over the particles.

The fact that stacked layers were exfoliated into few-layered graphite motivated us to seek the method to develop two dimensional graphene. Normally KCl has been known for an inert salt melt; it allows faster mass transfer transport in liquid phase. By using the salt metal, glucose was converted to graphene and two dimensional metal oxide were successfully

synthesized. It has been found that molten salt acted as template for two-dimensional material such as transition metal oxide and graphene. In this work, we used KCl as a template to develop few-layered graphite into 2D graphene. According to SEM images (figure 36c), the in-situ activated powder (denoted here as aCN-KOH/KCl) showed that it had a similar form to aCN-KOH and also has a very porous graphite structure with few-layer. TEM image of figure 36c confirmed that the porous graphite structure was a 2D developed graphene and showed that the 2D graphene was interconnected to the porous surface. As can be seen from the SEM image (figure 35c), 2D graphene exists in several directions in one porous particle, which is about 100 nm in the lateral direction. This seamlessly developed 2D graphene was further confirmed by HRTEM images. As shown in figure 38, it showed two folded graphene layers with intact crystallinity while the inside of the particle was amorphous evidenced by Fast Fourier Transform (FFT). We also observed the atomic structures of defective graphene. It consists usually of 1~3 atomic layers and has nanopores in damaged graphene plane. In the field of electrochemistry, this damaged graphene with crystalline CNT as a hybrid composite acted as active sites for oxygen reduction reaction and showed excellent performance. The layers of graphite in the carbon play an important role in developing graphene. We, therefore, studied two control experiments: activating commercial activated carbon having an amorphous structure using KOH and KCl and reacting aCN-KOH with KCl in the same weight ratio as aCN-KOH/KCl which we called aCN-KOH-KCl. The reaction of KOH and KOH/KCl activated AC resulting in porous carbon with the high surface area but not made AC into the graphene-like material. This demonstrates that graphene is only developed from graphite layers, not amorphous carbon. In case of aCN-KOH-KCl graphene is developed into more laterally about 200~300 nm as shown in TEM. The FESEM image clearly showed that the lateral graphene developed on the porous particle surface and the layers were more

aligned than the aCN-KOH/KCl surface structure. However, KCl itself does not exfoliate the stacked graphite layer after reaction with CN and does not develop it into graphene. Through the TEM images, compared to aCN-KOH/KCl, more lateral development and enhanced crystallinity in aCN-KOH-KCl mean that KCl acted as a template only if exfoliated layers are existed. As TEM shown, 3~5 layers were overlapped at the edges. To study the mechanism of template effect we reacted aCN-KOH with KCl at low temperature of 600 ℃ in which KCl existed as solid form. And we increased the duration time at 800 ℃ and the KCl ratio to the aCN-KOH to investigate the potential lateral growth and enhanced crystallinity.

Raman spectroscopy as shown in figure 39 was conducted to investigate the structural features of CN, aCN-KOH, aCN-KOH/KCl, and aCN-KOH-KCl. CN exhibits two broad D band around 1350 $cm^{-1}$ and G band around 1574 $cm^{-1}$. The D band is caused by the disordered structure of the graphene, the G band is due to the binding stretching of the $sp^2$-hybridized carbon, and both represent the disordered carbon of CN. In broad D+G band a decrease in the full width at half maximum intensity (FWHM) of aCN-KOH is observed because the disordered carbon is more selectively removed than the stacked graphite layers as the carbon is oxidized by KOH. This indicate s that C-C bonding becomes more uniform and by evolution of graphene, 2D band arises The width of D and G bands get sharper with 2D band at 2780 $cm^{-1}$ and broad D+G band at around 2900 $cm^{-1}$, all of which imply the porous graphitic carbon. G band in aCN-KOH, which is activated by $sp^2$-carbon domain, become intensified and narrowed after chemical activation, which was attributed to retained crystallinity in graphitic layers and also etching of the disordered carbon. This is more narrowed in aCN-KOH/KCl, which is ascribed to an increased crystalline degree of graphene possibly by KCl as a template. This is consistent with the enhanced crystallinity of aCN-

KOH/KCl compared to aCN-KOH. These results (Raman and XRD) are also consistent with the result of higher C/O ratio of aCN-KOH/KCl (59.53) than that of aCN-KOH (35.01) calculated by elemental analysis, both of which are higher than that of activated graphene-related materials (24.58 for 3D hierarchical porous graphene and ~35 for activated graphene material). The high C/O ratio normally results in good electrical conductivity and chemical stability. Therefore, keeping high C/O ratio in carbon materials could be an important factor for electrochemical application. 2D band at around 2680 $cm^{-1}$ is more enhanced in aCN-KOH and aCN-KOH/KCl with decreasing D+G band, implying that reconstructed few-layers of graphite and few-layered graphene-like structures were developed. Electrical conductivity (fig. 40), measured by four-probe method, increased from 3.2 * $10^2$ S/m (CN) to 1.3 * $10^3$ S/m (aCN-KOH). The increase in conductivity was likely attributed to crystalline few-layers of graphite, and dominant removal of the disordered carbon by etching. Further increase of electrical conductivity in aCN-KOH/KCl, determined to be 2.4 * $10^3$ S/m, was mainly due to developed crystalline 2D graphene from the few-layers of graphite. This value is about fifty times higher than that of activated graphene material and, to our best knowledge, it is so far the highest value reported for porous graphene-related materials. The properties of the excellent electrical conductivity and high density of micropores in aCN-KOH and aCN-KOH/KCl which is evidenced by the steep increase in a low-angle scatter from XRD (fig. 37), may find potential application where high surface area and electrical conductivity are needed.

The porosity of activated samples was characterized by cryogenic nitrogen sorption experiments and the isotherms are shown in figure 41. The $N_2$ sorption of chemically activated aCN-KOH and aCN-KOH/KCl showed Type I and IV adsorption isotherms with hysteresis, indicating the characteristics of well-developed porous carbon with micropore and

mesopore. aCN-KOH and aCN-KOH/KCl exhibit high adsorption curves at low and intermediate relative pressures, indicating that micropore and mesopore are well developed by KOH activation. The slightly higher adsorption amount of aCN-KOH/KCl at relative pressure ($0.05 < P/P_0 < 0.45$) is considered to be the pore developed by the 2D graphene, as can be seen from the TEM results. In the case of CN-KCl, adsorption curves and adsorption amounts similar to CN are shown, indicating that KCl does not react chemically with carbon and does not activate the pore structure of carbon. The adsorption amount of aCN-KOH-KCl is lower than that of aCN-KOH and aCN-KOH/KCl at low and intermediate relative pressures. The adsorption amount of aCN-KOH-KCl prepared by ex situ activation method is lower than that of aCN-KOH and aCN-KOH/KCl at low and intermediate relative pressures. This is because the crystallinity of the 2D graphene produced by the ex situ method is improved more than when it is made in situ, which is why the micropore and mesopore are less developed. The pore properties of all samples are summarized in table s1. The Brunauer-Emmett-Teller (BET) specific surface area of CN was 1572 $m^2/g$ and, after activation it increased to 3518 $m^2/g$ for aCN-KOH and 3779 $m^2/g$ for aCN-KOH/KCl, all of which were more than twice that of CN, indicating that KOH activation developed the micropore and small mesopore which mainly affected the BET specific surface area. The pore volumes of aCN-KOH/KCl and aCN-KOH were 2.70 and 2.64 $cm^3/g$ which are more than double that of CN (1.11$cm^3/g$). The calculation of MP method indicates that aCN-KOH/KCl has slightly narrowed and well developed micro pore of 1~1.6 nm compared to CN and micro pores were shifted into smaller size region compared to aCN-KOH. From Barrett-Joyner-Halenda (BJH) method, CN had mesopore feature in 2~10 nm region which, however, was highly activated in aCN-KOH and aCN-KOH/KCl with uniform pore size distributions. More developed mesopore in 2~3 nm range could be possibly from development of mesopore in 2D graphene

shown in TEM images. The higher BET SSA and mesopore developed in 2D graphene in aCN-KOH/KCl thus indicate that KOH activation favorably etched disordered carbon and also damaged the graphene with defects which develops the mesopore.

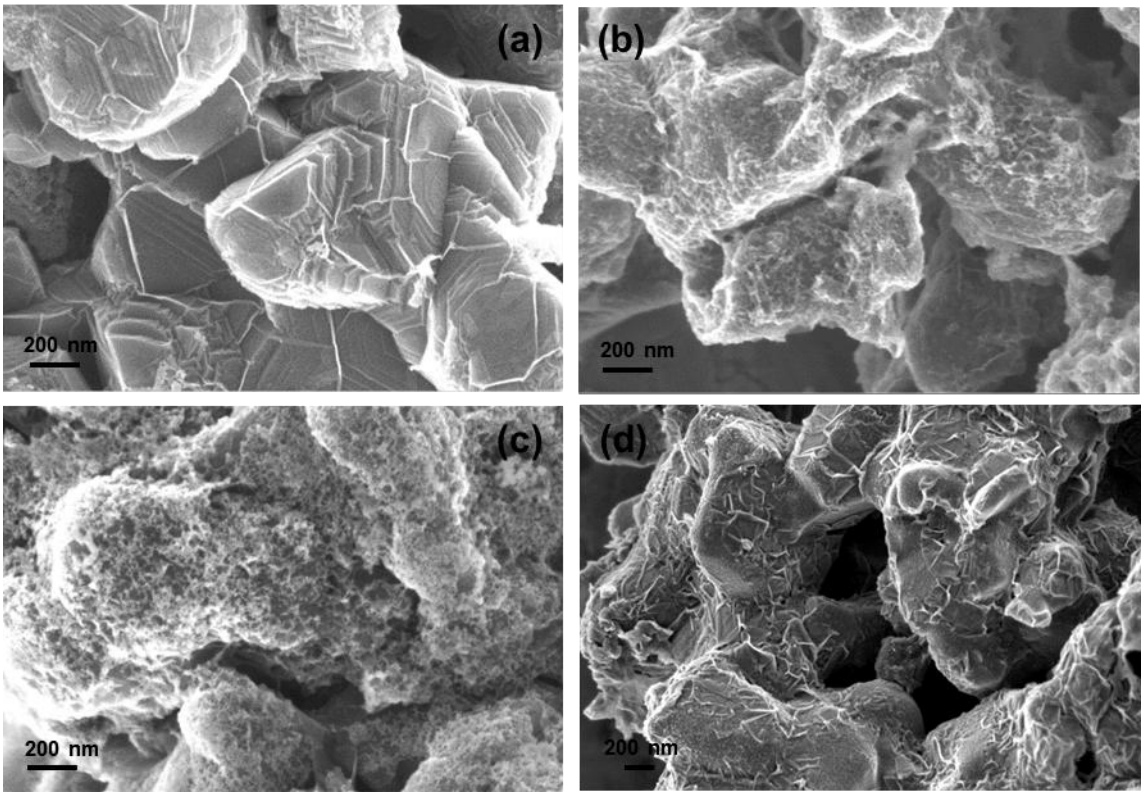


Figure 35. Field Emission Scanning Electron Microscopy (FESEM) images of CN (a), aCN-KOH (b), aCN-KOH/KCl (c), and aCN-KOH-KCl (d).

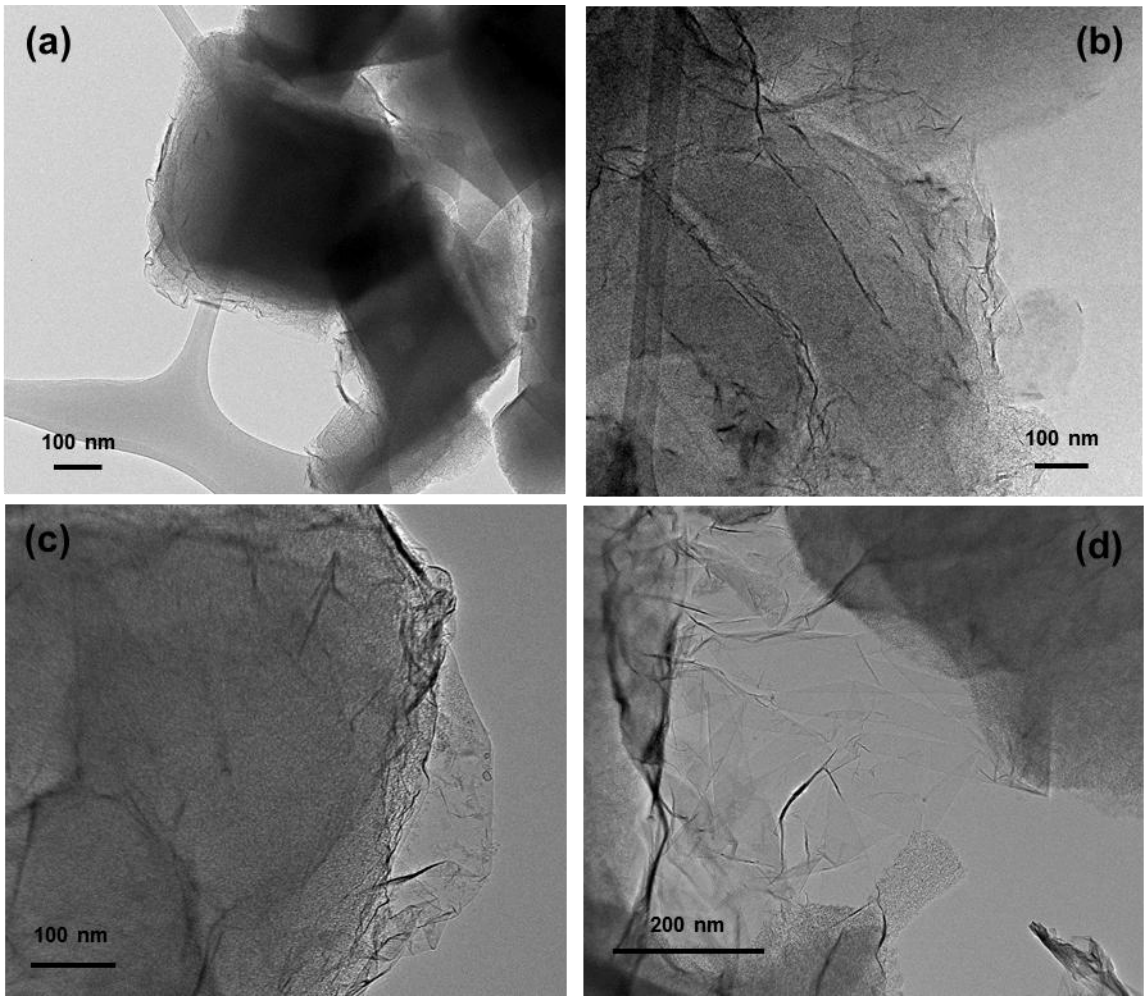


Figure 36. Transmission Electron Microscopy (TEM) images of CN (a), aCN-KOH (b), aCN-KOH/KCl (c), and aCN-KOH-KCl (d).

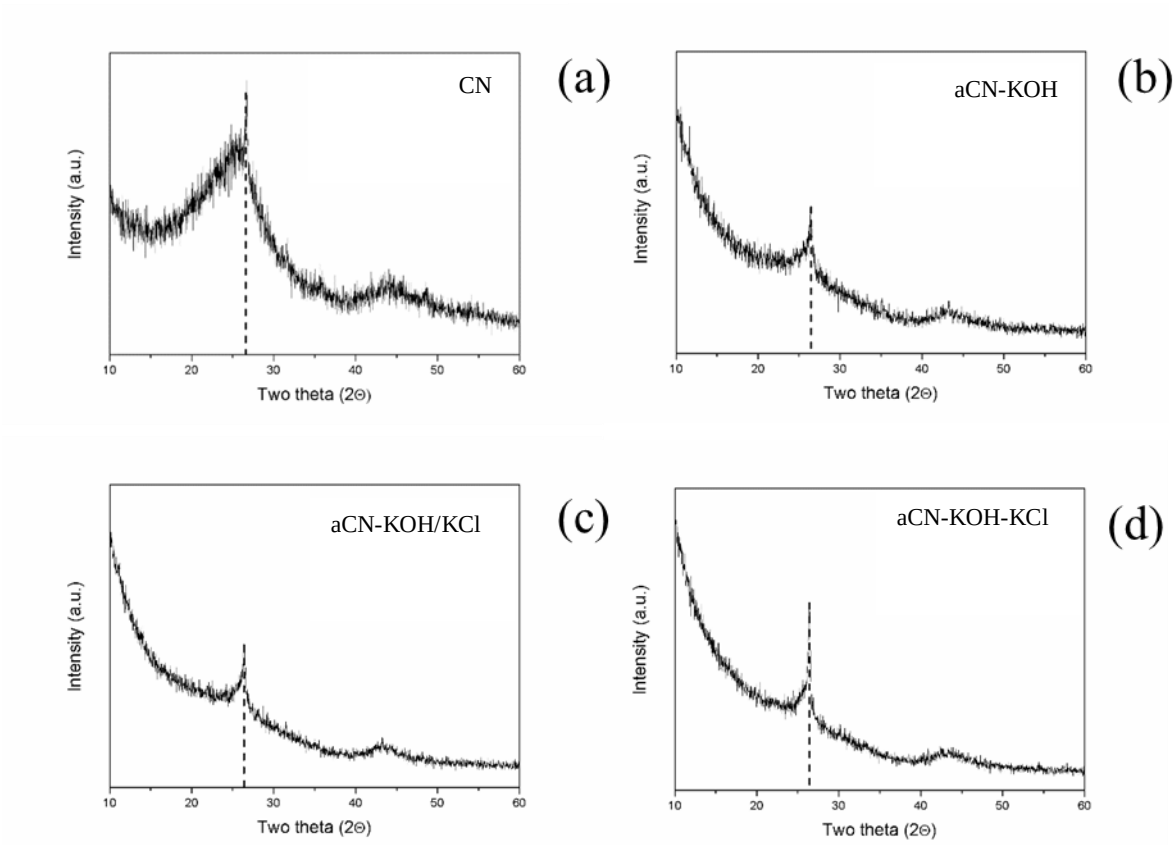


Figure 37. X-ray diffraction results of CN (a), aCN-KOH (b), aCN-KOH/KCl (c), and aCN-KOH-KCl (d).

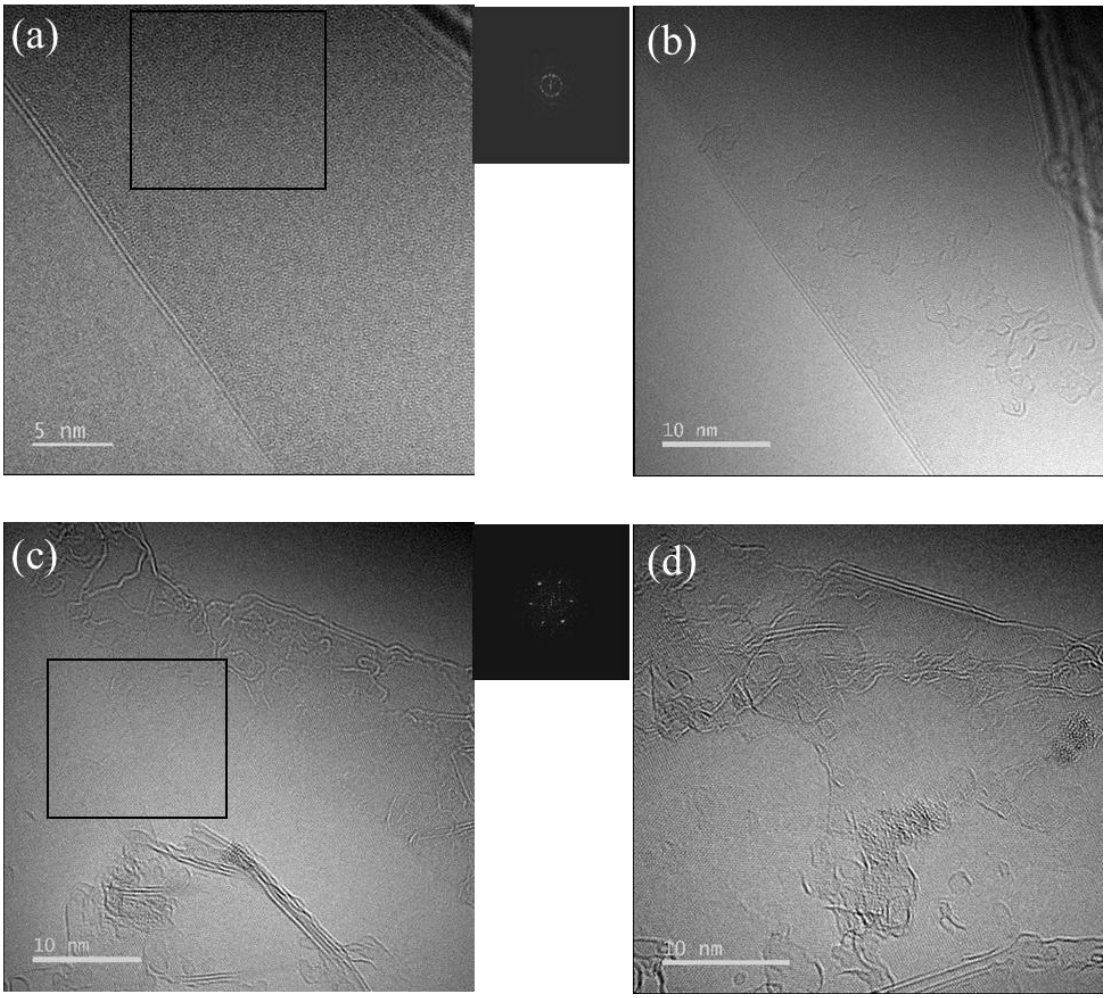


Figure 38. Transmission Electron Microscopy (TEM) images of aCN-KOH/KCl (a,b,c,d). Inset shows the Fast Fourier Transform (FFT) images for a and b.

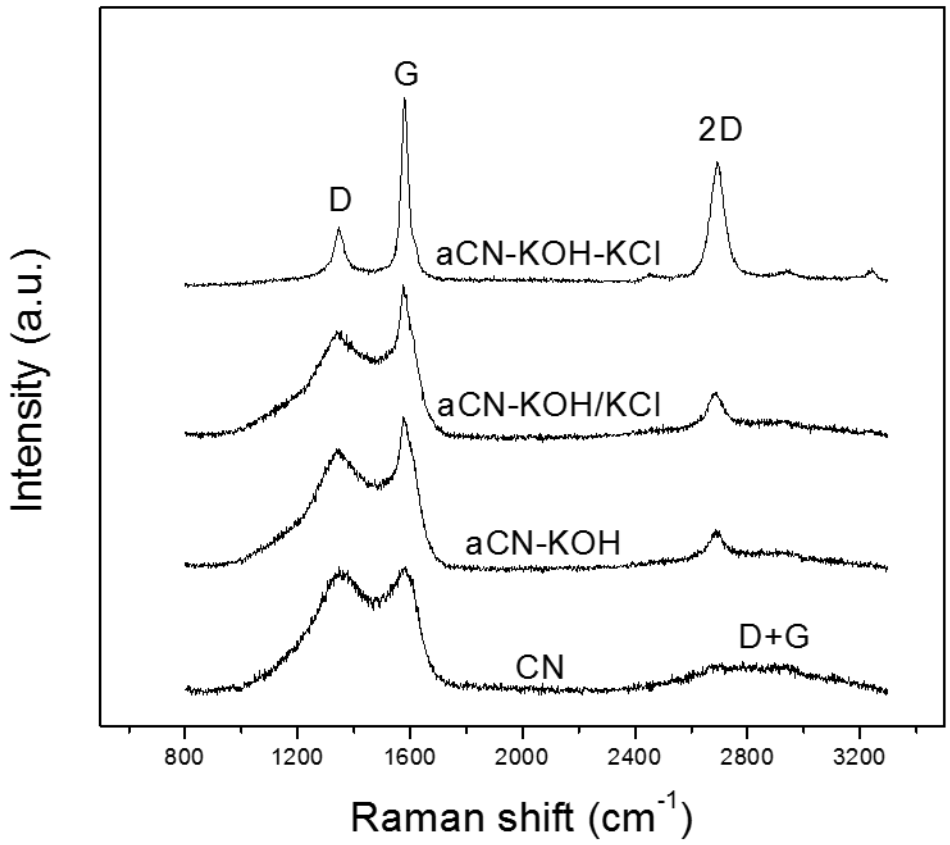


Figure 39. Raman spectra of CN, aCN-KOH, aCN-KOH/KCl, and aCN-KOH-KCl.

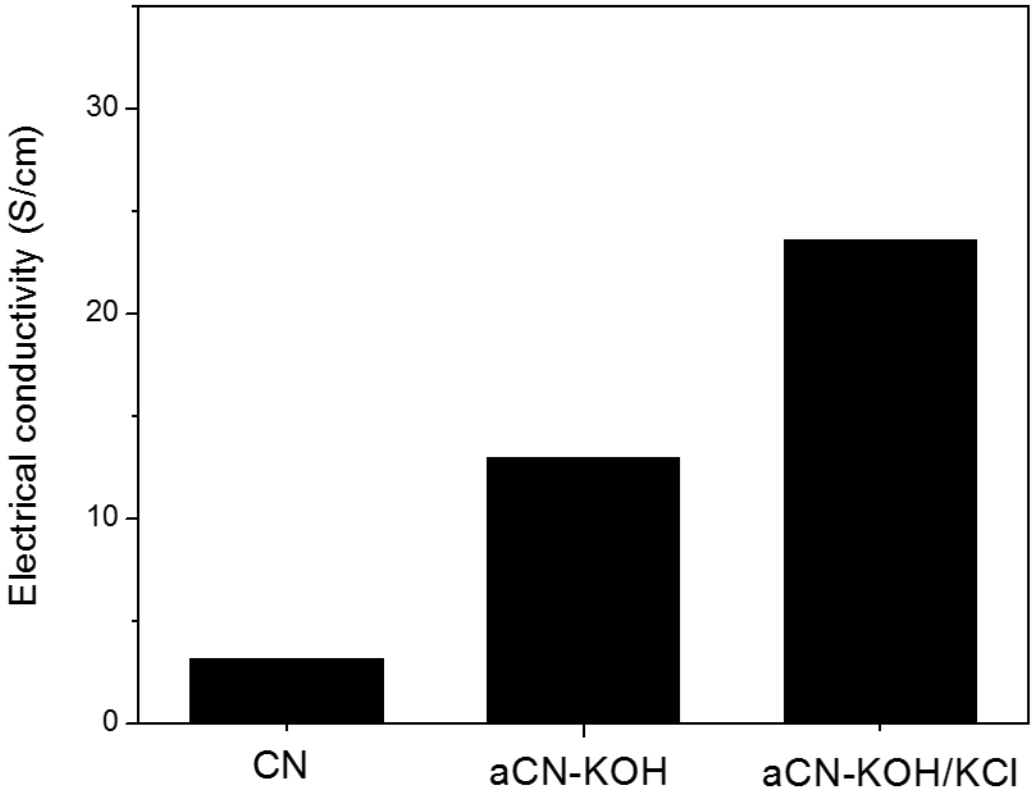


Figure 40. Electrical conductivity (S/cm) of CN, aCN-KOH, and aCN-KOH/KCl measured by four-point method.

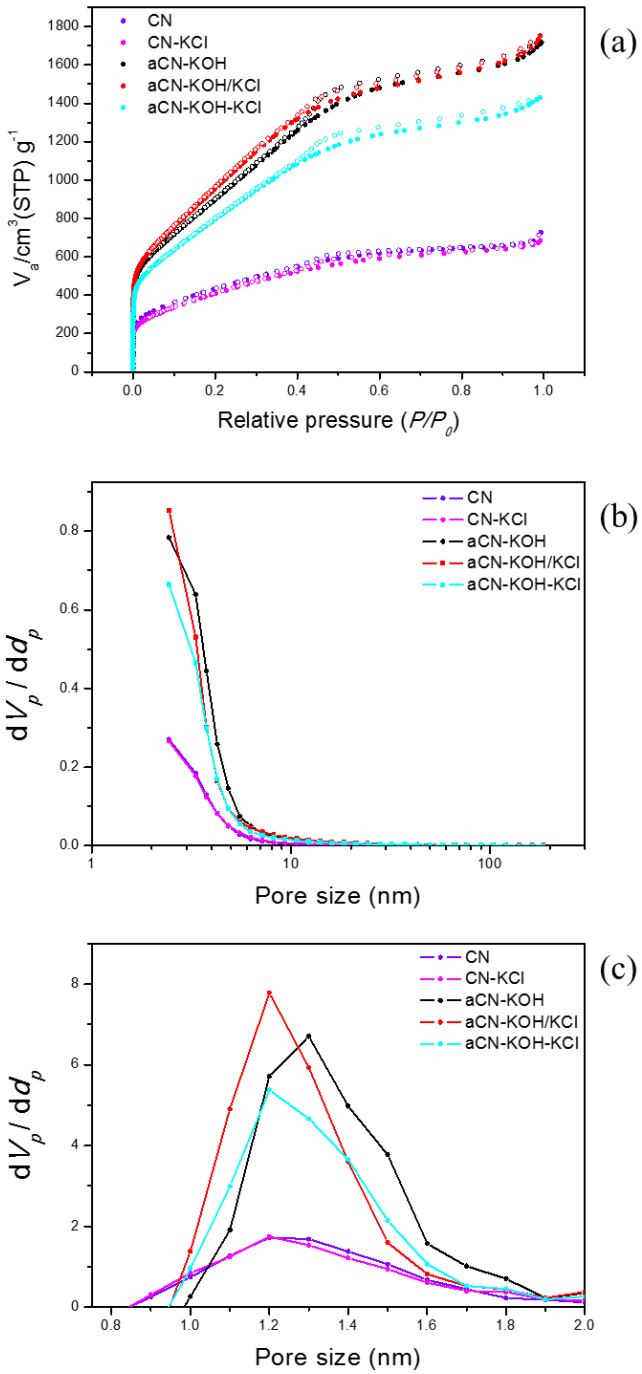


Figure 41. Nitrogen sorption isotherms at 77 K (a), mesopores calculated by BJH method (b), and micropores calculated by MP method (c) of CN, CN-KCl, aCN-KOH, aCN-KOH/KCl, and aCN-KOH/KCl.

| | SSA ($m^2/g$) | Total pore volume ($cm^3/g$) | Micro pore volume ($cm^3/g$) | Meso pore volume ($cm^3/g$) | Mean pore diameter (nm) |
|---|---|---|---|---|---|
| CN | 1572 | 1.11 | 0.56 | 0.47 | 2.83 |
| CN-KCl | 1486 | 1.05 | 0.52 | 1.01 | 2.91 |
| aCN-KOH | 3518 | 2.64 | 1.11 | 1.43 | 3.01 |
| aCN-KOH/KCl | 3779 | 2.70 | 1.16 | 1.40 | 2.86 |
| aCN-KOH-KCl | 3040 | 2.21 | 0.98 | 1.15 | 2.91 |

Table 6. Texture properties of synthesized materials measured by Nitrogen sorption isotherms at 77 K.

Specific surface area (SSA) was derived by BET equation. The total pore volume was measured up to $P/P_0$ =0.99. Micro and mesopore volumes were measured up $P/P_0$ =0.1 and 0.1< $P/P_0$ <0.95.

| | C (wt.%) | N (wt.%) | H (wt.%) | O (wt.%) | C/O ratio |
|---|---|---|---|---|---|
| CN | 70.23 | 13.43 | 1.64 | 6.14 | 11.44 |
| CN-KCl | 74.56 | 9.97 | 1.62 | 10.89 | 6.85 |
| aCN-KOH | 91.83 | 0.32 | 0.15 | 2.77 | 33.15 |
| aCN-KOH/KCl | 92.6 | 0.12 | 0.18 | 1.55 | 59.74 |
| aCN-KOH-KCl | 90.72 | 0.15 | 0.17 | 1.24 | 73.16 |

Table 7. Chemical composition of synthesized material measured by elemental analysis (EA)

### 3.3.4. Applicability of hybrid graphene/porous carbon for capacitive deionization

Figure 42 presents the electrochemical performance of CN, aCN-KOH, and aCN-KOH/KCl electrodes, which provides their specific capacitance conducted by the galvanocharge/discharge (Figure 42a) and the CV (Figure 42b). Figure 42a shows the specific capacitance of the electrodes at current densities varying from 0.1 A $g^{-1}$ to 10 A $g^{-1}$ in a 1 M of NaCl aqueous solution within the cell voltage range of 0 V to 1.2 V of which theoretically electrolysis can be prevented. Note that the specific capacitance of each electrode was calculated as how much charges per one gram of electrode are accumulated by electrical energy of one volt. First of all, the specific capacitances of the aCN-KOH/KCl and the aCN-KOH electrodes were higher than that of the CN electrode, resulting from the hierarchical pore structure, specific surface area and their porous graphitic carbon activated by KOH. For instance, at a current density of 0.1 A $g^{-1}$, the specific capacitance of 177 F $g^{-1}$ and 142 F $g^{-1}$ were measured in the aCN-KOH/KCl and the aCN-KOH electrodes, respectively, while that in the CN electrode was 55 F $g^{-1}$. Next, as the current density increases, the superior kinetic performance was observed in the aCN-KOH/KCl electrode, which the specific capacitance of approximately 31% was retained at one hundred times higher current density compared to that at a current density of 0.1 A $g^{-1}$. Whereas the retention of specific capacitance was approximately 18% and 7% in the aCN-KOH and CN electrodes, respectively. This excellent rate capability of the aCN-KOH/KCl electrode is attributed to high electrical conductivity originated from crystallinity in graphitic layers. It contributes to rapid adsorption and desorption of ions on the electrode surface even at the condition of high current density. This tendency of the specific capacitance in the CN, aCN-KOH, and aCN-KOH/KCl electrodes is

corresponded to that in CV measurement (Figure 42b). From the rectangular shape in the CV measurement, it is confirmed that these three electrodes possess super-capacitive properties for ion adsorption and desorption. Moreover, the rectangular shape of the aCN-KOH/KCl electrode was comparably not declined in comparison with those of the CN and aCN-KOH electrodes at the high scan rate, supporting that the excellent rate capability of the aCN-KOH/KCl electrode. As shown in Figure 42c, in aCN-KOH/KCl electrode, total resistance of the cell including the electrode and electrolyte that can be estimated by the intercept of x-axis in Nyquist plot was lower compared to that in aCN-KOH electrode. Moreover, the lower diffusion resistance of aCN-KOH/KCl electrode was measured in Nyquist plot (lower slope to 45 degree), contributing to better ion accessibility to the electrode surface.

The deionization performance of CN, aCN, and aCN-Gra electrodes was demonstrated in 10 mM of NaCl aqueous solution through single pass CDI operation and the result of deionization performance was shown in Figure 42d. Note that the salt adsorption capacity (SAC) is a representative factor to present how much ions (salts) can be deionized per one gram of employed electrodes. As shown in Figure 42d, the superior deionization capacity was measured in aCN-Gra electrodes, which was the SAC of approximately 22 mg $g^{-1}$, and the SAC of aCN and CN were 18 mg $g^{-1}$ and 10 mg $g^{-1}$, respectively. The deionization capacities of aCN-Gra and aCN electrodes are higher than that of the MSP20 electrode that is one of the widely used commercial activated carbon electrode (reported SAC value in literature: 13.5 mg $g^{-1}$) resulting from their high specific surface area. On the other hand, in respect to the kinetic performance in SAC curves, the rapid ion adsorption was observed in aCN-Gra electrode within approximately 6 min (with higher SAC) compared to that in aCN electrode (approximately 8 min). It could be originated from the crystallinity in graphitic

layers in aCN-Gra electrode.

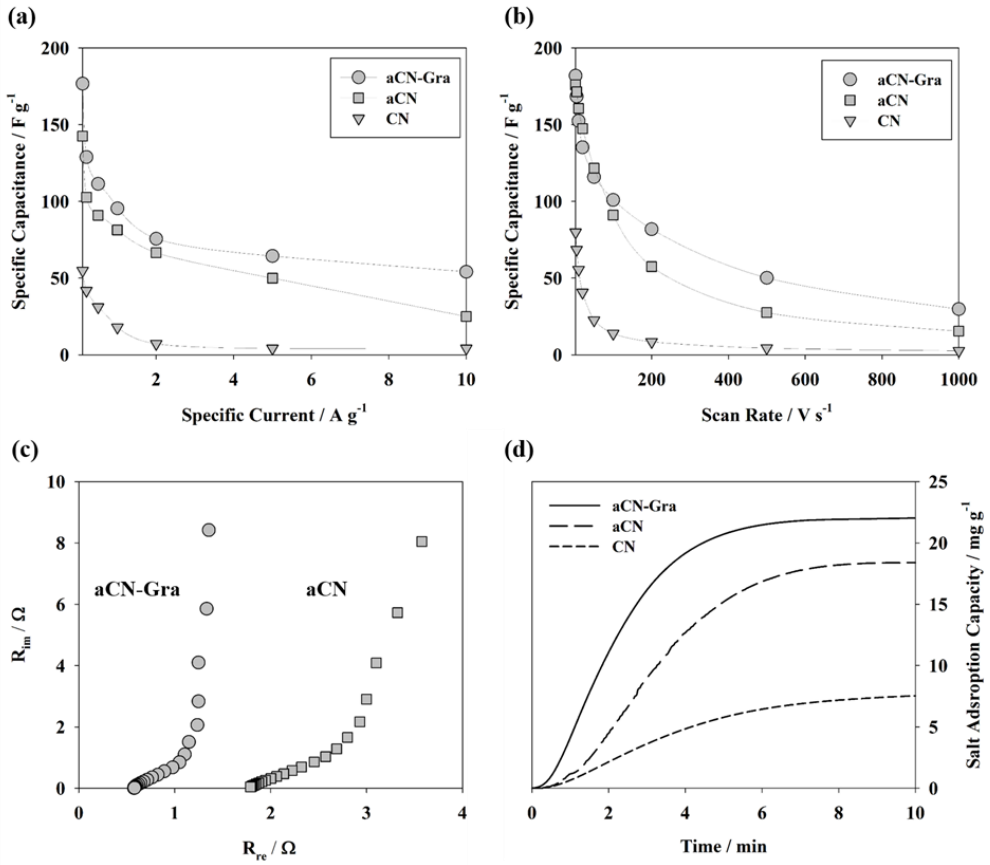


Figure 42. The specific capacitance of the CN, aCN-KOH, aCN-KOH/KCl electrodes evaluated through (a) galvanocharging/discharging and (b) CV, (c) the Nyquist plot of aCN and aCN-Gra electrodes in 1 M of NaCl aqueous solution and (d) the salt adsorption capacity of CN, aCN-KOH, aCN-KOH/KCl electrodes in 10 mM of NaCl aqueous solution.

## 3.3.5. Conclusions

Herein, we reported the simple and effective route to synthesis of hybrid material of nano-architectured graphene/porous carbon. This hybrid carbon showed a well-developed pore structure with a very high electrical conductivity of 2200 S/m, a high BET SSA of 3779 $m^2/g$ and a pore volume of 2.70 $cm^3/g$. The key to hybrid carbon synthesis is the use of KOH and KCl to activate the carbon (denoted as CN) that had graphite layers developed on the disordered carbon. Since graphite is layered structure it can be intercalated by alkali metals. Beguin et al. suggested through the XRD results of the intercalation compound phase that the metal K produced during KOH activation could be inserted into regular ordered graphite layers but not into disordered graphite layers. According to Kaner's study, graphite intercalated compound could be readily exfoliated by reacting it with aqueous solutions and reconstructed by mechanical stimulation. In this study, we found that during the KOH activation of carbon, the graphite layer was intercalated by metallic K and reconstituted by the washing step into few layers of graphite while the disordered carbon was predominantly activated. Surprisingly, by activating CN with KOH and KCl, a few layers of graphite developed into two-dimensional (2D) graphene, where KCl acts as a template for lateral growth. As a result, the developed graphene has a structure that is gently connected to porous carbon. The mechanism of development of 2D graphene is discussed in detail in this work. This promising hybrid material was used as electrode materials for capacitive deionization (CDI) which is attracting great attention as a novel desalination technology. Due to well-developed pore structure and conductive graphene interface, high Na+ and Cl- ions sorption rate and capacity were achieved.

# 4. Overall conclusions

The novel synthesis methods for porous carbon material with hierarchic pore structure has been demonstrated. Most studies of this dissertation have exploited the advantages of conformal transformation of the CDC process. From this astonishing characteristic, various results have been explored and new finding was found, in this dissertation. By introducing the pores and nitrogen substitution in the carbide, hierarchic CDCs with mesopore were successfully synthesized. We have found scientific results in CDC process. The introduction of the surface step edge of the carbonitride nucleated graphite layers on the surface. This graphite was exfoliated by KOH activation and formed into few-layered graphene. Ultimately, the graphene was developed laterally using molten salt, and the graphene associated with the porous carbon gave rise to a new hybrid material with one structure.

First, mesoporous titanium carbide was synthesized by carbothermal reduction of $ZnTiO_3$ with graphite under argon atmosphere. This process resulted in mesoporous titanium carbide, because metallic Zn is vaporized with fast rate at high temperature making the holes of 2~80 nm in the TiC particles. Chlorination of porous TiC led to synthesis of carbon with hierarchical pore structure where the holes acted as pore channels to micropore. This method could apply to other porous carbides (TiC, MoC, ZrC, SiC, etc.) and make hierarchical porous carbon materials with different specific pore size.

Second, titanium carbonitride, $Ti(C_xN_{1-x})$ was obtained by carbothermal reduction of $TiO_2$ with graphite under $N_2$ atmosphere. The composition of nitrogen in $Ti(C_xN_{1-x})$ could be tuned by molar ratio of $TiO_2$ and graphite, and synthesis temperature. Through the chlorination, the porosity changed depending on the composition of C and N in $Ti(C_xN_{1-x})$

and chlorination temperature. Since chlorine react with Ti($C_xN_{1-x}$) layer by layer, as formed $TiCl_4$ is vaporized carbon remained as the forms of C-C and C-N bonds. However, because of unstable C-N bonds at high temperature, decomposition occurred as a form of $CN_x$ and $N_2$, which resulted in additional pore generation from meso- to macropore depending on the nitrogen contents in Ti($C_xN_{1-x}$). As nitrogen content increases remaining carbon was gasified with increasing temperature due to severe decomposition of C-N bonds which results in collapse of microporous structure, and hence meso- and macropore were developed without micropore. Therefore, in this dissertation, Ti($C_{0.7}N_{0.3}$) was chosen for synthesizing the porous carbon with uniform pore structure. Chlorination at 700℃ (denoted as CN700) leads to porous carbon with micropore of 0.7 nm and mesopore in the range of 1~3 nm. With increasing chlorination temperature, pores are broaden into the large mesopores. Interestingly, by decomposition of $CN_x$, active nitrogen, such as pyrrolic and pyridonic-N, were doped uniformly into carbon. This materials was applied to adsorbent for arsenic removal in water. The detailed mechanism of arsenic adsorption was discussed. Also, we found that step edge on the titanium carbonitride promoted the graphitization on the surface. It seemed that edges with many broken bonds nucleated graphene after etching the titanium and the graphene grew along the (111) plane. With this mechanism, we could control the thickness of graphite layer and lateral size.

Lastly, Novel method to develop graphene from graphite layers is introduced. The graphite layers were grown on the carbon surface synthesized by chlorination of Ti($C_{0.7}N_{0.3}$). The graphite layer can be intercalated by metal potassium (K) to form graphite-intercalation compounds and can be peeled off into several layers by mechanical stimulation. The metal K formed by KOH activation is intercalated into the graphite layers of CN700, and the

disordered carbon inside is activated through the oxidation reaction to activate the pore structure. In addition, this peeled graphite layers were developed into a two-dimensional graphene composed of one to three layers through simultaneous activation reaction with a molten salt (KCl). Due to the activation process and development into two-dimensional graphene, the hybrid graphene/porous carbon material has a very high electrical conductivity of 2200 S/m, high specific surface area of 3779 $m^2/g$, and high pore volume of 2.70 $cm^3/g$.

# Reference

[1] Sing, Kenneth SW. "Reporting physisorption data for gas/solid systems with special reference to the determination of surface area and porosity (Recommendations 1984)." *Pure and applied chemistry* 57.4 (1985): 603-619

[2] Lee, Jinwoo, Jaeyun Kim, and Taeghwan Hyeon. "Recent progress in the synthesis of porous carbon materials." *Advanced Materials* 18.16 (2006): 2073-2094.

[3] Liang, Chengdu, et al. "Synthesis of a Large-Scale Highly Ordered Porous Carbon Film by Self-Assembly of Block Copolymers." *Angewandte Chemie International Edition* 43.43 (2004): 5785-5789.

[4] Panella, Barbara, Michael Hirscher, and Siegmar Roth. "Hydrogen adsorption in different carbon nanostructures." *Carbon* 43.10 (2005): 2209-2214.

[5] Oren, Yoram. "Capacitive deionization (CDI) for desalination and water treatment—past, present and future (a review)." *Desalination* 228.1-3 (2008): 10-29.

[6] Yu, Jong-Sung, et al. "Fabrication of ordered uniform porous carbon networks and their application to a catalyst supporter." *Journal of the American Chemical Society* 124.32 (2002): 9382-9383.

[7] Chmiola, John, et al. "Anomalous increase in carbon capacitance at pore sizes less than 1 nanometer." *Science* 313.5794 (2006): 1760-1763.

[8] Xu, Guiyin, et al. "Sulfur embedded in metal organic framework-derived hierarchically porous carbon nanoplates for high performance lithium–sulfur battery." *Journal of Materials Chemistry A* 1.14 (2013): 4490-4496.

[9] Gogotsi, Yury, et al. "Nanoporous carbide-derived carbon with tunable pore size." *Nature materials* 2.9 (2003): 591-594.

[10] Ania, Conchi O., et al. "The large electrochemical capacitance of microporous doped carbon obtained by using a zeolite template." *Advanced Functional Materials* 17.11 (2007): 1828-1836.

[11] Dash, Ranjan, et al. "Titanium carbide derived nanoporous carbon for energy-related applications." *Carbon* 44.12 (2006): 2489-2497.

[12] Presser, Volker, et al. "Effect of pore size on carbon dioxide sorption by carbide derived carbon." *Energy & Environmental Science* 4.8 (2011): 3059-3066.

[13] Oschatz, Martin, et al. "Carbide-Derived Carbon Monoliths with Hierarchical Pore Architectures." *Angewandte Chemie International Edition* 51.30 (2012): 7577-7580.

[14] Yeon, Sun-Hwa, et al. "Carbide-derived-carbons with hierarchical porosity from a

preceramic polymer." *Carbon* 48.1 (2010): 201-210.

[15] Korenblit, Yair, et al. "High-rate electrochemical capacitors based on ordered mesoporous silicon carbide-derived carbon." *Acs Nano* 4.3 (2010): 1337-1344.

[16] Lee, Jung Tae, et al. "Sulfur-Infiltrated Micro-and Mesoporous Silicon Carbide-Derived Carbon Cathode for High-Performance Lithium Sulfur Batteries." *Advanced Materials* 25.33 (2013): 4573-4579.

[17] Rose, Marcus, et al. "Hierarchical Micro-and Mesoporous Carbide-Derived Carbon as a High-Performance Electrode Material in Supercapacitors." *Small* 7.8 (2011): 1108-1117.

[18] Zhang, Jin, et al. "Carbon science in 2016: status, challenges and perspectives." *Carbon* 98.70 (2016): 8e732.

[19] Hutchins, Otis. "Method for the production of silicon tetrachlorid." U.S. Patent No. 1,271,713. 9 Jul. 1918.

[20] Gogotsi, Yury, et al. "Nanoporous carbide-derived carbon with tunable pore size." *Nature materials* 2.9 (2003): 591-594.

[21] Sigalov, Sergey, et al. "Selective adsorption of multivalent ions into TiC-derived nanoporous carbon." *Carbon* 50.10 (2012): 3957-3960.

[22] Jänes, Alar, Thomas Thomberg, and Enn Lust. "Synthesis and characterisation of nanoporous carbide-derived carbon by chlorination of vanadium carbide." *Carbon* 45.14 (2007): 2717-2722.

[23] Tallo, Indrek, et al. "Nanostructured carbide-derived carbon synthesized by chlorination of tungsten carbide." *Carbon* 49.13 (2011): 4427-4433.

[24] Cambaz, Z. G., et al. "Formation of Carbide-Derived Carbon on β-Silicon Carbide Whiskers." *Journal of the American Ceramic Society* 89.2 (2006): 509-514.

[25] Dash, R. K., G. Yushin, and Y. Gogotsi. "Synthesis, structure and porosity analysis of microporous and mesoporous carbon derived from zirconium carbide." *Microporous and Mesoporous Materials* 86.1 (2005): 50-57.

[26] Yushin, Gleb N., et al. "Synthesis of nanoporous carbide-derived carbon by chlorination of titanium silicon carbide." *Carbon* 43.10 (2005): 2075-2082.

[27] Hoffman, Elizabeth N., et al. "Synthesis of carbide-derived carbon by chlorination of Ti2AlC." *Chemistry of materials* 17.9 (2005): 2317-2322.

[28] Presser, Volker, Min Heon, and Yury Gogotsi. "Carbide-Derived Carbons–From Porous Networks to Nanotubes and Graphene." *Advanced Functional Materials* 21.5 (2011): 810-833.

[29] Dash, Ranjan, et al. "Titanium carbide derived nanoporous carbon for energy-related applications." *Carbon* 44.12 (2006): 2489-2497. Figure

[30] https://en.wikipedia.org/wiki/Carbide-derived_carbon

[31] Thomberg, Thomas, et al. "Mesoporous carbide-derived carbons prepared from different chromium carbides." *Microporous and Mesoporous Materials* 141.1 (2011): 88-93.

[32] Leis, Jaan, et al. "Carbon nanostructures produced by chlorinating aluminium carbide." *Carbon* 39.13 (2001): 2043-2048.

[33] Dimovski, Svetlana, et al. "Synthesis of graphite by chlorination of iron carbide at moderate temperatures." *Journal of Materials Chemistry* 14.2 (2004): 238-243.

[34] Robinson, Joshua, et al. "Nucleation of epitaxial graphene on SiC (0001)." *Acs Nano* 4.1 (2009): 153-158.

[35] Emtsev, Konstantin V., et al. "Towards wafer-size graphene layers by atmospheric pressure graphitization of silicon carbide." *Nature materials* 8.3 (2009): 203-207.

[36] Büke, Göknur Cambaz, et al. "Effect of defects on graphitization of SiC." *Journal of Materials Research* 28.07 (2013): 952-957.

[37] Oschatz, Martin, et al. "Hierarchical Carbide-Derived Carbon Foams with Advanced Mesostructure as a Versatile Electrochemical Energy-Storage Material." *Advanced Energy Materials* 4.2 (2014).

[38] Oschatz, Martin, et al. "Micro-and mesoporous carbide-derived carbon prepared by a sacrificial template method in high performance lithium sulfur battery cathodes." *Journal of Materials Chemistry A* 2.41 (2014): 17649-17654.

[39] Presser, Volker, et al. "Hierarchical Porous Carbide-Derived Carbons for the Removal of Cytokines from Blood Plasma." *Advanced healthcare materials* 1.6 (2012): 796-800.

[40] Smedley, P. L., and D. G. Kinniburgh. "A review of the source, behaviour and distribution of arsenic in natural waters." *Applied geochemistry* 17.5 (2002): 517-568.

[41] United States. Congress. House Committee on Science. Subcommittee on Environment Technology and Standards., Arsenic in drinking water: an update on the science, benefits, and cost: hearing before the Subcommittee on Environment, Technology, and Standards, Committee on Science, House of Representatives, One Hundred Seventh Congress, first session, October 4, 2001, U.S. G.P.O.: For sale by the Supt. of Docs., U.S. G.P.O. Congressional Sales Office, Washington, 2001.

[42] An, Byungryul, et al. "Preparation and characterization of an organic/inorganic hybrid sorbent (PLE) to enhance selectivity for As (V)." *Journal of hazardous materials* 289 (2015): 54-62.

[43] WHO Guidelines for Drinking Water Quality: Recommendations, vol. 1, W.H. Organization, Geneva (1993)

[44] Chen, Weifang, et al. "Arsenic removal by iron-modified activated carbon." *Water research* 41.9 (2007): 1851-1858.

[45] Chandra, Vimlesh, et al. "Water-dispersible magnetite-reduced graphene oxide composites for arsenic removal." *ACS nano* 4.7 (2010): 3979-3986.

[46] Mayo, J. T., et al. "The effect of nanocrystalline magnetite size on arsenic removal." *Science and Technology of Advanced Materials* 8.1-2 (2007): 71

[47] Vix-Guterl, Cathie, et al. "Electrochemical energy storage in ordered porous carbon materials." *Carbon* 43.6 (2005): 1293-1302.

[48] Sun, Yiqing, Qiong Wu, and Gaoquan Shi. "Graphene based new energy materials." *Energy & Environmental Science* 4.4 (2011): 1113-1132.

[49] Mohan, Dinesh, and Charles U. Pittman. "Arsenic removal from water/wastewater using adsorbents—a critical review." *Journal of Hazardous materials* 142.1 (2007): 1-53.

[50] Chmiola, John, et al. "Monolithic carbide-derived carbon films for micro-supercapacitors." *Science* 328.5977 (2010): 480-483.

[51] Lee, Jung Tae, et al. "Sulfur-Infiltrated Micro-and Mesoporous Silicon Carbide-Derived Carbon Cathode for High-Performance Lithium Sulfur Batteries." *Advanced Materials* 25.33 (2013): 4573-4579.

[52] Gong, Kuanping, et al. "Nitrogen-doped carbon nanotube arrays with high electrocatalytic activity for oxygen reduction." *science* 323.5915 (2009): 760-764.

[53] Hao, Guang-Ping, et al. "Rapid Synthesis of Nitrogen-Doped Porous Carbon Monolith for CO2 Capture." *Advanced Materials* 22.7 (2010): 853-857.

[54] Saada, A., et al. "Adsorption of arsenic (V) on kaolinite and on kaolinite–humic acid complexes: role of humic acid nitrogen groups." *Chemosphere* 51.8 (2003): 757-763.

[55] Yang, L., Shunnian Wu, and J. Paul Chen. "Modification of activated carbon by polyaniline for enhanced adsorption of aqueous arsenate." *Industrial & Engineering Chemistry Research* 46.7 (2007): 2133-2140.

[56] Porada, S., et al. "Review on the science and technology of water desalination by capacitive deionization." *Progress in Materials Science* 58.8 (2013): 1388-1442.

[57] Welgemoed, T. J., and C. F. Schutte. "Capacitive deionization technology™: an alternative desalination solution." *Desalination* 183.1-3 (2005): 327-340.

[58] Jeon, Sung-il, et al. "Desalination via a new membrane capacitive deionization process utilizing flow-electrodes." *Energy & Environmental Science* 6.5 (2013): 1471-1475.

[59] https://en.wikipedia.org/wiki/Capacitive_deionization

[60] Porada, S., et al. "Direct prediction of the desalination performance of porous carbon electrodes for capacitive deionization." *Energy & Environmental Science* 6.12 (2013): 3700-3712.

[61] Porada, S., et al. "Water desalination using capacitive deionization with microporous

carbon electrodes." *ACS applied materials & interfaces* 4.3 (2012): 1194-1199.

[62] Li, Lixia, et al. "Ordered mesoporous carbons synthesized by a modified sol–gel process for electrosorptive removal of sodium chloride." *Carbon* 47.3 (2009): 775-781.

[63] Zhang, Dengsong, et al. "Enhanced capacitive deionization performance of graphene/carbon nanotube composites." *Journal of Materials Chemistry* 22.29 (2012): 14696-14704.

[64] Porada, Slawomir, P. M. Biesheuvel, and Volker Presser. "Comment on sponge-templated preparation of high surface area graphene with ultrahigh capacitive deionization performance." *Advanced Functional Materials* 25.2 (2015): 179-181.

[65] Zhang, Dengsong, et al. "Enhanced capacitive deionization of graphene/mesoporous carbon composites." *Nanoscale* 4.17 (2012): 5440-5446.

[66] Dong, Qiang, et al. "Electrospun composites made of reduced graphene oxide and activated carbon nanofibers for capacitive deionization." *Electrochimica Acta* 137 (2014): 388-394.

[67] Li, Xiao, et al. "Large-Area Flexible Core–Shell Graphene/Porous Carbon Woven Fabric Films for Fiber Supercapacitor Electrodes." *Advanced Functional Materials* 23.38 (2013): 4862-4869.

[68] Liang, Ji, et al. "N-Doped Graphene Natively Grown on Hierarchical Ordered Porous Carbon for Enhanced Oxygen Reduction." *Advanced materials* 25.43 (2013): 6226-6231.

[69] Peng, Hong-Jie, et al. "Nanoarchitectured graphene/CNT@ porous carbon with extraordinary electrical conductivity and interconnected micro/mesopores for lithium-sulfur batteries." *Advanced Functional Materials* 24.19 (2014): 2772-2781.

[70] Nasibulin, Albert G., et al. "A novel hybrid carbon material." *Nature Nanotechnology* 2.3 (2007): 156-161.

[71] Raccichini, Rinaldo, et al. "The role of graphene for electrochemical energy storage." *Nature materials* 14.3 (2015): 271-279.

[72] Xu, Chaohe, et al. "Graphene-based electrodes for electrochemical energy storage." *Energy & Environmental Science* 6.5 (2013): 1388-1414.

[73] Han, Sheng, et al. "Porous graphene materials for advanced electrochemical energy storage and conversion devices." *Advanced Materials* 26.6 (2014): 849-864.

[74] Zhang, Long, et al. "Porous 3D graphene-based bulk materials with exceptional high surface area and excellent conductivity for supercapacitors." *Scientific reports* 3 (2013): 1408.

[75] Zhu, Yanwu, et al. "Carbon-based supercapacitors produced by activation of graphene." *Science* 332.6037 (2011): 1537-1541.

[76] Yan, Yang, et al. "A Sandwich-Like Hierarchically Porous Carbon/Graphene Composite

as a High-Performance Anode Material for Sodium-Ion Batteries." *Advanced Energy Materials* 4.8 (2014).

[77] Zhang, Long, et al. "Porous 3D graphene-based bulk materials with exceptional high surface area and excellent conductivity for supercapacitors." *Scientific reports* 3 (2013): 1408.

[78] Raymundo-Pinero, E., et al. "KOH and NaOH activation mechanisms of multiwalled carbon nanotubes with different structural organisation." *Carbon* 43.4 (2005): 786-795.

[79] Viculis, Lisa M., Julia J. Mack, and Richard B. Kaner. "A chemical route to carbon nanoscrolls." *Science* 299.5611 (2003): 1361-1361.

[80] Yushin, Gleb, et al. "Carbide-Derived Carbons: Effect of Pore Size on Hydrogen Uptake and Heat of Adsorption." *Advanced Functional Materials* 16.17 (2006): 2288-2293.

[81] Hanjung, K. W. O. N., and K. A. N. G. Shinhoo. "Carbothermal reduction of Titanium monoxide (TiO)." *Journal of the Ceramic Society of Japan* 116.1358 (2008): 1154-1158.

[82] Kim, Jinhong, et al. "Synthesis of nitrogen and boron co-doped carbon (CNB) and their CO 2 capture properties: from porous to hollow granule structure." *Journal of Materials Chemistry A* 2.39 (2014): 16645-16651.

[83] Seo, M. S., et al. "Tunable and selective formation of micropores and mesopores in carbide-derived carbon." *Carbon* 60 (2013): 299-306.

[84] Zhou, Dongshuai, et al. "Effect of stoichiometry on the surface energies of {100} and {111} and the crystal shape of TiC x and TiN x." *CrystEngComm* 15.4 (2013): 643-649.

[85] Li, Man, et al. "Carbon nanosphere adsorbents for removal of arsenate and selenate from water." *Environmental Science: Nano* 2.3 (2015): 245-250.

[86] Lai, Linfei, et al. "Exploration of the active center structure of nitrogen-doped graphene-based catalysts for oxygen reduction reaction." *Energy & Environmental Science* 5.7 (2012): 7936-7942.

[87] Palaniselvam, Thangavelu, Harshitha Barike Aiyappa, and Sreekumar Kurungot. "An efficient oxygen reduction electrocatalyst from graphene by simultaneously generating pores and nitrogen doped active sites." *Journal of Materials Chemistry* 22.45 (2012): 23799-23805.

[88] Pels, J. R., et al. "Evolution of nitrogen functionalities in carbonaceous materials during pyrolysis." *Carbon* 33.11 (1995): 1641-1653.

[89] Yang, Zhi, et al. "Nitrogen-doped, carbon-rich, highly photoluminescent carbon dots from ammonium citrate." *Nanoscale* 6.3 (2014): 1890-1895.

[90] Luo, Zhiqiang, et al. "Pyridinic N doped graphene: synthesis, electronic structure, and electrocatalytic property." *Journal of Materials Chemistry* 21.22 (2011): 8038-8044.

[91] Sing, Kenneth SW. "Reporting physisorption data for gas/solid systems with special reference to the determination of surface area and porosity (Recommendations 1984)." *Pure*

*and applied chemistry* 57.4 (1985): 603-619.

[92] Yushin, Gleb, et al. "Carbide-Derived Carbons: Effect of Pore Size on Hydrogen Uptake and Heat of Adsorption." *Advanced Functional Materials* 16.17 (2006): 2288-2293.

[93] Yang, L., Shunnian Wu, and J. Paul Chen. "Modification of activated carbon by polyaniline for enhanced adsorption of aqueous arsenate." *Industrial & Engineering Chemistry Research* 46.7 (2007): 2133-2140.

[94] Lua, Aik Chong, and Ting Yang. "Effect of activation temperature on the textural and chemical properties of potassium hydroxide activated carbon prepared from pistachio-nut shell." *Journal of colloid and interface science* 274.2 (2004): 594-601.

[95] Kim, Younghun, et al. "Arsenic removal using mesoporous alumina prepared via a templating method." *Environmental science & technology* 38.3 (2004): 924-931.

[96] Nørskov, Jens Kehlet, et al. "Origin of the overpotential for oxygen reduction at a fuel-cell cathode." *The Journal of Physical Chemistry B* 108.46 (2004): 17886-17892.

[97] Mulliken, Robert S. "Electronic population analysis on LCAO–MO molecular wave functions. I." *The Journal of Chemical Physics* 23.10 (1955): 1833-1840.

[98] Robertson, Alex W., and Jamie H. Warner. "Hexagonal single crystal domains of few-layer graphene on copper foils." *Nano letters* 11.3 (2011): 1182-1189.

[99] Chang, Yee-Shin, et al. "Synthesis, formation and characterization of ZnTiO 3 ceramics." *Ceramics international* 30.8 (2004): 2183-2189.

[100] Norimatsu, W., and M. Kusunoki. "Formation process of graphene on SiC (0001)." *Physica E: Low-dimensional Systems and Nanostructures* 42.4 (2010): 691-694.

# Publication List

### *Peer-reviewed journals:*

5. **JS Han**, DY Chung, DG Ha, JH Kim, K Choi, YE Sung, SH Kang, "Nitrogen and boron co-doped hollow carbon catalyst for the oxygen reduction reaction", ***Carbon***, 105, 1-7, (2016).

4. **Jisun Han**, Soonjae Lee, Keunsu Choi, Jinhong Kim, Daegwon Ha, Chang-Gu Lee, Byungryul An, Sang-Hyup Lee, Hiroshi Mizuseki, Jae-Woo Choi, Shinhoo Kang, "Effect of nitrogen doping on titanium carbonitride-derived adsorbents used for arsenic removal", ***Jounal of hazardous materials***, 302, 375-385, (2016).

3. Jinhong Kim, **Jisun Han**, Daegwon Ha, Shinhoo Kang, *"*Synthesis of nitrogen and boron co-doped carbon (CNB) and their CO 2 capture properties: from porous to hollow granule structure", ***Journal of Materials Chemistry A,*** *2, 39, 16645-16651, (2014)*.

2. Jinhong Kim, **Jisun Han**, Moonsu Seo, Shinhoo Kang, Dongok Kim, Jisoon Ihm, "High-surface area ceramic-derived boron-nitride and its hydrogen uptake properties", ***Journal of Materials Chemistry A***, 1, 4, 1014-1017, (2013).

1. MS Seo, JH Kim, JM Kim, **JS Han**, S Kang, JS Ihm, DO Kim, "Tunable and selective formation of micropores and mesopores in carbide-derived carbon", ***Carbon***, 3, 60, 299-306, (2013).

# Abstract (Korean)

다공성 탄소 재료는 높은 비 표면적, 다공성 및 높은 전기 전도도를 갖기 때문에 가스 흡착, 전극 재료 및 촉매 재료와 같은 학술 및 산업 분야에서 큰 주목을 받고 있다. 염소 가스를 사용하여 탄화물의 금속 상을 선택적으로 제거함으로써 만들어지는 탄화물 유래 탄소 (CDC)는 균일한 미세 기공이 (즉, 2nm 미만의 기공) 특징적이며, 흥미롭게도 기공 크기는 서브 옹스트롬 (sub-angstrom) 범위 내에서 탄화물의 전구체 또는 합성온도를 조절함을 통해 미세 조정된다. 서브 옹스트롬 범위에서 조절 가능한 기공크기는 다양한 응용 분야에 광범위한 관심을 가지며, 특히 전극 재료에 이점을 갖는다. 다양한 방법으로 합성 된 다공성 탄소 중에서도 메조 기공을 갖는 CDC는 전기화학분야에서 집중적으로 연구가 되었는데 그 이유는 이 CDC가 미세 기공뿐만 아니라 메조기공을 갖고 이 계층적인 기공구조는 전기화학분야에서 흡착특성과 흡착 속도를 향상시키기 때문이다. 그러나 현재의 방법은 미세/메조 기공을 갖는 CDC를 생성하기 위해 템플 레이팅 (templating) 및 심각한 세척 등의 복잡한 합성과정을 수반하고 또한 다공성 SiC에만 한정되어 있는 문제가 있다. 논문의 주요 부분은 간단하고 효과적으로 메조기공을 갖는 계층적인 CDC를 합성하는 방법에 초점을 두었으며 이는 titanium carbonitride 그리고 다공성의 titanium carbide의 합성을 통해 이루어졌다. Titanium carbonitride의 염화반응을 통해, 우리는 흑연 층이 계단 가장자리 (step edge) 에서 300도의 낮은 온도에서도 핵 생성되고 입자의 렛지 표면 (ledge surface) 을 따라 성장한다는 새로운 실험 결과를 발견했다. 마지막으로, KOH 활

성화 (KOH activation) 에 기초한 새로운 활성화 방법이 다공성 탄소 표면에 성장된 흑연 층으로부터 그라핀으로 발달시키기 위해 도입되었고 이의 방법을 통해 하이브리드 그라핀/다공성 탄소 (hybrid graphene/porous carbon) 재료가 합성된다.

첫 번째 titanium carbonitride, $Ti(C_xN_{1-x})$는 질소 분위기에서 $TiO_2$와 흑연의 탄화환원반응을 통해 얻어진다. $Ti(C_xN_{1-x})$의 질소 조성은 $TiO_2$ 그리고 흑연의 몰 비율, 합성 온도 및 질소 압력에 의해 조절된다. $Ti(C_xN_{1-x})$의 탄소와 질소의 조성에 따라 그리고 염소반응 온도에 따라 얻어지는 탄소의 기공특성이 조절된다. 염소가 $Ti(C_xN_{1-x})$의 입자 층과 층 (layer by layer) 으로 반응하기 때문에, $TiCl_4$로 기화 된 후 얻어지는 탄소는 C-C 및 C-N 결합의 형태로 남아있게 된다. 그러나 C-N 결합은 고온에서 불안정하기 때문에 $CN_x$와 $N_2$의 형태로 분해가 일어나 $Ti(C_xN_{1-x})$의 질소 함량에 따라 메조 기공부터 매크로 기공까지 추가적인 기공이 생성된다. Titanium carbonitride의 질소 함량이 증가함에 따라 염화반응 후의 잔류 탄소는 C-N 결합의 심각한 분해로 인해 온도가 상승함에 따라 가스화되어 미세 기공 구조의 붕괴를 가져오기 때문에 메조 기공과 매크로 기공만이 발달하게 된다. 따라서 본 논문에서는 $Ti(C_{0.7}N_{0.3})$을 사용하여 균일한 미세 기공 구조를 갖는 다공성 탄소를 합성 하였다. 700 ℃에서 염소화 (CN700으로 표시)는 0.7 nm의 미세 기공과 1~3 nm 범위의 메조 기공을 갖는 다공성 탄소를 합성한다. 염소화 온도가 증가함에 따라, 미세 기공은 메조 기공으로 확장된다. 흥미롭게도, $CN_x$의 분해에 의해, pyrrolic 및 pyridonic 질소 치환기와 같은 가장자리 (edge) 활성 질소가 탄소 격자 내로 균일하게 치환되었다. 이 물질은 물속의 비소 제거를 위한 흡착

제로 적용되었고 비소 제거에 대한 자세한 흡착 메커니즘이 논의된다.

둘째, 다공성 titanium carbide는 아르곤 대기 하에서 흑연으로 $ZnTiO_3$를 탄화 환원 시킴으로써 합성된다. Zn 관련 결합은 먼저 탄소에 의해 파괴되고 점차적으로 Zn으로 환원되기 때문에 불안정한 Ti 성분은 쉽게 환원되어 titanium carbide으로 환원된다. $ZnTiO_3$를 선택한 이유는 Zn는 탄소와 반응하여 탄화물을 만들지 않고 907도에서 쉽게 환원되어 기화, 제거되기 때문에 다공성의 탄화물을 만들 수 있기 때문이다. 금속 Zn은 고온에서 빠른 속도로 기화되어 TiC 입자에 2~80nm의 홀 (hole)을 형성하기 때문에 이 공정은 다공성 titanium carbide를 생성 할 수 있다. 메조기공을 갖는 다공성 titanium carbide의 염소화는 홀 (hole)이 미세 기공과 연결되어 기공 채널 역할을 하기 때문에 계층 적 기공 구조를 갖는 다공성 탄소를 유도한다. 이 방법은 다양한 다공성 탄화물 (TiC, MoC, ZrC, SiC 등)에 적용 할 수 있기 때문에 미세기공의 기공 크기를 조절할 뿐만 아니라 계층적인 기공구조를 가질 수 있는 장점이 있다. 이의 물질은 전기적인 에너지를 가하여 담수화하는 capacitive deionization에 적용되었고 높은 속도 특성을 보였다.

마지막으로 흑연 층에서 그라핀을 개발하는 새로운 방법을 소개된다. 흑연 층은 $Ti(C_{0.7}N_{0.3})$의 염소화에 의해 합성 된 탄소 표면에서 성장되었다. 흑연 층은 금속 포타슘 (K)에 의해 삽입 되어 graphite-intercalation compounds를 형성될 수 있고 기계적 자극에 의해 몇 층으로 박리 될 수 있음을 발견 하였다. KOH 활성화 (KOH activation) 를 통해 형성되는 금속 K는 CN700의 흑연 층으로 삽입되고 몇 층으로 박리되고 상대적으로 결정성이 낮은 내부의 비정질 탄소는 산화반응

을 통해 기공구조가 활성화 된다. 또한, 이 박리된 흑연 층은 용융 솔트 (molten salt) 와의 동시적인 활성화 반응을 통해 1~3 layer로 구성된 2 차원 그라핀으로 발달 되었다. 활성화 과정 및 2 차원 그라핀으로의 발달로 인해, 하이브리드 그라핀/다공성 탄소 (hybrid graphene/porous carbon) 재료는 2200 S/m의 상당히 높은 전기 전도성을 갖고 2.70 $cm^3/g$의 기공 부피, 3779 $m^2/g$의 높은 비 표면적을 갖는 계층 적 기공 구조를 나타냈다. 합성 메커니즘과 그 특성에 대해 자세히 설명되며 이의 물질은 전기적인 에너지를 이용한 담수화 반응에 적용되었고 높은 담수 특성을 보였다.

주요어: 다공성 탄소, 탄화물 유도 탄소, 미세기공, 기공크기분포, 계층적인 기공 구조, 질소 도핑, 다공성 탄화물, 그라핀, 전기 전도성, 비소제거, 축전식 탈염, 화학 활성법.

학번: 2011-20676